SMALL ANGLE SCATTERING OF GAMMA RAYS

AN EXPERIMENTAL INVESTIGATION OF SMALL ANGLE SCATTERING OF (200-1500 keV) GAMMA RAYS

by

NAGANATHASASTRIGAL RAMANATHAN, B.Sc., M.Sc.

A Thesis

Submitted to the Faculty of Graduate Studies

in Partial Fulfilment of the Requirements

for the Degree

Doctor of Philosphy

McMaster University

May 1977

DOCTOR OF PHILOSOPHY
(Physics)

McMASTER UNIVERSITY
HAMILTON, ONTARIO.

TITLE: An experimental investigation of small angle scattering of (200-1500 keV) gamma rays

AUTHOR: Naganathasastrigal Ramanathan
B.Sc. (University of Madras)
M.Sc. (Annamalai University)

SUPERVISOR: Professor W.V. Prestwich

NUMBER OF PAGES: xv : 172

ABSTRACT

Differential cross-sections for the small angle (2^{o} - 10^{o}) scattering of 1408.0, 1274.2, 1112.0, 1085.8, 964.0, 778.9, 443.9, 344.3 and 244.7 keV gamma rays from lead, tantalum, cadmium, copper, aluminum and carbon were measured experimentally employing a high resolution gamma ray spectrometer system. An attempt was made to separate the coherent and incoherent components of the scattered radiation. An empirical model was developed to generate the shape or energy distribution of the incoherently scattered gamma rays and was applied to extract these components where these were unresolved. Various correction factors for the coherent and incoherent components have been considered.

The experimental results for the coherent scattering in lead, tantalum, cadmium and copper were compared with the form-factor based numerical computations. Significant deviations have been observed and some of the possible causes are indicated. The present results are compared with the previous measurements, wherever available, on the basis of momentum trahsfer.

This work reports the first set of systematic measurements of the incoherent scattering cross-sections for small momentum transfers (1.0Å^{-1} - 10.0Å^{-1}). The experimental incoherent scattering functions are found to be considerably lower than the theoretical values for the scatterers of high atomic number.

ACKNOWLEDGMENTS

It is a privilege to be a student of Professor W.V. Prestwich. I thank him for his guidance and advice with respect to this work and far beyond its boundaries. I thank him also for introducing me to different types of projects and providing me with an experience which I would not have gained in any other way.

It is a great pleasure to thank Professor T.J. Kennett for his valuable suggestions and stimulating discussions. It was a pleasure to work with Dr. W.V. Prestwich and Dr. T.J. Kennett because they were always approachable and available for consultations.

I am grateful to Professor R.B. Taylor, James Cook University, Australia for his help during the very early phases of this work.

I thank all my friends in the Nuclear Research Building who contributed to an atmosphere of tranquility and creativity, on weekdays, evenings and weekends. In particular, I wish to thank Dr. A. Robertson, Dr. A.M. Lopez, Dr. L.M. Lowe, Mr. J.E. McFee and Mr. E. Beaver. I am most appreciative to the staff of the McMaster Nuclear Reactor and to the staff of Health Physics Department, for their suggestions and cooperation.

I wish to express my thanks to Mrs. Dorothy Matthews who carried out the difficult task of typing this manuscript.

TABLE OF CONTENTS

TABLE OF CONTENTS

TABLE OF CONTENTS

LIST OF TABLES

LIST OF TABLES

LIST OF ILLUSTRATIONS

LIST OF ILLUSTRATIONS

LIST OF ILLUSTRATIONS

LIST OF ILLUSTRATIONS

LIST OF ILLUSTRATIONS

CHAPTER 1

INTRODUCTION

1. General features of gamma ray scattering

The electromagnetic radiations or photons emitted by excited atomic nuclei are called gamma rays. The interaction of these photons with matter may be classified into absorption and scattering. In the absorption process the photon vanishes losing all of its energy to the medium, but in scattering the photon is merely deflected from the initial direction with or without any change in energy. When a photon is scattered imparting no energy to excite the interacting system (an atom or nucleus) the phenomenon is known as elastic scattering. If the photon raises the internal energy of the atomic system either by ejecting one of the particles or by exciting them to higher energy states, the energy of the scattered photon is reduced. This process is referred to as inelastic scattering [FA 53, CO 23]. The discussion in this report will be limited to the phenomena of importance for gamma ray energies from 200 keV to 2000 keV.

The elastic scattering of gamma rays results from (i) the interaction with the bound electrons of an atom,

the whole atom receiving the recoil energy (Rayleigh scattering)

(ii) the interaction of nuclear charge like a radiating dipole (nuclear Thomson scattering)

(iii) the electrodynamic interaction in which a photon produces electron-positron pairs, real or virtual, in the nuclear electric field and the pairs annihilate yielding a single photon with no energy modification (Delbruck scattering) and

(iv) the resonant process which is possible only when the incident photon energy falls exactly into one of the energy-levels of the scattering nucleus. (nuclear resonant scattering) [DA 65].

In all these elastic scattering processes the whole atom receives the recoil energy. If E is the incident photon energy and θ is the angle between the directions of initial and scattered photons (scattering angle) as in Fig. 1.1, the recoil energy of a free atom is given by

$$E_R = \frac{2E^2}{Mc^2} \sin^2(\theta/2) \left|1 + \frac{2E}{Mc^2} \sin^2(\theta/2)\right|^{-1} \qquad (1.1)$$

where M is the mass of recoiling atom and c is the velocity of light in vacuum.

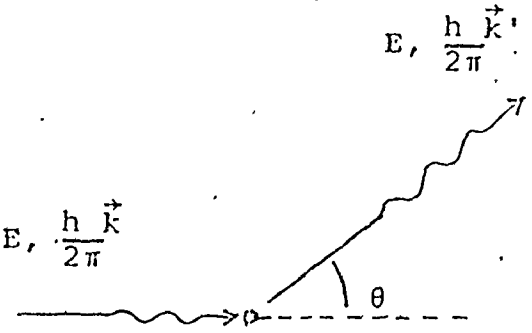

Fig.1.1(a) Elastic scattering of photons

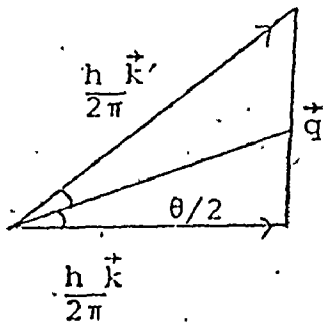

Fig. 1.1(b) Momentum transfer diagram

Legend:

E photon energy

h Planck's constant

$\vec{k}$ propagation vector ($|\vec{k}| = 2\pi.\lambda^{-1}$) before scattering

$\vec{k}'$ propagation vector after scattering

$|\vec{q}| = 2h.x$ where $x = \frac{\sin(\theta/2)}{\lambda}$ and λ is the photon wavelength

$= 0.00391.E.\sin(\theta/2)$ in (mc) units
where m is the electron rest mass and c the velocity of light in vacuum and E is in keV.

For example, when a 1 MeV photon is scattered by a lead atom by 10°, the recoil energy is $\sim$ 0.079 eV. This energy has to be supplied by the incident photon. The situation is different when the atomic scatterer is bound in a solid. Then all the neighbouring atoms may also take up the recoil. Under suitable circumstances the recoil loss can be reduced to zero [DY 73, MO 58].

The wavelengths of incident photons in the present investigation range between 0.051Å (1Å = 1.0×10^{-8} cms) and 0.0088Å. These wavelengths are considerably less than the Bohr radius (= 0.528Å) and are less than the diameter of an atom. Hence any correlation between scattering due to more than one atom must be negligible. Under these conditions the photon scattering amplitude is a coherent sum of the amplitudes associated with each of the elastic scattering processes. The amplitude for the Rayleigh scattering process is the coherent sum of the amplitudes due to the individual atomic electrons. If f_i is the scattering amplitude for i^{th} elastic scattering process, the total elastically scattered photon intensity due to all n processes [MO 50]

$$I_{\text{coherent}}(\theta) \propto \left| \sum_{i=1}^{n} f_i(\theta) \right|^2 \qquad (1.2)$$

In the case of inelastic scattering the phase relationship does not exist, the contributing processes are incoherent, and the incoherently scattered intensity can be written as

$$I_{\text{incoherent}}^{(\theta)} \alpha \sum_i |f_i^{(\theta)}|^2 \qquad (1.3)$$

with f_i representing the scattering amplitude for the i^{th} inelastic scattering process.

The atomic incoherent scattering in the gamma ray energy range is essentially Compton scattering [GR 57] with suitable modifications depending upon the momentum transfer [eq. Fig. 1.1] and atomic number of the scatterer. The energy of the Compton scattered gamma rays is less than the incident photon energy, the difference being a function of the scattering angle. When the energy difference between the coherent and incoherent scattered photons is small or can not be observed experimentally, the understanding of coherent scattering relies on an empirical (or theoretical) estimate of the incoherent part and vice versa.

2. Experimental studies of small momentum transfer scattering of gamma rays.

Of the three common coherent scattering processes, Rayleigh scattering is the only significant contributor in the case of small momentum transfers ($q < 0.5$ mc or $x < 10\text{Å}^{-1}$). For larger momentum transfers, however, nuclear Thomson and Delbruck scattering have amplitudes comparable to the Rayleigh mode and hence must be taken into account [HU 75, PA 75, FA 53, RO 52]. For a given momentum transfer small angle scattering of high energy gamma rays and large angle scattering of low energy gamma rays are equivalent with respect to the differential scattering cross-sections. To the extent that this is true, one is allowed to put together the experimental differential coherent scattering cross-sections in terms of momentum transfer, which is a function of photon energy and scattering angle as well.

Early experimental investigations [MO 50] established the fundamental aspect of Rayleigh scattering as compared to incoherent or Compton scattering - that is, a sharp reduction in differential scattering cross-section with increasing scattering angle. First significant quantitative results, perhaps, were obtained by Storruste [ST 50]. In this

experiment, gamma rays from a ^{198}Au source (411 keV) were scattered by targets made of aluminum, copper and lead and measurements were made at several scattering angles from 3^{o} to 150^{o} using a scintillation counter (scheelite crystal). The Compton scattering cross-section was deduced using the large angle scattering data. Then the Rayleigh scattering cross-section was obtained by subtracting the Compton component from the observed small angle differential scattering cross-section. Though the Compton scattered photons have lower energy than the elastically scattered photons, the energy resolution of the scintillation detector was not good enough to permit the discrimination between the two components, particularly for small momentum transfers. Later experiments involving small momentum transfers also had the same difficulty [MA 65, BE 60, KA 61, NA 64, AN 65, SI 65, HA 66]. In all these experiments monoenergetic sources were employed with a NaI scintillation counting system for the detection of scattered radiation. In general, all these measurements needed some method to estimate the incoherent component.

When the momentum transferred to an electron is very much greater than its momentum while bound to an atom, the

incoherent scattering can be considered to be equivalent to the ideal Compton scattering. But when the two momenta are roughly of the same order of magnitude, the assumptions of the Compton scattering theory is not satisfied. Even for small momentum transfers, low-Z atoms like carbon can be considered as "pure" Compton scatterers while for high-Z atoms this will not be true. As a first step a simple method of estimation of the incoherent component for high-Z atomic scatterers was to assume the Compton scattering to be directly applicable and extrapolate the incoherent cross-section from that of an experimental measurement using a low-Z scatterer like carbon or aluminum [MA 56, KA 61]. For example, under this method, the incoherent scattering cross-section from lead (Z=82) would be $(\frac{82}{6})$ times that from carbon (Z=6), without any regard to the momentum transfer. A more refined method [NA 64] was to use theoretically calculated values of the Compton scattering cross-section after suitable modification. There had been considerable theoretical developments in computing the incoherent scattering function [cf. Ch. 2] which took into account the momentum transfer and atomic electron binding energy. However, the incoherent scattering function itself

had not been put to any serious experimental test.

This thesis presents a series of experiments aimed at resolving the above situation. The high resolution capabilities of a lithium-drifted germanium detector were exploited to accomplish the separation of coherent and the energy-modified incoherent components of the scattered radiation. The gamma ray energies and scattering angles chosen for this investigation cover a region of momentum transfers, from 0.02 to 0.5 mc.

The objective of this investigation is to extend our knowledge of the gamma ray atomic scattering process for small momentum transfers, by a direct experimental measurement of the elastic and the incoherent scattering components.

CHAPTER 2

THEORY

1. Elastic scattering amplitudes

If $A^{\parallel}$ denotes the amplitude for photons which are initially polarized in the plane of scattering and $A^{\perp}$ denotes the amplitude for the photons which are initially polarized perpendicular to the plane of scattering, then the differential elastic scattering cross-section for initially unpolarized photons is given by

$$\frac{d\sigma}{d\Omega}(\theta,\phi) = 1/2\ [|A^{\parallel}|^2 + |A^{\perp}|^2] \qquad (2.1)$$

The amplitudes $A^{\parallel}$ and $A^{\perp}$ themselves are a coherent sum of amplitudes due to different elastic scattering processes. Then,

$$A^{\parallel} = A_R^{\parallel} + A_T^{\parallel} + A_D^{\parallel} + A_N^{\parallel} \quad \text{and}$$
$$A^{\perp} = A_R^{\perp} + A_T^{\perp} + A_D^{\perp} + A_N^{\perp} \qquad (2.2)$$

where the subscript R represents Rayleigh scattering, T denotes nuclear Thomson scattering and D and N stand for Delbruck scattering and nuclear resonant scattering

processes respectively.

The equation (2.1) can be rewritten in terms of scattering amplitudes for circularly polarized photons. Then the scattering amplitude for no change in the state of circular polarization A is written as

$$A = 1/2 \quad [A^{||} + A^{\perp}] \tag{2.3}$$

and the scattering amplitude for change in the state of circular polarization A' is

$$A' = 1/2 \ [A^{||} - A^{\perp}] \tag{2.4}$$

The differential elastic scattering cross-section becomes

$$\frac{d\sigma}{d\Omega}(\theta, \phi) = |A|^2 + |A'|^2 \tag{2.5}$$

The circularly polarized amplitudes can also be decomposed into component processes in a similar fashion. In general, the amplitudes A_R, A_D , A_N , A'_R , A'_D and A'_N are complex; since these add up to yield the total coherent scattering amplitude their relative phases are important.

Their relative phases are determined from the optical theorem and scattering amplitudes at 0^{o} [PA 75]. As far as the present work is concerned, the interference due to Delbruck, Thomson and nuclear resonant processes would be negligible when compared to the Rayleigh scattering amplitude.

2. Nuclear Thomson scattering

Gamma ray photons, being electromagnetic waves, set into forced oscillation the positively charged atomic nuclei. The accelerated nucleus radiates the energy it received. When the gamma ray energy is very much smaller than the rest-mass energy of the nucleus the scattered photon retains all the initial energy except for the small recoil loss. This mechanism was first proposed by J.J. Thomson [CO 35] in the context of low energy X-ray scattering by electrons. The Thomson scattering amplitude is given by

$$A_T = - \left(\frac{Z^2 e^2}{Mc^2}\right) (\hat{\varepsilon}.\hat{\varepsilon}') \qquad (2.6)$$

Ze is the charge as the nucleus

M the mass of the nucleus, and

$\hat{\varepsilon}$ and $\hat{\varepsilon}'$ are polarisation vectors before and after scattering.

In terms of the classical electron radius r_o, A_T can be given as

$$A_T = -\left(\frac{Z^2 m}{M}\right) r_o \quad (\hat{\varepsilon}.\hat{\varepsilon}') \qquad (2.7)$$

where m is the mass of the electron.

It may be observed that the scattering amplitude is independent of energy and depends primarily on $\left(\frac{Z^2}{M}\right)$. The ratio $\left(\frac{Z}{M}\right)$ varies only from 0.39 to 1 across the periodic table and so roughly $A_T \propto Z$. The angular dependence of Thomson scattering is dictated by the polarisation term $(\hat{\varepsilon}.\hat{\varepsilon}')$. The polarization components $A_T^{\parallel}$ and $A_T^{\perp}$ are arrived at, by fixing directions of $\hat{\varepsilon}$ and a direction perpendicular to it, as

$$A_T^{\parallel} = \left(\frac{Z^2 m}{M}\right) r_o \cos\theta$$

and (2.8)

$$A_T^{\perp} = \left(\frac{Z^2 m}{M}\right) r_o$$

For small angles both components $A_T^{\parallel}$ and $A_T^{\perp}$ are about the same while at 90^o, $A_T^{\parallel} \equiv 0$. The differential cross-section for the Thomson process is

$$\frac{d\sigma}{d\Omega} = \left(\frac{Z^2 m}{M}\right)^2 r_o^2 \frac{(1+\cos^2\theta)}{2} \qquad (2.9)$$

For small angles, $\frac{d\sigma}{d\Omega} \approx (Z^2 \frac{m}{M})^2 r_o^2$

Thus, practically this value does not vary. For lead, $A_T^{\perp}$ has a value of about $(0.0178 r_o)$. Comparing this value with the Rayleigh scattering amplitude ($A_R^{\perp} \approx 6.39 r_o$) for 1408 keV for scattering in lead by 10^o, the Thomson amplitude is less than 0.3% of Rayleigh amplitude. This particular case is chosen to illustrate the relative importance of the two cases to the present investigation.

3. Delbruck scattering

The phenomenon of the scattering of photons by a Coulomb field was predicted by M. Delbruck [DE 33] on the basis of quantum electrodynamics. This process can be thought of as pair production in the nuclear Coulomb field followed by annihilation of the pair. Delbruck scattering can be considered as a radiative correction to nuclear Compton scattering [KA 67]. This is a second-order interaction [RO 52] and so the scattering amplitude $\sim (Z\alpha)^2$, where α is the fine structure constant and Z, the number of protons of the scattering nucleus. The amplitude for Delbruck scattering is written as

$$A_D(E,\theta) = A_1(E,\theta) + i\, A_2(E,\theta) \qquad (2.10)$$

where A_1 is known as the dispersive part and A_2 as the absorptive part. Up to 10 MeV, the dispersive part dominates and for higher energies the absorptive part is larger than A_1.

The absorptive part is related to pair production and the dispersive part may be considered to represent scattering of photon by photons [RO 52]. The calculations of scattering amplitudes are complex [PA 75]. The differential Delbruck cross-section is given by

$$\frac{d\sigma(E,\theta)}{d\Omega} = |A_1(E,\theta) + iA_2(E,\theta)|^2 \ (\alpha Z)^4 r_o^2 \qquad (2.11)$$

For $E << mc^2$,

$$A(E,0^o) = A_1(E,0)$$

$$= \frac{73}{72} \left(\frac{1}{32}\right) \left(\frac{E}{mc^2}\right) \qquad (2.12)$$

The Delbruck scattering differential cross-section in lead at 0^o for 1.33 MeV photons is 0.591 millibarns/steradian and thus is negligible for the energies relative to the Rayleigh scattering and angles of interest in this investigation.

4. Rayleigh scattering

The elastic scattering of gamma rays by bound electrons is called Rayleigh scattering [MO 50]. The scattering process consists of the absorption of a primary photon of energy E and the "simultaneous" emission of a secondary or scattered photon of energy E'. When the scattering atom is left in its initial state by the secondary photon, the scattering process is termed elastic. This process takes place through the agency of intermediate states which differ from the initial and final states by one photon emitted or absorbed [He 54] . Then, there can be two kinds of such intermediate states differing in order of the emission of E' and the absorption of E takes place, as shown below:

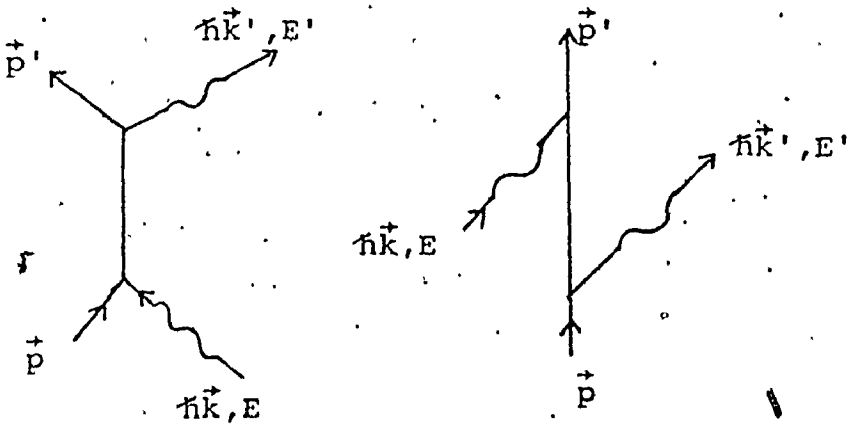

[The vectors $\vec{p}$ and $\hbar\vec{k}$ represent the initial momenta of the electron and photon respectively. The primes denote the momenta of the outgoing particles.]

The relativistic scattering amplitude for Rayleigh scattering is given by [JO 68, BR 55, HE 54]

$$A_R = r_o \sum_n \{ \frac{\langle g|\delta H'|n\rangle\langle n|\delta H|g\rangle}{E_g+E-E_n} + \frac{\langle g|\delta H|n\rangle\langle n|\delta H'|g\rangle}{E_g-E-E_n} \} \qquad (2.13)$$

where $|g\rangle$ and $|n\rangle$ refer to the ground state and intermediate states of a Z-electron atom with E_g and E_n being the corresponding energies of those states. The first term represents the process with absorption of E(the photon energy) at the start and the second term describes the scattering starting with the emission of the photon. The states $|n\rangle$ are obtained by solving the Dirac equation [SC 55] for electron in a central field. We may write this as,

$$(E_n - H)\ |n\rangle = 0 \qquad (2.14)$$

with the Hamiltonian H being

$$H = - c\vec{\alpha}.\vec{p} - \beta mc^2 + V(r). \qquad (2.15)$$

In the equation (2.15) $\vec{\alpha}$ and β are the Dirac matrices and V(r) is a central potential for the elctron. A perturbation ΔH due to an electromagnetic (or radiation) field represented by a vector potential $\vec{A}(\vec{r},t)$ is deduced by replacing $(c\vec{p})$ by $(c\vec{p}-e\vec{A})$ in the Hamiltonian (2.15) as

$$\Delta H = \vec{\alpha} \cdot e\vec{A} \qquad (2.16)$$

The perturbation δH and $\delta H'$ will be

$$\delta H = \hat{\varepsilon} \cdot \sum_{j=1}^{Z} \vec{\alpha}_j \, e^{-\vec{k}\cdot\vec{r}_j} \qquad \text{and}$$

$$\delta H' = \hat{\varepsilon}' \cdot \sum_{j=1}^{Z} \vec{\alpha}_j \, e^{-i\vec{k}'\cdot\vec{r}_j} \qquad (2.17)$$

where the operator $\vec{A}$ is replaced by $\hat{\varepsilon}\, e^{i\vec{k}\cdot\vec{r}_j}$

The photon polarization direction is denoted by the unit vectors $\hat{\varepsilon}$ and $\hat{\varepsilon}'$. The propagation vectors for the photons are given by $\vec{k}$ and $\vec{k}'$ such that:

$$E = \hbar c|\vec{k}| = \hbar c|\vec{k}'| = \hbar ck \qquad (2.18)$$

The radius vector $\vec{r}_j$ represents the position of the j^{th} electron. It may be noted that the vector $c\vec{\alpha}$ corresponds to velocity in the non-relativistic limit [ME 66, HE 54]. The interaction matrix given in (2.13) includes the effects of the non-relativistic operators $\vec{p}.\vec{A}$ and $\vec{A}^2$ [BR 54].

For a scattering angle θ, i.e. the angle between the directions of the propagation vectors $\vec{k}$ and $\vec{k}'$, the momentum transferred by the photon to the atom is

$$\hbar q = 2\hbar k \sin(\theta/2) \qquad (2.18)$$

The momentum transfer is presented in several ways in the literature. The equivalent forms of the momentum transfer are:

$$x = \sin(\theta/2) \cdot \lambda^{-1} \qquad (k = (2\pi)\lambda^{-1}) \qquad (2.19)$$

and $Q = \frac{\hbar q}{mc}$

In the former form x is given in units of Å^{-1} or $10^8 cm^{-1}$ and the later one is in the (mc) units where m is the electron rest-mass.

If $Q << 1$ and the intermediate states are assumed to be free-electron states, the Rayleigh scattering amplitude

reduces to [WE 27, HA 51, LE 52, NE 55, BA 69]

$$A_R = r_o(\hat{\varepsilon}.\hat{\varepsilon}') \sum_{j=1}^{Z} \langle g|e^{i(\vec{k}-\vec{k}').\vec{r}_j}|g\rangle \qquad (2.20)$$

The amplitude under this approximation is called the form-factor. In this form it is possible to calculate the amplitude and there have been quite a few attempts made in this direction.

Introducing

$$F(q) = \sum_{j=1}^{Z} \langle g|e^{i\vec{q}.\vec{r}_j}|g\rangle \qquad (2.21)$$

we can write the Rayleigh scattering amplitude as

$$A_R = r_o\ (\hat{\varepsilon}.\hat{\varepsilon}')F(q)$$

and the differential scattering cross-section for this process with initially unpolarized radiation is

$$\frac{d\sigma}{d\Omega}_R = r_o^2\ \frac{(1+\cos^2\theta)}{2}\ |F(q)|^2 \qquad (2.22)$$

In an equivalent form we can write for F(q),

$$F(q) = \sum_{j=1}^{Z} \int_{o}^{\infty} |\psi(\vec{r}_j)|^2 e^{i\vec{q}\cdot\vec{r}_j} d^3 r_j \qquad (2.23)$$

where $\psi(\vec{r}_j)$ is the ground-state wave function for j^{th} electron. The term $|\psi(\vec{r}_j)|^2$ represents the electronic charge distribution at the position vector $\vec{r}_j$. In the literature F(q) is referred to as the form-factor, atomic scattering factor or electronic structure factor.

Debye and Harms obtained a simple form for F(q,Z) on the basis of a Gaussian charge distribution function [DE 30] given as

$$F(q,Z) = Z\, e^{\frac{-q^2 A_{TF}^2}{4}} \qquad (2.24)$$

where $A_{TF} = \frac{0.47}{Z^{1/3}}$ in $\mathring{A}$ $[1\mathring{A} = 10^{-8}\text{cm}]$.

Applying the Fermi-Thomas model [FE 28, TH 26] of an atomic charge distribution, Franz [FR 35, FR 36] derived a form factor,

$$F(x,Z) = Z \int_{o}^{\infty} R^{-1/2}\, \phi^{3/2}(R)\, \frac{\sin uR}{u}\, dR \qquad (2.25)$$

where $R = \frac{r}{\mu}$ with $\mu = 0.47Z^{-1/3}A^{o}$, and

$$u = 5.906Z^{-1/3}x \text{ with } x = \frac{\sin\theta/2}{\lambda} (A^{o})^{-1} .$$

$\Phi(R)$ is the Fermi function [FE 28]. Using an approximate series expansion for Φ [BA 30] it was shown [FR 36] that for $x>x_F = 1.065Z^{1/3}$, the form-factor reduces to a simple form as

$$F(x,Z) \approx 0.08745 \left(\frac{Z}{x}\right)^{3/2} [1-0.2017\left(\frac{Z}{x}^{1/3}\right)] \qquad (2.26)$$

The value of x_F is a characteristic of the atomic number, presented in Table 2.1 . For $x>>x_F$, the differential Rayleigh scattering cross-section becomes

$$\frac{d\sigma}{d\Omega} \approx 3.036x10^{-4} \left(\frac{Z}{x}\right)^{3} \frac{(1+\cos^2\theta)}{2} \text{ barns/Sr.} \qquad (2.27)$$

Expressing this in terms of gamma ray energy E we have [MO 50]

$$\frac{d\sigma}{d\Omega} = 0.5783 \frac{Z^3}{(E\sin\theta/2)^3} \frac{(1+\cos^2\theta)}{2} \text{ barns/Sr}$$

where E is given in keV.

TABLE 2.1

Characteristic Momentum Transfers

Element	Atomic Number Z	Momentim transfer x_F in (Å^{-1})
Lead	82	4.627
Tantalum	73	4.451
Cadmium	48	3.870
Copper	29	3.272
Aluminum	13	2.504
Carbon	6	1.935

With these results, some observations on the Rayleigh scattering process can be made.

On the basis of the form-factor approximation, for q or x = 0, we must have $F(0,Z) \cong Z$ and the scattering cross-section becomes

$$\frac{d\sigma}{d\Omega} = r_o^2 Z^2$$

In the range of x=0 to $x=x_F$, the differential Rayleigh scattering cross-section varies as the exponent of Z changes from 2 to 3. In the same range the exponent of the momentum transfer variable x, changes from 0 to (-3). Another significant deduction is that the cross-section depends primarily on momentum transfer x rather than on the gamma ray energy. It is also interesting to note that more than three quarters of the scattered radiation takes place for momentum transfers x less than x_F. The momentum transfers x_F for the elements under investigation are given in Table 2.1. This characteristic momentum transfer can be expressed in terms of a characteristic scattering angle θ_F as

$$\theta_F = 2.13 \lambda Z^{1/3} \qquad (2.28)$$

where λ is the wavelength of the incident photon, in A^{o} units. For gamma ray energies, the Rayleigh scattering process takes place mainly in forward angles. The value of θ_F is inversely proportional to gamma energy (or proportional to wavelength). Thus the simple derivation was useful in bringing out the main features of Rayleigh scattering.

Pauling and Sherman [PA 27, PA32] developed an analytical method of computing form-factors under the following assumption. Each electron of an atom is assumed to move in a hydrogen-like nuclear Coulomb potential with a correction included for the effect of screening of this potential due to the inner shell electrons. Since the wave-functions thus obtained are hydrogen-like, form-factors can be analytically calculated. This procedure was adopted, in this thesis, to estimate the contribution of the electrons from different shells of the atom, to the scattering amplitude. This method, though simple, provides an insight into the physics of the situation. Partial form-factors f_K, f_L and f_M for K- , L- , and M-shell electrons in lead, tantalum, cadmium and copper were computed.

The relative contributions of f_K, f_L, f_M etc., to the total form-factor F ($=f_K+f_L+f_M+ \ldots$) change with the

momentum transfer x. As x increases the form-factors corresponding to the inner shells tend to dominate the scattering and in the region of momentum transfer x between 0.4 and 10.0 $\mathring{A}^{-1}$ covered in this work the K, L and M shells play a prominent role. To bring out these features while comparing the experimental results, the form-factors were computed on the basis of Pauling and Sherman model and are presented with a discussion in Chapter 5.

More rigorous computations were done using the Hartree-Fock self-consistent field method of generating many electron wave-functions [HA 28]. Nelms and Oppenheim [NE 55] performed numerical computations of form-factors and tabulated them in a graphical form. Recent develbpments in computational techniques and in digital computer facilities have made possible a more complete tabulation of form-factors for a wide range of x, for all atoms. The method of calculation, for x up to 10 $\mathring{A}^{-1}$, was based on non-relativistic Hartree-Fock wave-functions due to Cromer and Mann [CR 68]. The form-factors were tabulated in the Journal of Physical and Chemical Reference Data volume 4, No. 3, 1975 [HU 75]. This extensive tabulation has helped the comparison with the experimental data.

Brown, Peirls and Woodward [BR 55] devised a method of calculation of scattering amplitude matrix elements for gamma ray scattering in mercury due to K-shell electrons. They used relativistic wave-functions for electrons and took into account the intermediate states properly. The differential elastic scattering cross-sections were calculated for gamma ray energies 163.5, 327, 654 and 1308-keV. The series of interesting publications [BR 55, SH 55, BR 56, BR 57] threw light on the differing features between the form-factor approximation and their method based on second order perturbation theory.

First, even at 0°, their scattering amplitude, which includes the binding of electrons in intermediate states, was less than the form-factor (for K-shell electrons) by as much as 30%. The form-factor approximation does not include the imaginary part which can be related to the photoelectric effect. For low energies, this part is significant. For example, for 163.5 keV gamma rays in mercury the imaginary part was calculated to be about 14% of the real part of the scattering amplitude for all scattering angles. For higher energies this part reduces in value. For all energies above 163.5 keV, their scattering amplitude was less than form-

factor by about 25 to 30%. The binding in the intermediate states was shown to have a significant effect for x not too small compared to 20 $\mathring{A}^{-1}$. However, for L-shell and outer shell electrons this effect is expected to be less important. They proposed a correction to the form-factor to take into account the effect of intermediate states. The scattering amplitude for n^{th} shell electrons in these cases, could be approximated to [BR 57]

$$A_{R_n} = r_o(\hat{\epsilon}.\hat{\epsilon}') \sum_{j=1}^{Z_n} \int_o^\infty |\psi(\vec{r}_j)|^2 \frac{e^{i\vec{q}.\vec{r}_j} d^3r_j}{[E_T+V(r_j)]} \qquad (2.26)$$

where E_T is the total energy of the bound electron

-V is the Coulomb potential and the sum over j is done for Z_n electrons in the n^{th} shell.

5. Incoherent scattering of gamma rays

When a gamma ray photon is scattered by a free electron at rest, the energy and momentum conservation laws, lead to a reduction in energy of the scattered gamma rays [CO 22, CO 23, DE 23]. This phenomenon is the well-known Compton effect . The energy of the scattered photon E' can

be expressed, in terms of the (photon) scattering angle θ (cf. Fig. 1.1) and the initial energy of the photon E, as

$$E' = \frac{E}{1+\frac{E}{mc^2}(1-\cos\theta)} \tag{2.27}$$

where mc^2 is the electron rest mass energy. On the basis of the relativistic quantum-mechanical considerations [KL 29] the differential cross-section for the unpolarized incident gamma rays is given by the following Klein-Nishina formula:

$$\frac{d\sigma}{d\Omega} = \frac{r_o^2}{2}\left(\frac{E'}{E}\right)^2\left[\left(\frac{E}{E'}\right) + \left(\frac{E'}{E}\right) - \sin^2\theta\right] \quad \text{per electron} \tag{2.28}$$

where r_o is the classical electron radius.

The scattered photons, from different electrons bear no relationship in phase and hence the Compton cross-section due to scattering from all the Z electrons of an atom is

$$\frac{d\sigma(\theta,\phi)}{d\Omega}_{\text{Atom}} = Z \cdot \left(\frac{d\sigma}{d\Omega}\right)_{\text{electron}} \tag{2.29}$$

This is true only when the momentum transferred to the electron greatly exceeds the initial momentum of the electron's motion within the atom. In the non-relativistic approximation, this condition leads to

$$q \doteq 2.\left(\frac{E}{c}\right) \sin\theta/_2 >> (B.2m)^{1/2}. \qquad (2.30)$$

where B is the electron binding energy.

For K-electrons in lead, B=88 keV. When E =1408 keV, the ratio of the momentum transfer to the initial electron momentum is approximately unity for $\theta \approx 12.2^{o}$. Thus for the gamma ray energies and scattering angles involved in this investigation, for high-Z materials, the ideal Compton effect conditions are not satisfied. In order to account for this binding energy effect, the incoherent scattering differential cross-section is separated into two factors as

$$\frac{d\sigma(\theta,\phi)}{d\Omega}_{\text{incoherent}} = S(q,Z) \left(\frac{d\sigma}{d\Omega}\right)_{\text{electron}} \qquad (2.31)$$

The factor S(q,Z) is called the incoherent scattering function [GR 57].

Defining $F_\varepsilon(\vec{q},Z)$ as

$$F_\varepsilon(\vec{q},Z) = \langle\psi_\varepsilon| \sum_{j=1}^{Z} e^{i\vec{q}.\vec{r}_j} |\psi_o\rangle \qquad (2.32)$$

$$S(q,Z) = \sum_{\varepsilon>o} |F_\varepsilon(\vec{q}.Z)|^2$$

where ψ_ε is the wave function for an excited state or ionized state of the electron; the summation sign represents the sum over discrete states and the integral over the continuum states.

On the basis of the Thomas-Fermi approximation, the incoherent scattering function was calculated by Bewilogua [BE 31, HE 31]. $S(q,Z)$ was rewritten as

$$S(q,Z) \equiv S(x,Z) \equiv S(v)$$

where $v = 2.2166\ x.Z$

Several model calculations are outlined in the excellent review by [GR 57].

An empirical equation for $S(v)$ was obtained by fitting to these calculations [VE 66]. They arrived at a function for S as

$$S(v) = 1 - e^{-(4.88\ v^{0.856})} \qquad (2.33)$$

The incoherent scattering function for an atom with Z electrons can be thought of, as a sum of a similar factor for the individual electrons. Then

$$S(q,Z) = Z - \sum_{i=1}^{Z} |f_0^i(q)|^2 \qquad (2.34)$$

where f_0^i represents the amplitude for the i^{th} electron not to get excited nor ionized, on receiving the momentum q. The amplitude $f_0(q)$ is different from the form-factor amplitude $f^i(q)$ by the fact that some of the transitions are forbidden by the Pauli exclusion principle. Since the form-factor data are more extensively available, one may write

$$S(q,Z) = Z - \sum_{i=1}^{Z} |f^i(q)|^2 - \left[\sum_{i=1}^{Z} |f_0^i(a)|^2 - \sum_{i=1}^{Z} |f^i(q)|^2\right] \qquad (2.35)$$

Now the term in the brackets can be evaluated as a correction [WA 29, PI 46]. The most complete tabulation for incoherent scattering functions for all elements for the range of x in this report, is available [HU 75]. In these calculations, Hartree-Fock self-consistent-field wave functions were used and S(x,Z) was calculated using the complete Waller-Hartree theory [WA 29] with exchange terms.

6. Photoelectric effect

In this absorption process, a gamma ray , with energy E greater than atomic electron binding energy B, is completely absorbed by the atom and the electron escapes from the atom with a kinetic energy [EI 05]

$$T = E - B \tag{2.36}$$

For $B << E << mc^2 \approx 511$ keV, on the basis of non-relativistic calculations [HE 54] atomic K-shell contribution to the photoelectric differential cross-section by an atom of atomic number Z,

$$\frac{d\sigma_K}{d\Omega} \propto Z^5 \left(\frac{mc^2}{E}\right)^{7/2} \tag{2.37}$$

For $E >> mc^2$,

$$\frac{d\sigma_K}{d\Omega} \propto Z^5 \left(\frac{mc^2}{E}\right) \tag{2.38}$$

From these expressions one may infer that the photoelectric cross-section falls off rapidly for high energies. If σ_K, σ_L and σ_M are the photoelectric total cross-sections for K, L and M shells respectively, then we have [RO 68]

$$\sigma_K \approx \frac{4}{5} \sigma_o$$

$$\frac{\sigma_K}{\sigma_L} \approx 5 \text{ and } \frac{\sigma_L}{\sigma_M} \approx 4$$

These ratios lead to the conclusion that inner shells of the atom contribute much more than the outer shells - a property similar to the Rayleigh scattering. In fact, the Rayleigh scattering at 0^o and photoelectric cross-section can be related by optical theorem [BR 54].

7. Pair production

A photon with energy greater than $2\ mc^2$ ($\approx$ 1.022 MeV) may be absorbed in the neighbourhood of an atomic nucleus or an atomic electron and produce an electron-positron pair. For low energies, i.e., $(\frac{E}{mc^2} - 2) << 1$, the pair production cross-section [RO 68]

$$d\sigma \alpha Z^2 \left(1 - \frac{2mc^2}{E}\right)^3 \qquad (2.39)$$

It is interesting to note that for photon energies below 2 MeV, this process is not important relative to the Compton scattering. For gamma ray energies greater than 5 MeV, the

pair production is a major process of absorption.

8. Gamma-ray attenuation in matter

All the processes described in the previous sections contribute to the removal of gamma-rays from the original photon beam. The total interaction cross-section for the gamma rays with a material is obtained by summing the integral cross-sections for each of those processes [DA 52, NE 53, RO 68, EV 55]. The photoelectric effect, Compton effect and the pair production are the important modes in this regard. For the energy range of this study the Compton and photoelectric processes dominate the gamma-ray attenuation. For 1000 keV photons in lead, the coherent processes form only 3% of the total interaction cross-section while the incoherent scattering can account for 71% of the total. However as the energy is lowered the coherent scattering tends to become important relative to the incoherent part. For example, for a 200 keV gamma-ray in lead the coherent and incoherent processes are responsible for 5.4% and 9.2% of the total attenuation [ST 70] respectively.

CHAPTER 3

EXPERIMENTAL DESIGN

1. Introduction

Experimental investigation of photon scattering requires a photon-source of constant intensity, a suitable collimation system and a reliable detection system. A convenient scattering geometry is a very important part of the design and the choice largely depends upon the measurements of interest. In the present case, the experiment was designed to measure

(i) the angular distribution of scattered gamma rays

(ii) the energy dependence of the scattering process and

(iii) the variation of scattering intensity with atomic number of the scatterer.

Small angle scattering is the matter of current study and the angular interval was chosen to be from 2^{o} to 10^{o}.

2. Choice of photon source

First, the photon energy range of interest had to be decided upon. Above 2 MeV, the atomic nucleus starts to play a significant role in the scattering process (RO 52). Below 100 keV, anomalous dispersion effects are important, depending upon shell ionisation energies

of the scatterer (GR 57). The intermediate energy region is ideally suited to study the scattering due to atomic electrons.

The use of monoenergetic sources necessitates a program of serial measurements in which several different sources must be prepared and introduced into the apparatus. With the advent of high resolution spectroscopic techniques this procedure can be circumvented. Thus polyenergetic sources yielding the energy dependence during each measurement may be used. Many radioactive sources of this type are available. It is desirable that the isotope be considerably long lived. If the half life is much longer than the entire period of measurements, the correction for the decrease in source intensity due to radioactive decay is small.

The isotopes, europium-152 and europium-154, satisfy all the criteria, their gamma spectrum containing ten prominent lines, from 122-keV to 1408-keV. These isotopes were produced by irradiation of europium oxide (Eu_2O_3, 99.99%) in the McMaster Nuclear Reactor. Natural europium has two prominent isotopes ^{151}Eu (47.8%) and ^{153}Eu (52.2%). On irradiation, the following nuclear reactions occur:

$$^{151}_{63}Eu + \text{Thermal neutron} \rightarrow {}^{152}Eu \quad (\sigma_a = 5000 \text{ barns})$$

$$^{152}_{63}Eu \xrightarrow{\beta^-} {}^{152}_{64}Gd \text{ (stable)} \quad \text{(Half-life 13.2 years)}$$

$$^{152}_{63}Eu \xrightarrow{\beta^+} {}^{152}_{62}Sm \text{ (stable)} \quad \text{(Half-life 13.2 years)}$$

$$^{153}_{63}Eu + \text{Thermal neutron} \rightarrow {}^{154}Eu \quad (\sigma_a = 480 \text{ barns})$$

$$^{154}_{63}Eu \xrightarrow{\beta^-} {}^{154}_{64}Gd \text{ (stable)} \quad \text{(Half-life 8.5 years)}$$

Some details of the container used for the irradiation are in order at this point. The schematic is shown in Fig. 3.1. A fine quartz tube of 3 mm inner diameter and 1 mm wall-thickness was packed with Eu_2O_3 powder. The packed region was about 3 cms long and contained 295 mg of Eu_2O_3. The open end of the quartz tube was sealed. The reactor irradiation procedures required this sealed tube to be placed inside a standard size reactor-grade aluminum capsule and this was also sealed. Specifically for this

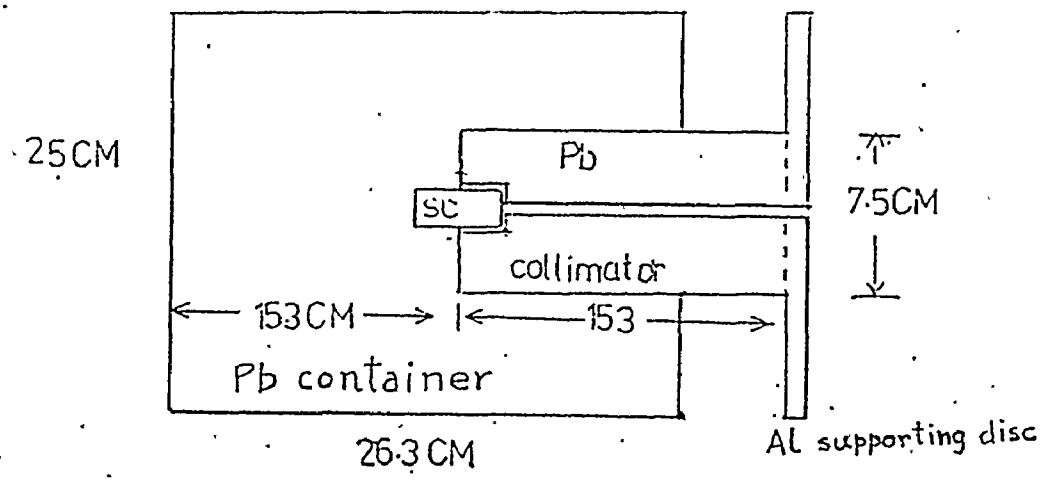

SC - source capsule

Fig. 3.2 Schematic diagram of the source-container

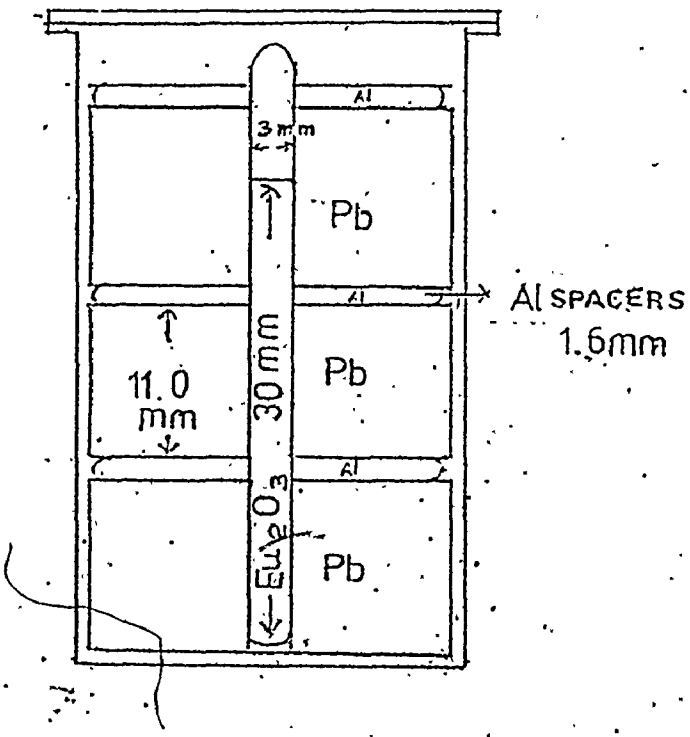

Fig. 3.1 Schematic diagram of the irradiation capsule

investigation, the position of the quartz container was fixed by aluminum spacers and lead donuts. While the lead donuts provided the shielding, the aluminum spacers held the quartz container in position along the longitudinal axis of the cylindrical aluminum capsule. This design protected the container geometry against any possible softening of lead and consequent shape deformation due to local heating during neutron irradiation. To add mechanical strength, the quartz container was wrapped lengthwise with aluminum sheet.

This doubly sealed capsule was irradiated in the McMaster Nuclear Reactor to produce the required source, of about five Curies strength. After the period of irradiation (5 weeks) and a period of 2 weeks to allow for the decay of short-lived radioactive isotopes, the aluminum capsule was carefully dropped in position into a specially designed source-container made of lead (Fig. 3.2).

3. Experimental System Geometry

The choice of scattering system geometry was guided by the following criteria:

(i) the source-to-target and target-to-detector distances should not be changed throughout the measurements

(ii) for all scattering angles, the target should face the same part of the collimated photon beam (This is not true for a ring geometry (NA 64).)

(iii) any possible effect due to a non-uniform density within a collimated beam should be circumvented.

The resulting system geometry is presented in Fig. 3.3. In this geometry, the collimation system determined the photon beam size; the targets used had larger area than beam size; and different scattering angles were realized by rotating the source and collimation system around a pivot under the target position. The details of the experimental arrangement are given in Fig. 3.4.

The lead-castle source-container, and four lead collimators were all mounted on the grooves of an aluminum H-beam. On the source-end the H-beam rested on a movable cart and the other end was supported by a pivot which could be raised or lowered. The Ge(Li) detector used in this experiment was placed in an immovable cart at a desired distance from the pivot position. All the lead collimators had 0.635 cm holes along their axes. The lead-castle and the collimators had circular

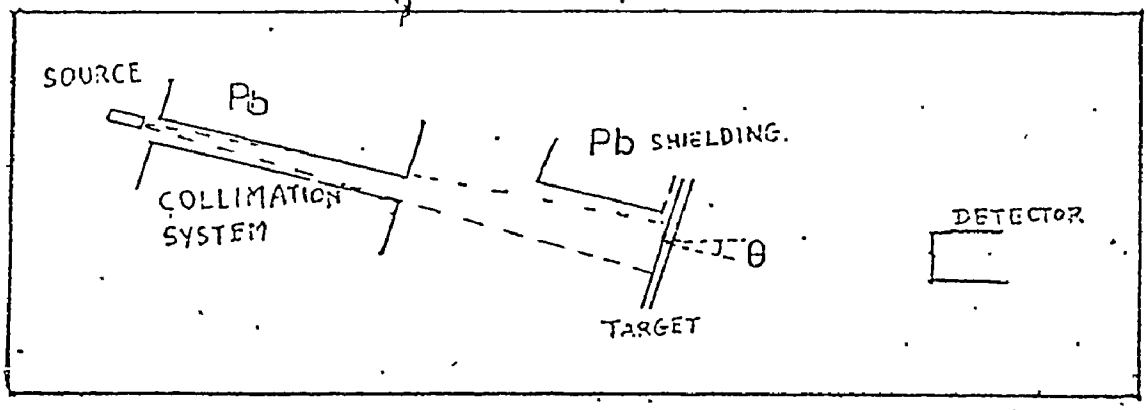

Fig. 3.3 Schematic diagram of the scattering geometry of the set-up

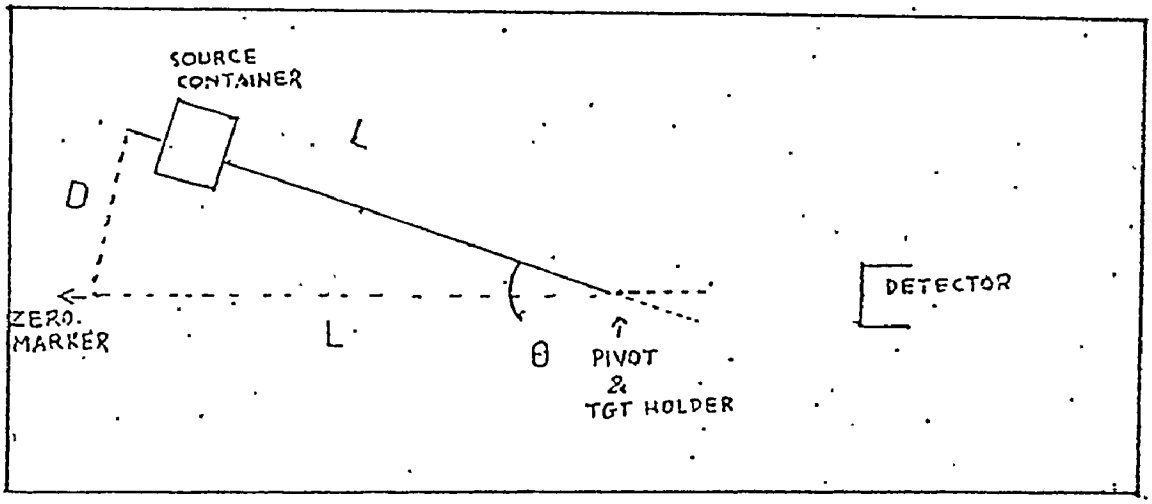

Fig. 3.3(a) Schematic diagram for measurement of scattering angle of the set-up

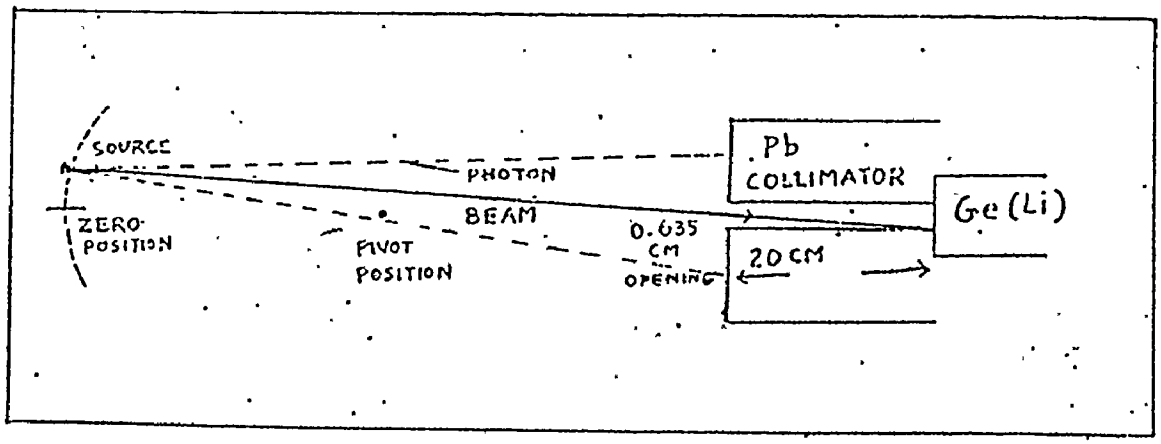

Fig. 3.3(b) Schematic diagram for measurement of beam profile

end surfaces, 25.4 cm in diameter, and hence all their axial holes lined up when these were mounted on the H-beam. By varying the positions of these collimators along the H-beam, the photon beam size could be varied. Before the lead container was in position, a laser beam was passed through the collimators placed at different positions along the H-beam. The height of the Ge(Li) detector was adjusted using this laser spot.

A target holder was placed above the pivot position perpendicular to the photon beam and it was attached to the H-beam. As the H-beam was rotated the target would also turn accordingly. The target position was ascertained by tracing the photon beam using a Geiger counter and x-ray sensitive films. The source-to-target, target-to-counter distances and all the other dimensions are given in Fig. 3.4.

Some lead shielding close to the target was necessary (cf. Fig. 3.3) to prevent any photons reaching the detector from the edges of the last collimator, C1 in Fig. 3.4. The minimum scattering angle, in this type of geometry, is limited by the width (or diameter) of the diverging photon beam at the detector position. Thus, in

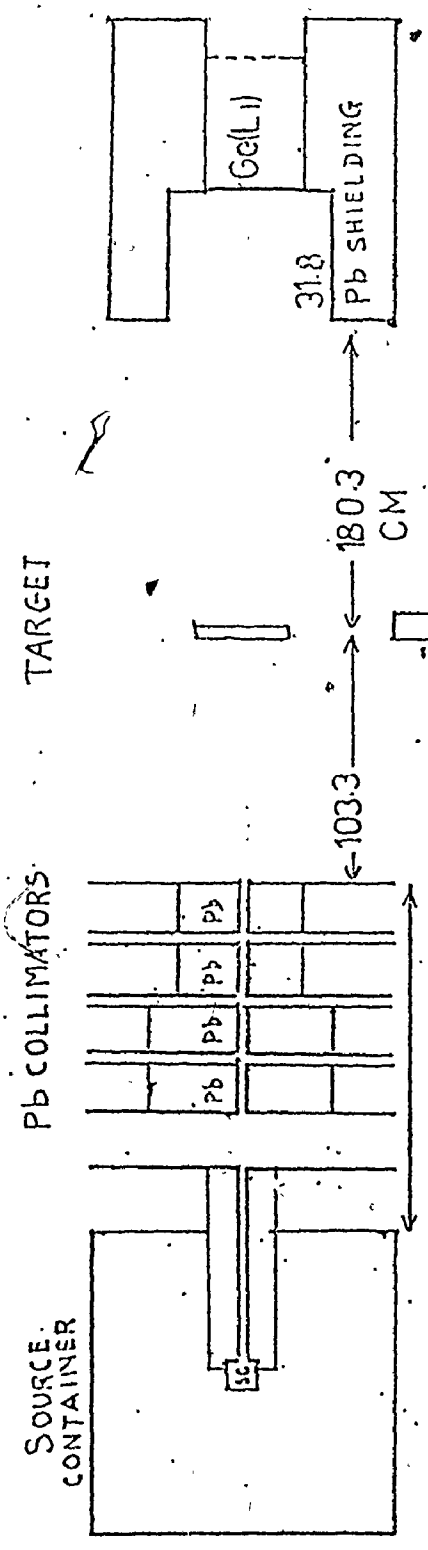

Fig. 3.4 Schematic diagram of the experimental system

the position of the smallest angle for measurement the direct photon beam will just miss the detector.

The size of the photon beam, the collimator positions and the source-to-target and target-to-detector distances were all adjusted for count rates of about one per minute at the scattering angles of interest.

Scattering angles were measured using a plumb line hanging from the end of the rotating arm. Before mounting the source on the arm, using a large beam and lead collimators, a geometric 'zero' position of the plumb line was marked on the floor. As the arm was rotated, the chord length between the current plumb line position and 'zero' position was measured, (Fig. 3.3). Then the scattering angle θ is given by

$$\theta = 2 \sin^{-1} \left(\frac{D}{2L} \right)$$

Values measured in this way agreed within $\pm 0.3^{\circ}$ with those obtained by Compton peak analysis. The uncertainty stemmed from the statistical nature of the peak-data obtained by fitting (cf. Chapter 4) procedure. The zero position was also confirmed by an experiment to measure the diverging source photon beam profile directly. An 8" long lead collimator with a 0.25" hole was placed at

the centre in front of the detector directly looking at the centre of the target. This positioning was adjusted using a weak Eu source at the target position. The source-arm, with lead collimators under the regular experimental positions, was positioned at several angles (1 cm of chord length ≈ 0.15^{o}) and spectra were collected in each position. Counts per minute of each peak were computed in every case, thus making up a beam profile. The collimator in front of the detector helped cut down the rate so that a meaningful spectrum could be obtained. The 'zero' position measured in this fashion agreed within 0.05^{o} with the geometric position marker.

4. Target Samples

To measure the variation of scattering intensity with atomic number Z, the target elements chosen were carbon (Z=6), aluminum (Z=13), copper (Z=29), cadmium (Z=48), tantalum (Z=73) and lead (Z=82). The lateral dimensions of all targets were 5 cm by 5 cm square. Usually targets were cut out of a sheet and the pieces were stacked together to form different thicknesses.

The photon source consisted of gamma rays of different energies and for each energy attenuation in the target is different. For thin targets, the number of

scattered gamma rays due to single scattering,

$$n_s(\theta) \alpha\ \sigma(\theta) t\ \mathrm{Exp}(-\mu(E)t) \qquad (1.4)$$

where $\sigma(\theta)$ is the scattering cross-section for scattering by a small angle θ (with sec $\theta \approx 1$), t is the target thickness and $\mu(E)t$ is the total attenuation cross-section.

From the relation (1.4) one may find that n_s is a maximum for $\mu(E)t = 1$. Correcting for the absorption in the scatterer, we may write for the corrected count-rate

$$n_s'(\theta) = n_s(\theta) e^{\mu(E)t} \quad \alpha\ \sigma(\theta) t \qquad (1.5)$$

Immediately it is observed that n_s' is proportional to thickness for a single scattering process. When the scattering within the target involves more than one interaction or multiple scattering, the relationship between n_s' and t becomes non-linear. In the present experiments, using different target thicknesses, the linear region for each energy was measured. Typical measurements of this type are presented in Figures 3.5a and 3.5b. For the collection of data, only those thicknesses which would be linear with the corrected count-rates were employed.

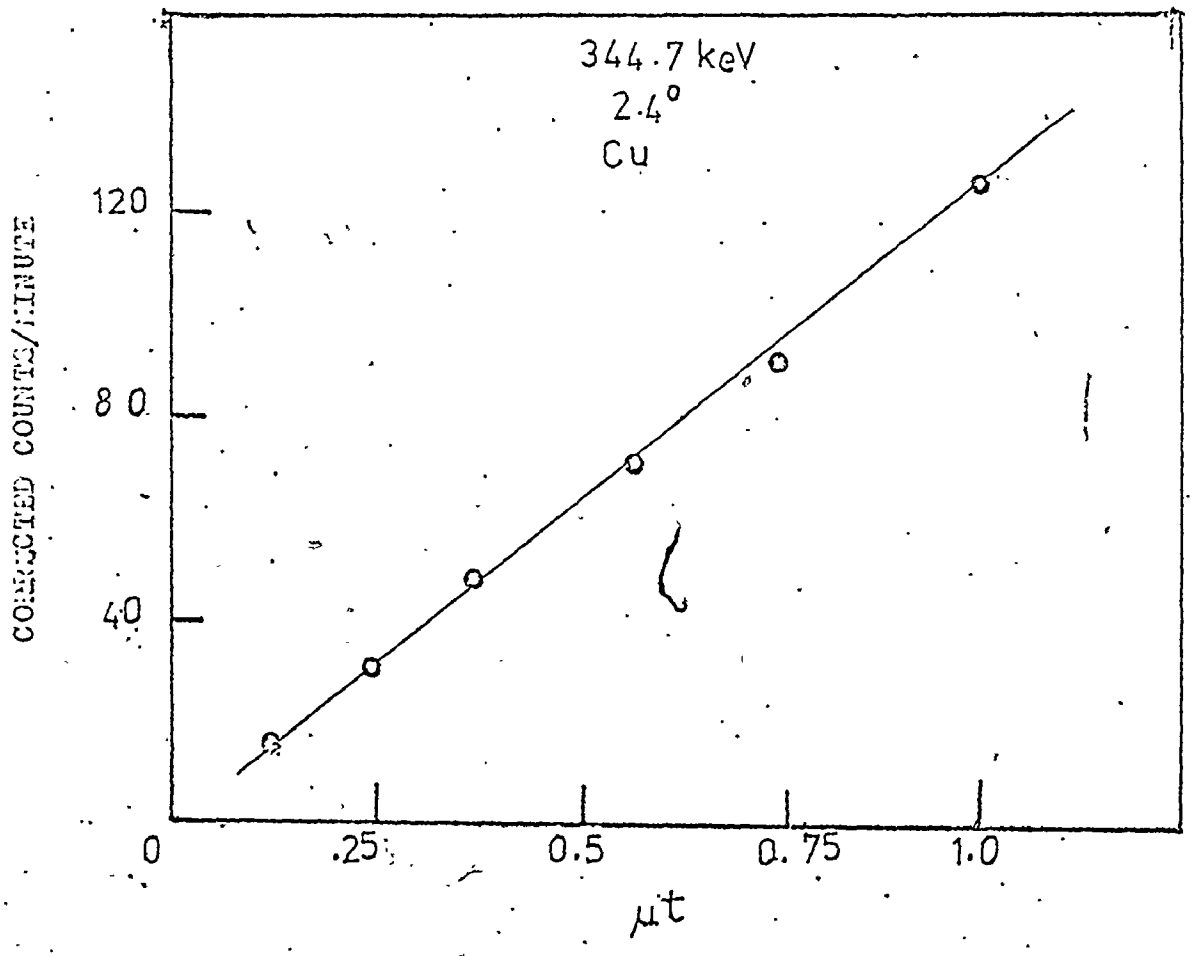

Fig. 3.5(a) Dependence of countrates on scatterer thickness for 344.7-keV gamma ray in copper at 2.4°

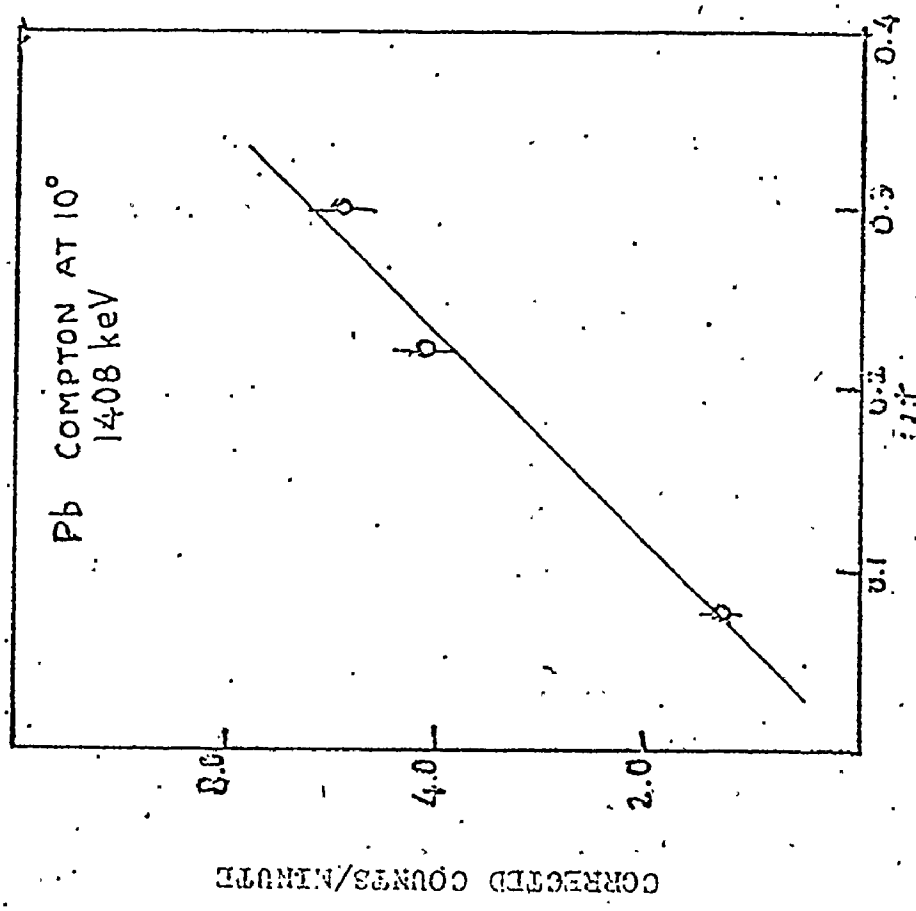

Fig. 3.5(b) Dependence of Compton component on scatterer thickness for 1408-keV gamma ray in lead at 10°

All the targets used in this experiment were 99.9% pure metallic sheets. Their thicknesses were measured using a micrometer and by weighing as well. The range of target thicknesses used for the measurements are as follows:

For lead 0.011 cm to 0.531 cm
tantalum 0.00508 cm to 0.203 cm
cadmium 0.044 cm to 1.76 cm
copper 0.043 cm to 1.89 cm
aluminum 0.317 cm to 2.54 cm and for
carbon 0.52 cm to 2.44 cm (density = 1.545 gm/cc).

5. Detection System

A lithium drifted germanium detector was the primary component of the detection system. Basically, a Ge(Li) detector is a p-i-n diode reverse biased and kept at 77°K. The gamma rays interact with germanium via the photoelectric effect, Compton effect or pair-production when energetically possible. Below 1.5 MeV, the photoelectron acquires the full gamma ray energy (less electron shell binding energy and recoil energy) while the Compton electron receives only a fraction of that energy. These energetic electrons ionize the

intrinsic region producing electron-hole pairs at the expense of 2.98 eV per pair. These charges are collected, integrated and suitably amplified. The width of the full energy peak in the spectrum, so obtained, is a figure of merit for the detector. The full width at half-maximum height (FWHM) for the Harshaw Model Ge(Li) detector used in these experiments was 2.3 keV at 1.33 MeV incident gamma energy. Another interesting property of a detector is the ratio of full energy peak height to the Compton continuum height on the low energy side of the peak. This ratio was 25 : 1 for this detector. The detector is a coaxial type, operated at -2900 V and has the following geometric specifications:

Total diameter of Ge	4.0 cm
Total length	3.8 cm
Drift depth	1.5 cm
"p" core diameter	1.1 cm

The excellent FWHM of this detector permit the resolution of elastic and inelastic components in the observed spectrum - the prime aspect of this investigation.

6. Data Handling System

The detector signal, after suitable amplification, was coupled to an analog-to-digital converter (ADC). After pulse-height analysis by the ADC, the events were accumulated in a Nuclear Data - 3300 multi-channel analyzer memory. The memory of this analyzer consists of 16K words or channels with 18 bits per channel. The spectra were collected and stored in 2048-channel groups. The data were transferred on to a magnetic tape and were analysed using a CDC-6400 digital computer. A block diagram of the data handling system is presented in Fig. 3.6.

A spectrum stabiliser was used to maintain the gain and zero of the spectrum constant. This operation requires two reference peaks in the spectrum. A weak americium-241 radioactive source (59.9 keV) was used for the low energy reference. A stabilisation pulser (Canberra Model 1504, 60c/s)was used to simulate a high energy peak.

It was realised that the data collection live-time (run-time) could be deduced from this pulser peak. Usually each run took a day. The analyzer memory can store only 2^{18} events per channel and the pulser peak overflowed

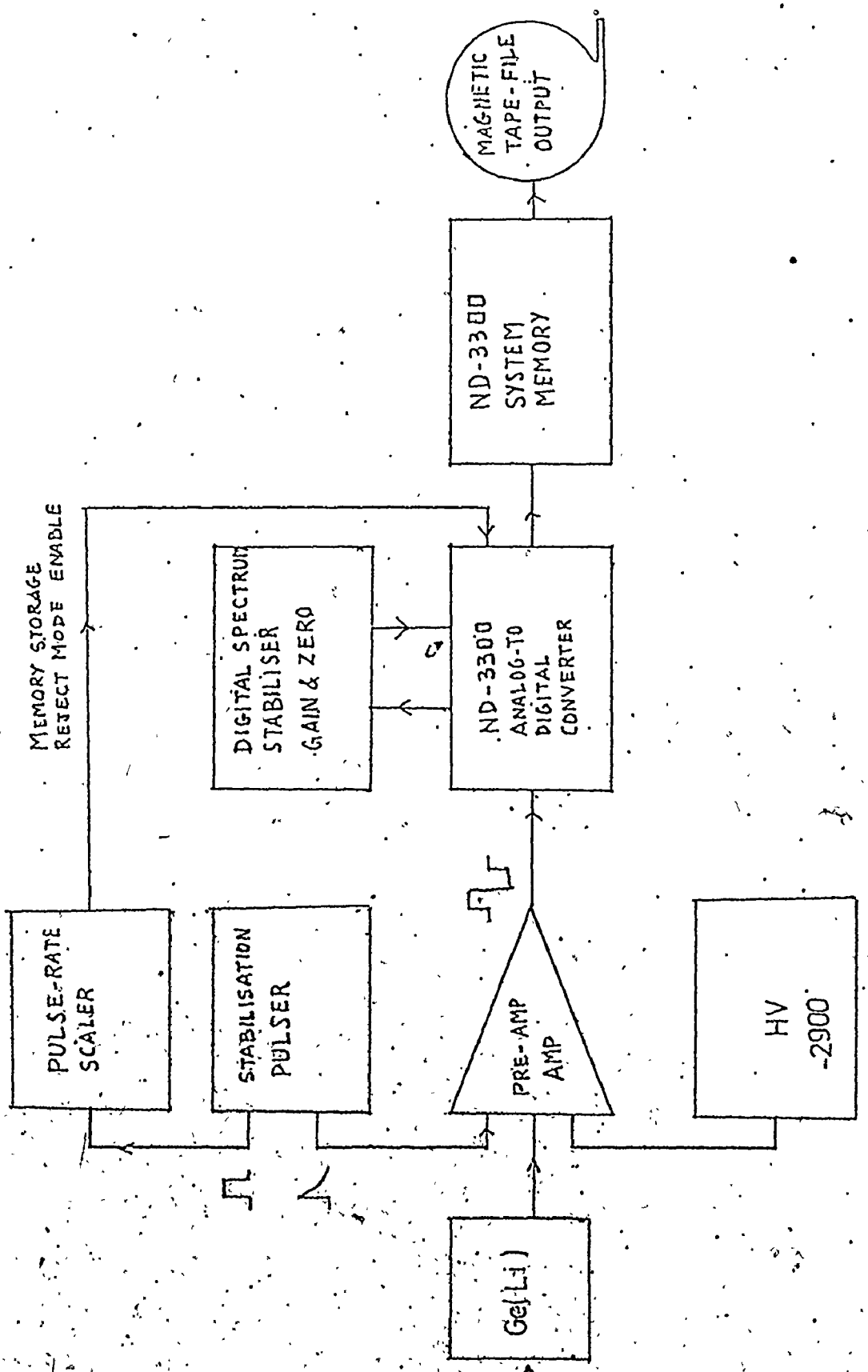

Fig. 3.6 Block diagram of the data acquisition system

about seven times a day. It was possible to inhibit the memory store process for the pulser events at a desired rate. This was accomplished by a pulser-rate scaler circuit (Fig. 3.7) and by the operation of the analyzer in a memory storage reject mode for pulser events.

7. Pulse -rate Scaler

The stabilisation pulser, used for the high energy reference provides a linear and a logical output, synchronised with each other. This logical pulse triggers a monostable MS1 and the width of the output is fixed by adjustable R-C components (cf. Fig. 3.7).

At this stage, the circuit operation can be understood in terms of two branches. One branch, consisting of a monostable MS-3, produces the same number of input pulses, of desired width. On the other branch, the number of input pulses are scaled by two decades. The width of output pulses from monostable MS-2 have to be wider than those from MS-3. By adjusting the R-C components of these monostables, the outputs of both these branches are set to arrive in time to an AND gate which serves the purpose

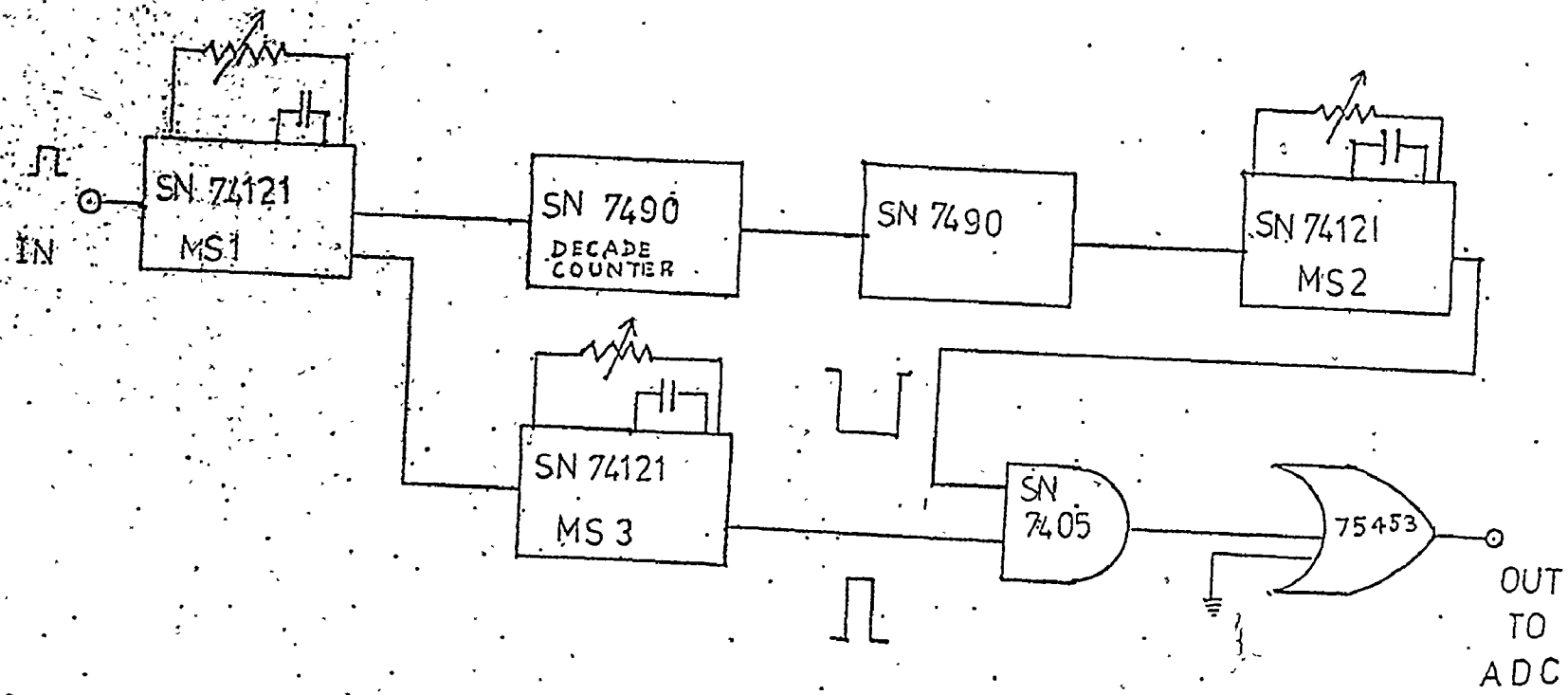

Fig. 3.7 Diagram of the pulse-rate scaler circuit

of suppressing the output, for one out of one hundred pulses. Using a driver, the output of the pulser rate scaler provides a trigger for analyzer storage suppression.

In this mode of application, any input to the ADC, in time with the above trigger pulse, is pulse-height analysed and used for stabiliser correction; but it is not accumulated in the analyzer memory.

CHAPTER 4

DATA ANALYSIS PROCEDURES

1. Relation between the observed count-rate and scattering cross-section.

The number of scattered gamma rays of energy E' observed at a mean angle θ_m to the initial direction (cf. Fig. 4.1) from a differential target element of thickness dt is given by

$$dI_S = \frac{N_o \rho}{A} \cdot dt \cdot \iint I_o(E,\theta_1) \cdot e^{-\mu_T(E)t \sec\theta_1} \cdot e^{-\mu_T(E')(\ell-t) \sec\theta_2} \varepsilon(E',\theta_2) \cdot \frac{d\sigma}{d\Omega}(\theta,E) \cdot d\Omega_t(\theta_1) \cdot d\Omega_d(\theta_2) \qquad (4.1)$$

where $I_o(E,\theta_1)$ is the number of incident photons of energy E along the initial direction θ_1

$d\Omega_t(\theta_1)$ is the differential solid angle of the target for the incident photons

$[\frac{N_o \rho}{A}]$ the number of target atoms per unit volume, ρ being the density, A the atomic mass and N_o the Avogadro's number

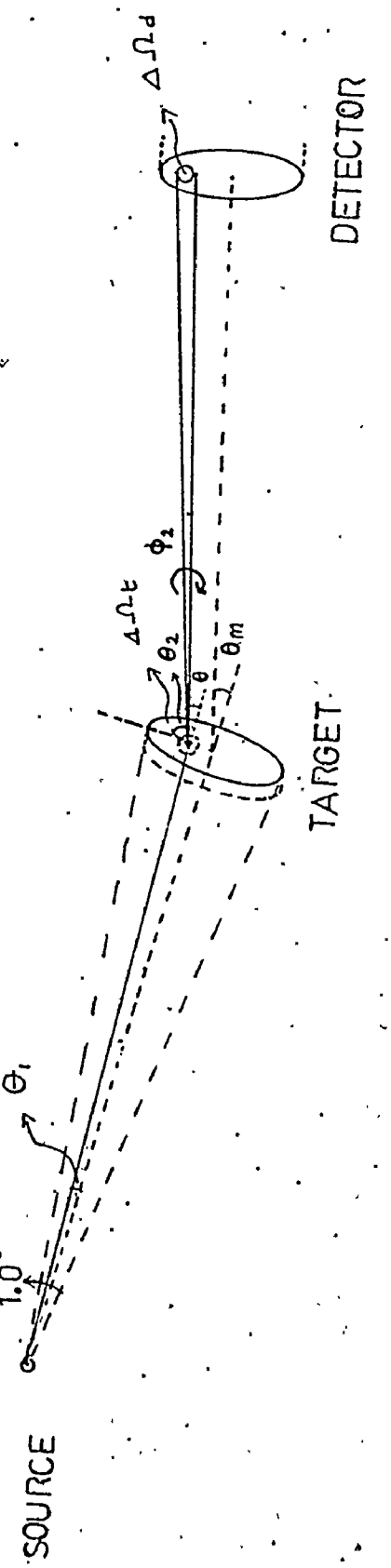

Fig. 4.1 Schematic diagram of a differential scattering system

$\varepsilon(E;\theta_2)$ the efficiency of the detector for the scattered ray

$d\Omega_d(\theta_2)$ the detector differential solid angle

$\mu_T(E)$ the total absorption coefficient for the photons of energy E in the target

ℓ the total thickness of the target and

$\frac{d\sigma}{d\Omega}(\theta,E)$ the differential scattering cross-section for photons of energy E at a scattering angle θ $(\theta_1,\theta_2,\phi_2)$

In the above formula θ_1 is defined for a coordinate system on the source, and θ_2 for a coordinate system placed on the target. The values of θ_1 are less than 0.5° and the values of $(\theta_2-\theta)$ are also in the same range. In all cases of interest, the value of $\sec\theta_1$ is nearly equal to unity and that of $\sec\theta_2$ can be assumed to be equal to $\sec\theta$. We did not attempt to calculate the solid angle factors directly but tried to evaluate the effect through an empirical procedure outlined in a later section.

Considering the photon transmission part in the above expression for a target of thickness ℓ, we have

$$\int_0^{\ell} dt\, e^{-\mu_1 t}\, e^{-\mu_2(\ell-t)\sec\theta} = \left[\frac{1-e^{-(\mu_1-\mu_2\sec\theta)\ell}}{\mu_1-\mu_2\sec\theta}\right] \cdot e^{-\mu_2\ell\sec\theta}$$

where $\mu_1 \equiv \mu_T(E)$ and $\mu_2 \equiv \mu_T(E')$. (4.2)

When the term $(\mu_1-\mu_2.\sec\theta)\ell << 1$, this integral reduces to $[\ell e^{-\mu_T(E')\ell.\sec\theta}]$. In the current set of experiments the condition $(\mu_1-\mu_2\sec\theta)\ell < 0.1$ was maintained and hence the above approximation was valid. It may be observed that the transmission appears to be equal to the case of the scattered photon passing through the whole thickness. Now the number of scattered gamma rays for a scatterer (or target) of thickness ℓ can be written as

$$I_S(E',\theta)=I_o(E)\Delta\Omega_t \cdot [\frac{N_o\rho}{A}] \cdot \frac{d\sigma_S(\theta,E)}{d\Omega}\ell.e^{-\mu_T(E')\ell.\sec\theta}$$

$$.\Delta\Omega_d.\ \varepsilon(E).(1+\delta_{E'}) \qquad (4.3)$$

where $\varepsilon(E')\equiv\varepsilon(E)(1+\delta_{E'})$.

In equation (4.3) we have assumed, say a point scatterer and point detector such that we can represent the solid angles by $\Delta\Omega_t$ and $\Delta\Omega_d$ without any dependence on θ_1,θ_2 or θ.

The efficiency $\varepsilon(E')$ is written in terms of the efficiency of the detector for incident photons of energy E and a correction factor $\delta_{E'}$. The term $(1+\delta_{E'})$ represents

the relative change in efficiency for detection due to a change in energy of the photon.

To obtain the differential scattering cross-section we can rewrite (4.3) as

$$\frac{d\sigma_S(\theta,E)}{d\Omega} = I_S(E',\theta)\,\frac{e}{\ell}^{\mu_T(E')\ell.\sec\theta}\,K^{-1}.(1+\delta_{E'})^{-1}.N^{-1} \qquad (4.4)$$

where $K \equiv I_o(E)\Delta\Omega_t\,.\Delta\Omega_d\,.\varepsilon(E)$ and the atomic density $N \equiv \frac{N_o\rho}{A}$. We may refer to K as the observable source photon strength factor.

For coherent scattering, imposing the conditions $E' = E$ and $\delta_{E'} = 0$, the differential scattering cross-section becomes,

$$\frac{d\sigma_{CoH}(\theta,E)}{d\Omega} = I_S(E,\theta).\frac{e}{\ell}^{\mu_T(E)\ell.\sec\theta}\,K^{-1}N^{-1} \qquad (4.5)$$

In the case of incoherent (Compton) scattering, however, the relationship given by equation (4.4) is directly applicable.

2. Energy calibration

The energies and the relative strengths of the gamma rays emanating from the radioactive sources ^{152}Eu and ^{154}Eu are well known [BO 74, RI 70]. The energy spectrum of a weak europium source (^{152}Eu and ^{154}Eu) as observed by our Ge(Li) detection system is presented in Fig. 4.2. An ^{241}Am radioactive source emitting 59.9 keV gamma rays and the 1460-keV gamma rays from K^{40} present in the room back-ground were included in the spectra providing an independent built-in energy calibration. At times independent standard gamma ray sources were also used for the same purpose.

3. Computation of full-energy peak area

It is a common practice that the area of the full-energy peak or photo-peak in the energy spectrum is taken to be representative of the number of events in the detector and this area, when corrected for detector efficiency, yields the intensity of the gamma ray, with the energy given by the peak position. This full-energy peak lies on top of the room background events and the Compton events in the detector. If the room background is smooth in the energy region of interest, the contribution

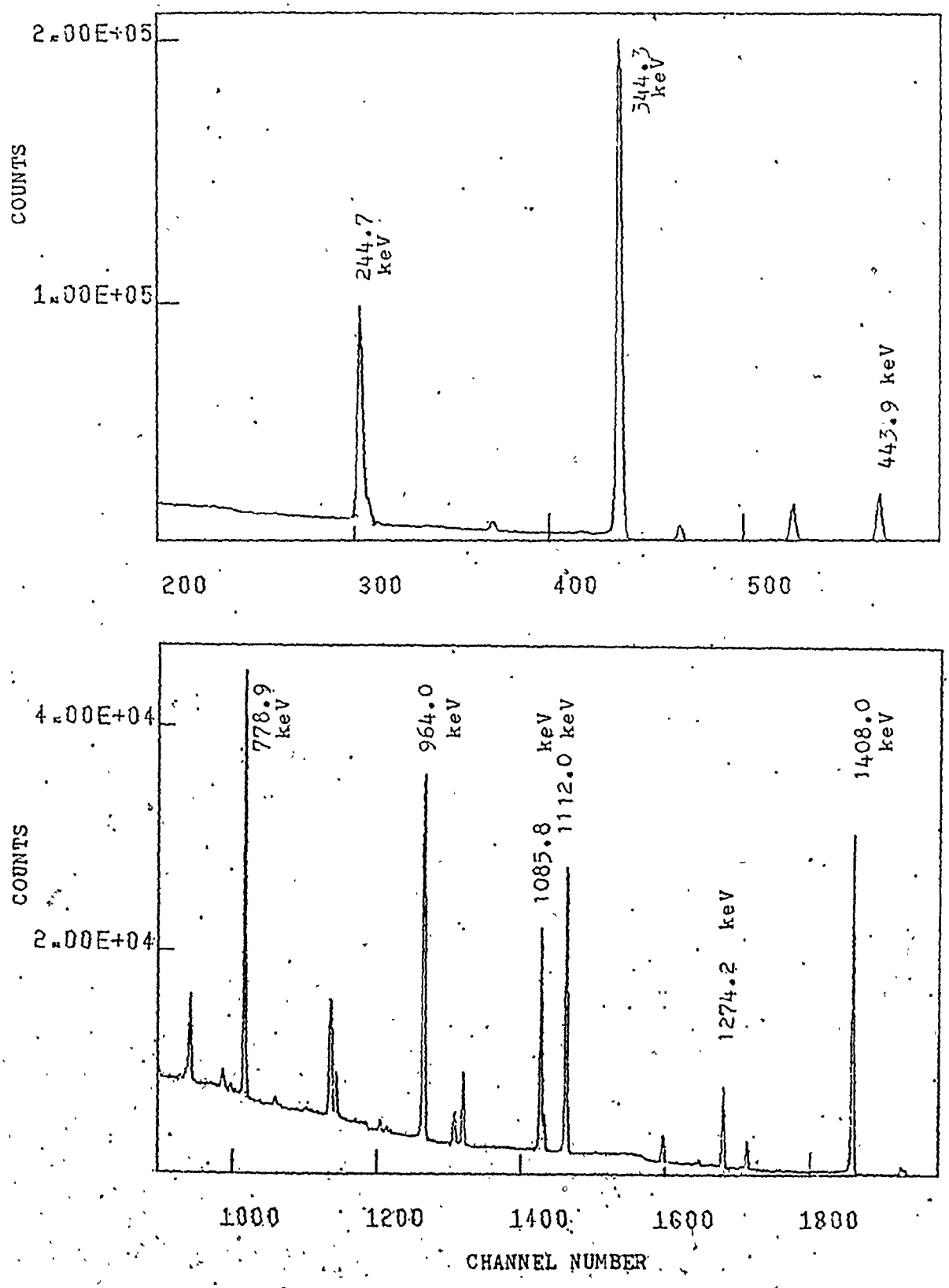

Fig. 4.2 Energy spectrum of the europium source

of room background and the Compton events in the detector is estimated using a small portion of the energy-spectrum on either side of the full-energy peak. These two wing regions are fitted to a parabola or straight line. Using the parameters of this fit, the curve is extrapolated under the full-energy peak region. Thus the continuum area under the peak is computed. Then the full energy peak area or the gamma line-intensity is given by the total area under the full energy peak minus the continuum area. A straight-line model for the background continuum was found to be giving reproducible results in all cases.

4. Attenuation correction

The number of counts in the full-energy peak was first corrected by the factor $[\frac{e^{+\mu_T \ell \sec\theta}}{\ell}]$. The effect of scattering angle in this factor can be understood by considering the ratio

$$\tau(\theta) = [\frac{e^{+\mu_T \ell \sec\theta}}{\ell}] \cdot [\frac{e^{+\mu_T \ell}}{\ell}]^{-1} = e^{+\mu_T \ell (\sec\theta - 1)} \qquad (4.6)$$

For $\theta = 10^0$ and $\mu_T \ell = 1$, $\tau = 1.016$ and thus the effect of angle over this correction factor is small. This

correction was performed for each target sample using gamma ray attenuation coefficients for every energy of interest. The coefficients were obtained from the currently available data of Storm and Israel [ST 70] by the method of least-squares fit. The tabulated data were fitted to an inverse polynomial function represented by

$$\mu_T(E) = \sum_{n=0}^{m} a_n E^{-n} \qquad (4.7)$$

where m was in the range of 7 to 9. Using the set of fitted coefficients a_n for the polynomial, μ_T's for all the energies were calculated. The corrected peak-areas for all samples of different thicknesses were averaged.

5. Empirical model for the angular resolution functions

In an ideal experiment, with a single ray, a point scatterer and a point-detector, the scattering angle is unique with no spread. However in a practical experiment there will be a finite spread due to the following causes:

(a) the diverging incident rays introducing different scattering angles

(b) the size of the incident beam

(c) the size of the detector and the spatial distribution of efficiency of the detector for different scattered rays.

To get some insight into the problem a very simple situation may be considered.

For a point scatterer (cf. Fig. 4.3) at O, let the mean scattering angle be θ_m. For any scattering angle θ, the scattered intensity along an infinitesimal area dA on the detector of uniform efficiency is given by

$$dI(\theta) = K(E, I_o, \Delta t) \frac{d\varphi_s(\theta)}{d\Omega} \int d\Omega_d \qquad (4.8)$$

where $\int d\Omega_d = \sin\theta \Delta\theta \int_{\phi_1(\theta_m,\theta)}^{\phi_2(\theta_m,\theta)} d\phi$

Here ϕ represents the azimuthal angle and K is a function of incident energy, photon distribution and the target thickness.

Let us define an angular resolution function $w(\theta_m, \theta)$ such that

$$w(\theta_m, \theta) \equiv \sin\theta \int d\phi \qquad (4.9)$$

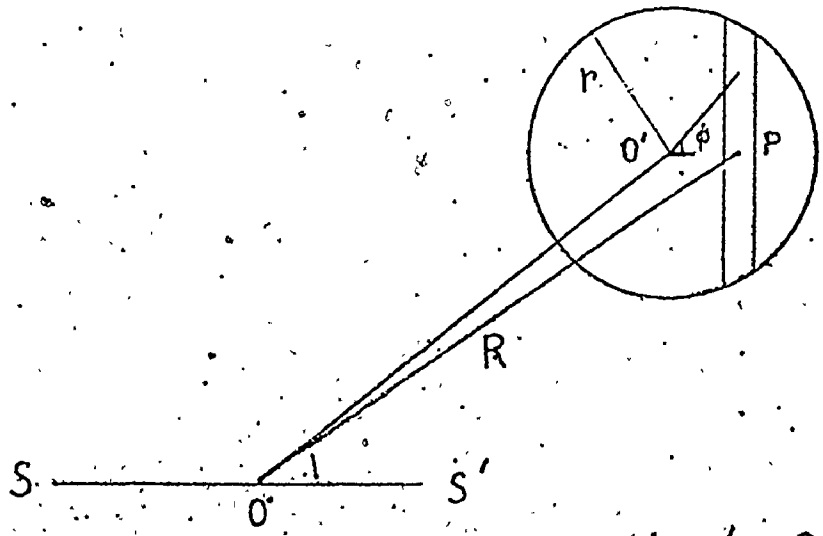

$O'OS' = \theta_m$

$POS' = \theta$

$O'OP = \theta_m - \theta$

$= \theta_1$

Fig. 4.3 Schematic diagram of a scattering system with a point-scatterer and a finite detector.

For the set up in Fig. 4.3, the area of the strip dA covering the point P essentially defines the solid angle of that part of the detector. Then we have the solid angle for this area

$$d\Omega = 2\left[\frac{r^2}{R^2} - \tan^2\theta_1\right]^{1/2}\sec^2\theta_1 d\theta \qquad (4.10)$$

where $\theta_1 = \theta_m - \theta$. Then the angular resolution function normalised to unity at $\theta_m = \theta$ or $\theta_1 = 0$ is given by

$$w(\theta_m, \theta) = \frac{1}{a}\left[a^2 - \tan^2\theta_1\right]^{1/2}\sec^2\theta_1 \qquad (4.11)$$

where $a = \frac{r}{R}$ with a value of 0.0185 in our experiment. This distribution is presented in Figure 4.3a.

In the above case, just the effect of the face-area of the detector over the scattering angles was found. The inclusion of all the other effects makes the calculation very difficult. However these could be taken into account in an empirical form. The experimental scattering angles may be characterized in a fashion similar to the above case, by a mean scattering angle and a distribution function for the angular spread.

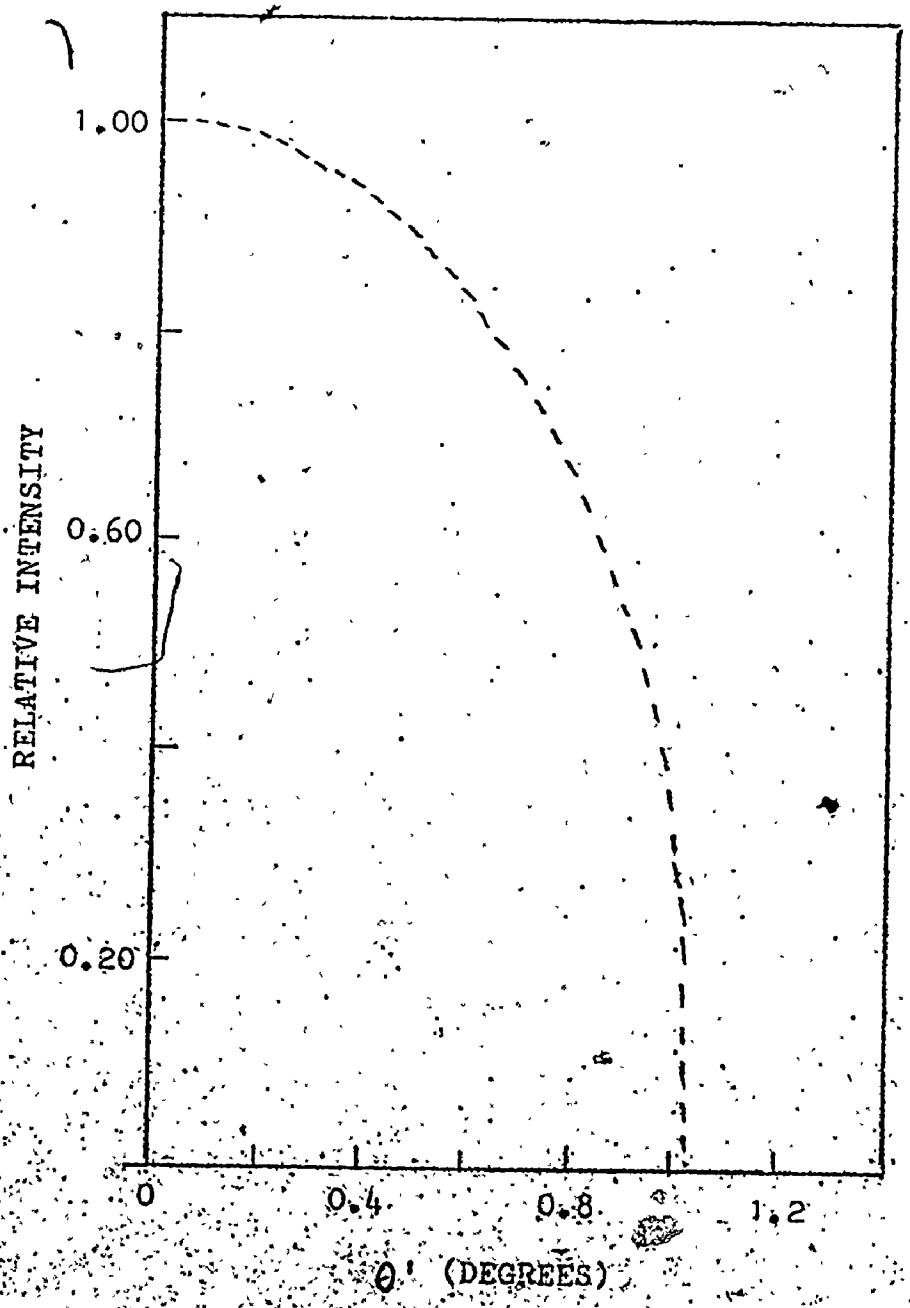

Fig. 4.3(a) Angular resolution function for the point-scattering system

To deduce these factors the experimental data for the Compton scattered gamma ray spectrum were used. The energy of the scattered photons in this case is related to the scattering angle and the incident energy. So, for a pure Compton scatterer, the energy distribution carries the information about the distribution of scattering angles for an experimental system. From the energy-angle relationship for the Compton scattered photons, we have

$$\frac{dE'}{d\theta} = \frac{-\sin\theta}{mc^2} E'^2 \qquad (4.12)$$

If the detector resolution is small compared to the width of the Compton scattered photon experimental energy distribution then we are justified in transforming the energy distribution into an angular distribution without any need for removing the effect of detector resolution by deconvolution. In this case, the transformation is performed making use of the equivalence between the two distributions given by

$$N(\theta_m, \theta)d\theta \equiv N(E_m, E')dE' \qquad (4.13)$$

where $N(\theta_m,\theta)$ is the distribution of scattering angles and $N(E_m,E')$ is the energy distribution for Compton scattered photons. The photon energies E_m and E' correspond to the Compton scattering angles θ_m and θ. After the transformation the differential cross-section for Compton scattering and the distribution of scattering angles are related by

$$N(\theta_m,\theta) = N(E_m,E') \left.\frac{dE'}{d\theta}\right|_{E',\theta}$$

$$= \alpha \cdot \left.\frac{d\sigma}{d\Omega}\right|_{\theta} \cdot I(\theta) \cdot \sin\theta \left[\int_{\phi_1(\theta_m,\theta)}^{\phi_2(\theta_m,\theta)} \phi\right] \qquad (4.14)$$

$$= \alpha \cdot \frac{d\sigma}{d\Omega}_{\theta} \cdot w(\theta_m,\theta)$$

where $w(\theta_m,\theta) = I(\theta) \cdot \sin\theta \cdot \left[\int_{\phi_1}^{\phi_2} \phi\right]$

The factor $I(\theta)$ represents the contribution of the incident photon beam distribution for the ray at θ. In the above equation α denotes a constant and ϕ_1 and ϕ_2 are the limits of effective azimuthal angles. The differential cross-section for Compton scattering is practically a constant for

a spread of about 2° in our range of scattering angles and hence we have

$$N(\theta_m, \theta) = \alpha' w(\theta_m, \theta) \tag{4.15}$$

where α' is a constant.

The distribution function $w(\theta_m, \theta)$ may be normalized numerically such that

$$\sum_{\theta} w(\theta_m, \theta)\,\delta\theta = 1 \tag{4.16}$$

It appears to be the first time this angular resolution function for scattering angles was deduced experimentally and used for the analysis of the data.

The spectra of photons scattered from aluminum at 3.5°, 6.0° and 8.0° were used for the shape analysis. Typical energy distributions of scattered gamma rays for 1408-keV are presented in Fig. 4.4 and for comparison the detector response to 1460-keV gamma rays is also included. The cases of Compton peaks for all energies greater than or equal to 779-keV and of widths larger than the detector FWHM were analysed. In all the cases analysed, the data fitted well with the model function given by (Fig. 4.4a)

$$w(\theta_m, \theta) = \frac{1}{W}\left(1 - \left|\frac{(\theta_m - \theta)}{W}\right|\right) \tag{4.17}$$

4.4 Energy spectrum of 1408-keV gamma rays scattered aluminum

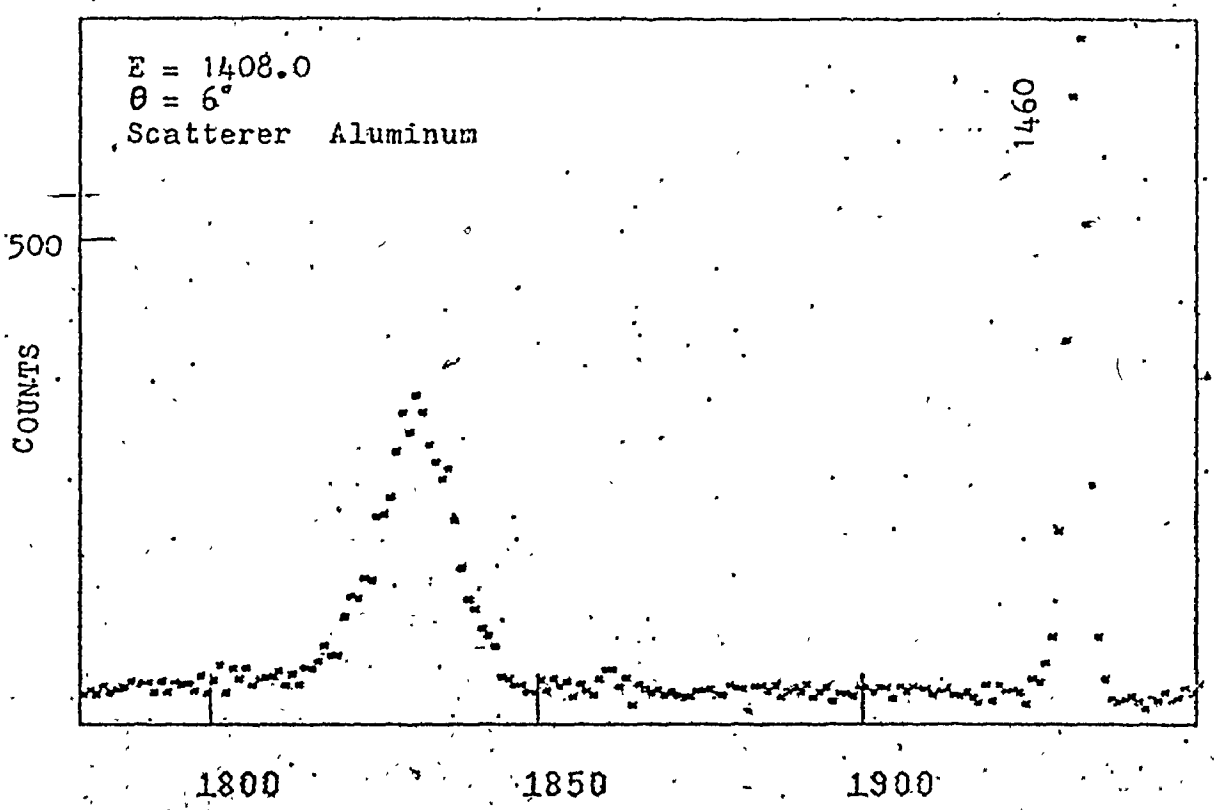

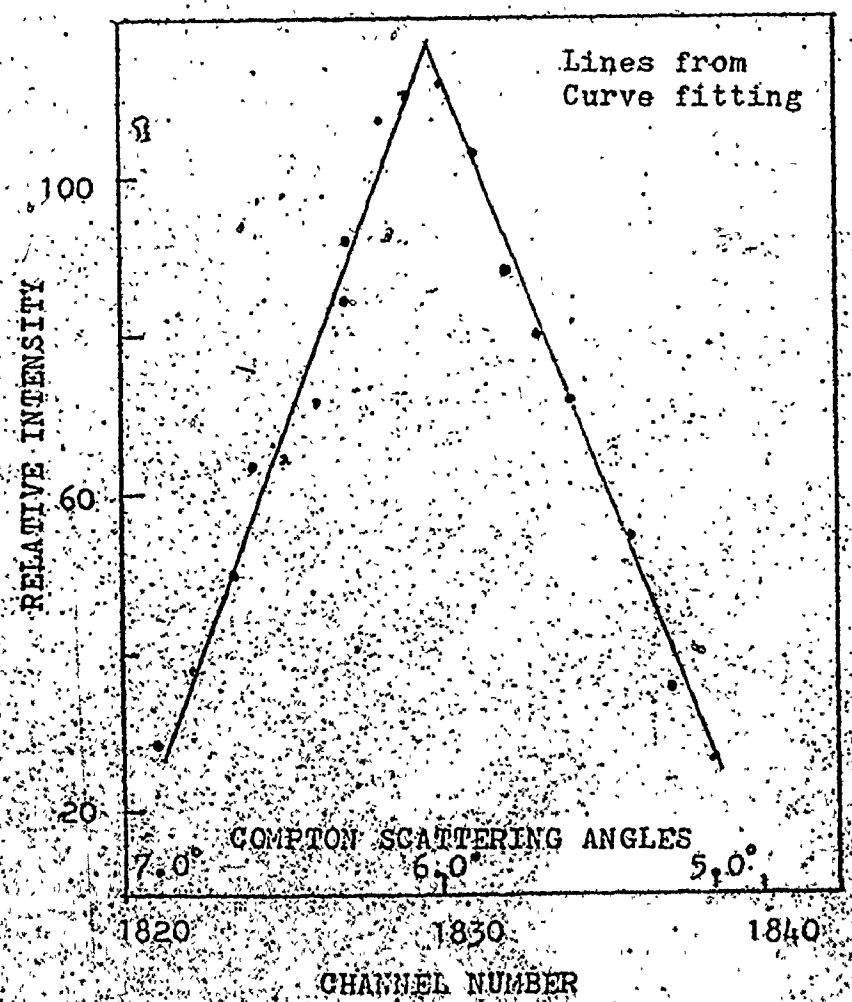

Fig. 4.4(a) Angular resolution function deduced from the above data

where W was found to be equal to $1.5^{o} \pm .1^{o}$. It may be mentioned that this function must be convolved with the detector response in any application or for comparison. The consistency of the parameters θ_m^* and W deduced from the spectra for different energies, angles and thicknesses of the scatterer tended to confirm the validity of this simple and fruitful approach.

6. Separation of coherent and incoherent components

The scattered radiation from the elements of high atomic number, unlike from aluminum, has a strong coherent component even for energies as high as 1408-keV (Fig. 4.5). When the scattering angle is sufficiently small, the incoherent and coherent components overlap in the experimental energy distribution spectrum. For these particular cases, a method to extract the individual components was devised using the empirical model for the angular resolution function.

The model line shape for the scattered photons can be written as

$$S(E,E_m,E_o) = A.C(E,E_m) + B.\delta(E-E_o) \qquad (4.18)$$

where $C(E,E_m)$ is the angular resolution function transformed

Fig. 4.5(i) Energy spectrum of 1408-keV gamma rays scattered by 3.5° off lead

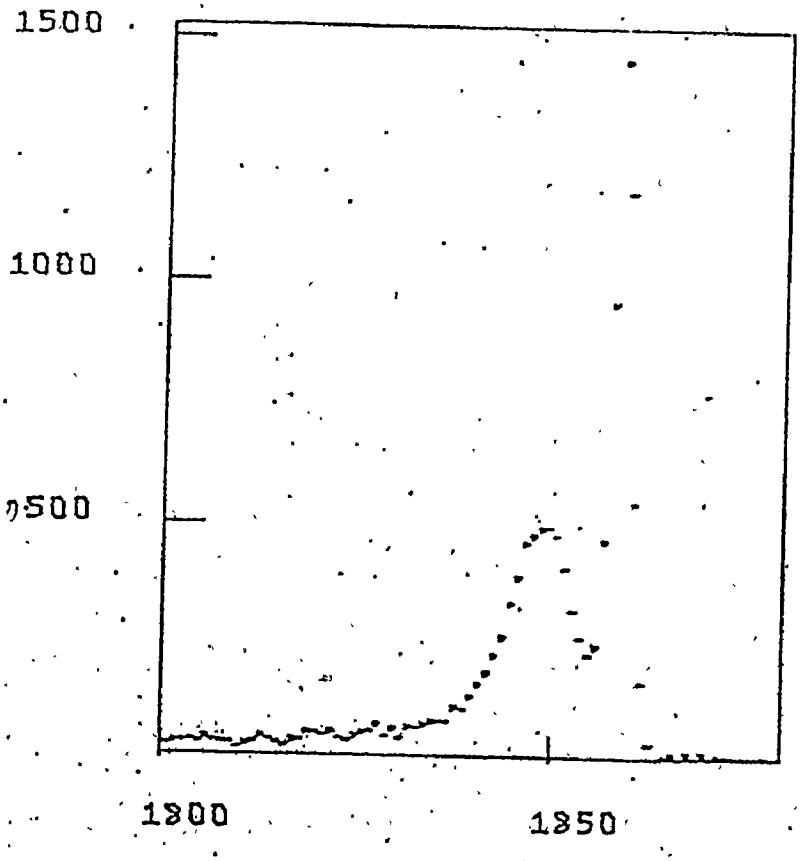

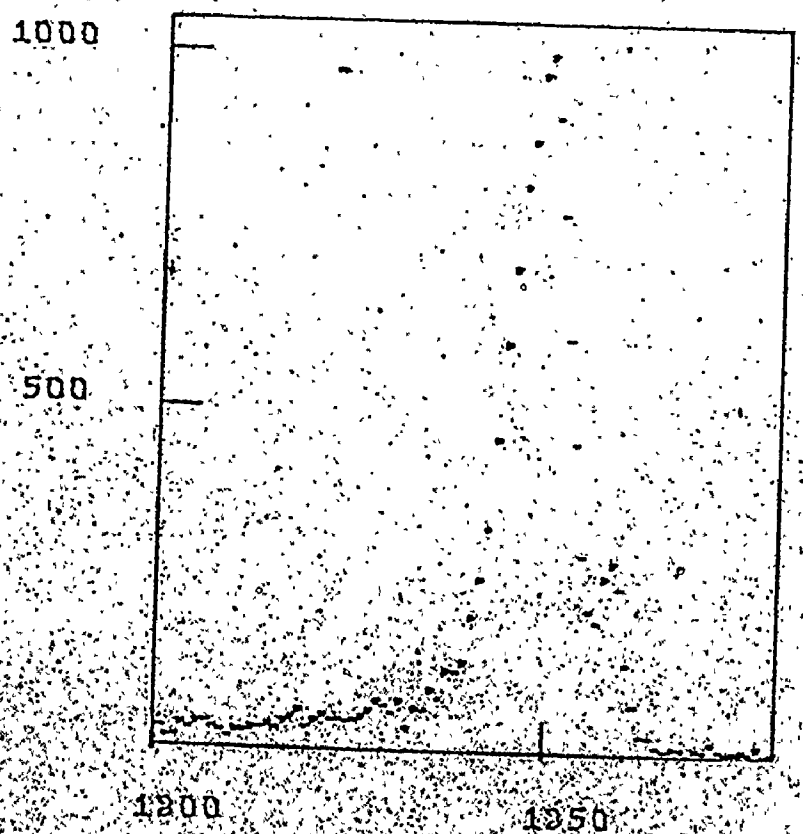

Fig. 4.5(ii) Energy spectrum of 1408-keV gamma rays scattered by 3.5° off copper

into an energy distribution from

$$C(E,E_m) = \alpha w(\theta_m,\theta) \cdot \left[\frac{d\theta}{dE}\right]_{E,\theta} \qquad (4.19)$$

with α being a normalisation factor.

In the above expression, A and B represent the component intensities while C and δ represent normalised distributions for incoherent line shape and delta function distribution with the centre at E_o, the incident energy of the photon.

The shape of S is presented in Fig. 4.6. This model shape is to be convolved with the detector resolution function $R(E,E_o,\sigma)$. This represents a distribution with the peak position at E_o and a parameter representing the width of the distribution σ. This resolution function is adequately represented by a Gaussian as

$$R(E,E_o,\sigma) = \frac{1}{\sigma\sqrt{2\pi}} e^{-\frac{(E-E_o)^2}{2\sigma^2}} \qquad (4.20)$$

Then the total model function $Y_T(E)$ is obtained by convolving S with R as,

$$Y_T(E) = R*S(E,E_m,E_o) \qquad (4.21)$$

$$= A \cdot R*C(E,E_m) + B \cdot R*\delta(E,E_o)$$

(symbol * denotes convolution operation)

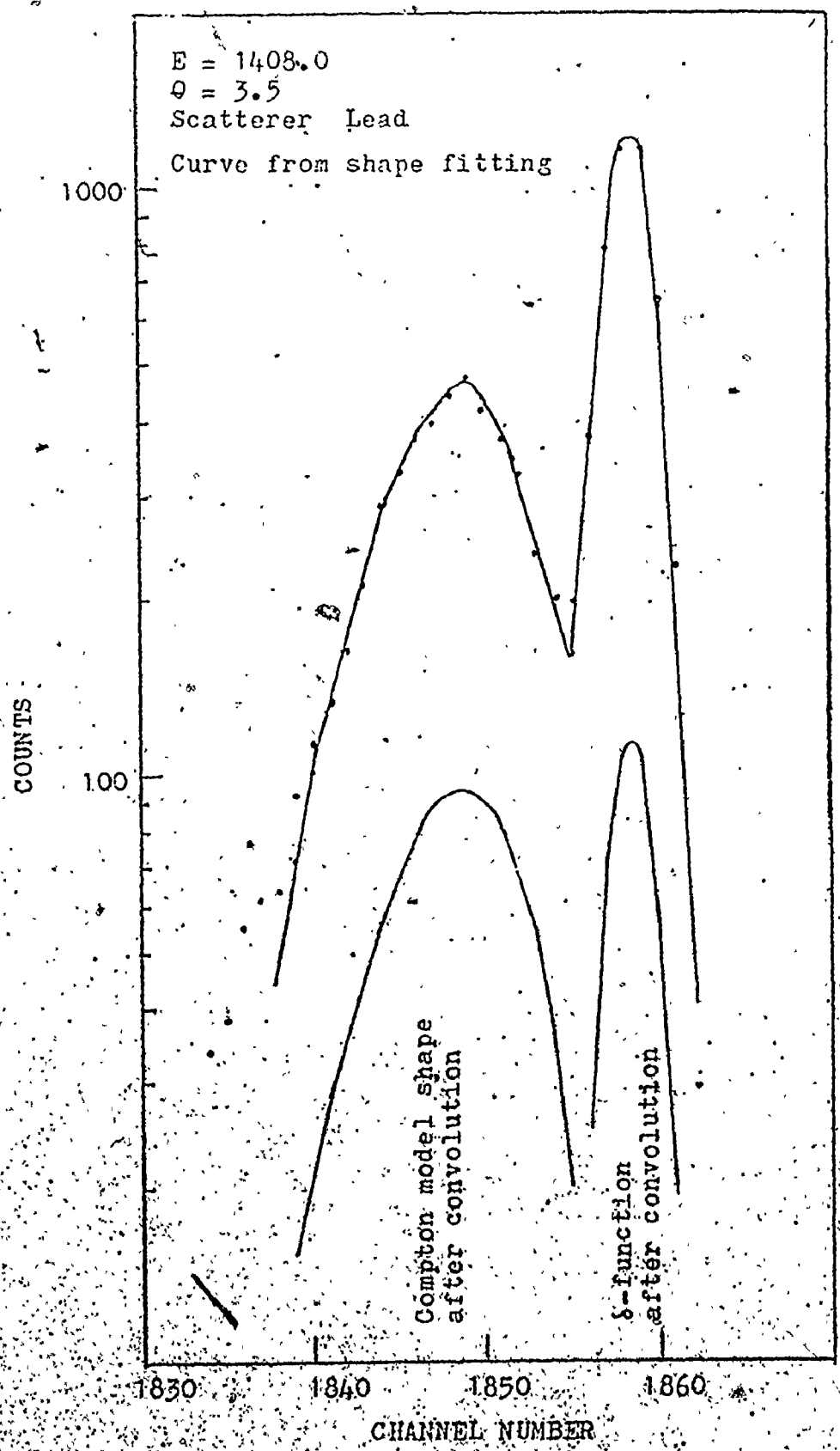

Fig. 4.6 Model function for the coherent and Compton components and the fitted line shapes

TABLE 4.1

Ratio of coherent to total intensity, at 2.3°

	CADMIUM SCATTERER					
E(keV)	thickness 0.44cm		0.88cm		1.32cm	
1408	0.47,	3.5%	0.48	2.9%	0.50	3.1%
1274	0.51	6.3	0.57	3.8	0.51	5.8
1112	0.62	4.3	0.70	2.5	0.69	2.2
1086	0.58	9.0	0.65	3.4	0.59	7.7
964	0.75	3.7	0.79	1.9	0.77	2.4
779	0.87	4.1			0.86	2.2

This distribution was fitted with the experimental peak to extract the parameters A and B representing the coherent and incoherent intensities. The method of weighted linear least-squares was used for fitting the model and experimental shapes. The uncertainties in the fit-parameters A and B were calculated using variance-covariance matrix analysis. The ratio of A to the total peak intensity from the peak area analysis and the ratio of B to total intensity were compared between different runs and different thicknesses for the same angle, energy and element. These ratios were in good agreement, for example refer to Table 4.1. Thus the suitability of this procedure was monitored for each case at every step.

7. Angular resolution correction to coherent scattering cross-sections

Incoherent scattering cross-sections, for $0.4<x<10.0$ vary with angle only by a small percent and hence the finite geometry of the system has very little effect in changing the value of the cross-section at the mean angle. The coherent scattering cross-sections, according to Franz's simple estimate [FR 36] might have a simple angular dependence

of the form $[\sin\theta/2]^{-n}$ with n lying between 0 and 3 depending on the momentum transfer. Though this dependence is not good enough for a rigorous comparison with the experiment, this still brings out the importance of the scattering angle. From this one might infer that the scattering angles smaller than the mean angle would tend to increase the value at the mean scattering angle. Hence a proper method is necessary to take into account the experimental distribution of scattering angles in calculating the differential scattering cross-section at the mean angle. However, this correction does require some assumption about the shape of the angular distribution itself. As a first approximation the form-factor based cross-sections computed from the tables of Hubbel et al. [HU 75] were used to derive these correction factors. Unless there is a large discrepancy between experimental and form-factor based theoretical shapes of the angular distribution function, these corrections may be valid. Hence this estimate of correction is not expected to be unrealistic.

Let the theoretical cross-section $\frac{d\sigma(\theta_o)}{d\Omega}$ be given by

$$\frac{d\sigma(\theta_o)}{d\Omega} = r_o^2 \cdot F^2(x) \frac{(1+\cos^2\theta_o)}{2} \tag{4.22}$$

with $x = \frac{\sin\theta/2}{\lambda}$.

The experimentally observable cross-section, if the angles were distributed according to $w(\theta_o,\theta)$, can be written as

$$\frac{d\sigma(\theta_o)}{d\Omega}_{COH,EXP} = r_o^2 \frac{\sum_{i=1}^{n} F^2(x_i)\left(\frac{1+\cos^2\theta_i}{2}\right) \cdot w_i(\theta_o,\theta_i)\Delta\theta_i}{\sum_{i=1}^{n} w_i(\theta_o,\theta_i)\Delta\theta_i} \tag{4.23}$$

where n denotes the number of angular intervals θ_i chosen for integration and $x_i = \left(\frac{\sin\theta i/2}{\lambda}\right)$.

The value of n used was 199 to cover a span of 3^o, from $(\theta_o - 1.5^o)$ to $(\theta_o + 1.5^o)$ centering around the mean scattering angle θ_o. The computations were checked for the convergence of the integral by varying the number of intervals.

If $\frac{d\sigma(\theta_o)}{d\Omega}$ represents the uncorrected experimental differential cross-section, then the corrected cross-section is obtained from

$$\frac{d\sigma(\theta_o)}{d\Omega}_{CORR,COH} = \frac{d\sigma(\theta_o)}{d\Omega} \cdot \frac{\frac{d\sigma(\theta_o)}{d\Omega}_{COH}}{\frac{d\sigma(\theta_o)}{d\Omega}_{COH,EXP}} \qquad (4.24)$$

In the numerical computation F(x') was calculated for each x' by linear interpolation from tables of Hubbel et al. [HU 75]. Thus an attempt was made to estimate the correction due to the angular resolution function as accurately as possible. The ratios of $\frac{d\sigma}{d\Omega}_{COH,EXP}$ to $\frac{d\sigma}{d\Omega}_{COH}$ are tabulated [cf. Table 4.2] for all energies and angles for which measurements were made in this investigation.

8. Source photon strength factor (K)

This factor gives the relative number of photons of each energy incident on the target. This is a constant for each source-line (energy) for <u>all</u> angles. Hence it is possible to extract this set of numbers from the angular distribution data for a pure Compton scatterer. Of the elements used in these experiments, carbon has the lowest K-shell electron binding energy (0.284 keV) and can be

TABLE 4.2

ANGULAR RESOLUTION CORRECTION

Ratios of corrected cross-sections to theoretical values $\frac{d\sigma}{d\Omega_{COH,EXP}} / \frac{d\sigma}{d\Omega_{COH}}$

1. LEAD

Photon energy (keV)	Mean scattering angles 2.4°	3.5°	5.1°	6.0°	8.0°	10.0°
1408.0	1.05	1.11	1.11	1.01	1.00	1.08
1274.2	1.07	1.02	1.02	1.04	1.01	1.00
1112.0	1.08	1.00	1.01	1.03	1.00	1.00
1085.8	1.08	1.00	1.02	1.01	1.01	1.00
964.0	1.08	1.01	1.08	1.00	1.01	1.01
778.9	1.06	1.04	0.99	1.02	1.00	1.00
443.9	0.98	1.00	1.02	1.01	1.01	1.00
344.3	0.98	0.99	1.02	1.03	1.01	1.00
244.7	0.97	1.00	1.00	1.00	1.00	1.00

2. TANTALUM

	2.4°	3.5°	5.1°	6.0°	8.0°	10.0°
1408.0	1.03	1.18	1.05	1.01	1.00	1.09
1274.2	1.02	1.05	1.01	1.02	1.03	1.00
1112.0	1.02	1.02	1.02	1.01	1.00	1.00
1085.8	1.02	1.02	1.04	1.00	1.00	1.00
964.0	1.05	1.02	1.12	1.00	1.01	1.02
778.9	1.08	1.00	1.00	1.03	1.00	1.00
443.9	0.99	1.02	1.01	1.00	1.02	1.00
344.3	0.97	1.00	1.03	1.02	1.00	1.01
244.7	0.97	0.99	1.01	1.01	1.00	1.00

TABLE 4.2
(cont'd)

ANGULAR RESOLUTION CORRECTION

Ratios of corrected cross-sections to theoretical values

3. CADMIUM

Photon energy (keV)	Mean scattering angles 2.4°	3.5°	5.1°	6.0°	8.0°	10.0°
1408.0	1.17	1.03	1.11	1.08	1.00	1.02
1274.2	1.19	1.00	1.02	1.05	1.03	1.00
1112.0	1.15	1.03	1.00	1.03	1.03	1.00
1085.8	1.12	1.05	1.00	1.02	1.05	1.00
964.0	1.08	1.08	1.02	1.00	1.02	1.02
778.9	1.01	1.09	1.00	1.00	1.00	1.01
443.9	1.00	0.98	1.02	1.02	1.03	1.00
344.3	1.01	0.99	1.00	1.02	1.03	1.01
244.7	0.99	1.01	1.00	0.99	1.00	1.00

4. COPPER

	2.4°	3.5°	5.1°	6.0°	8.0°	10.0°
1408.0	1.14	1.23	1.04	1.00	1.00	1.07
1274.2	1.06	1.09	1.00	1.01	1.01	1.00
1112.0	1.01	1.08	1.03	1.01	1.00	1.00
1085.8	1.00	1.10	1.05	1.00	1.00	1.00
964.0	0.98	1.08	1.14	1.01	1.00	1.01
778.9	1.02	1.01	1.03	1.04	1.00	1.00
443.9	1.08	1.02	0.99	1.00	1.06	1.00
344.3	1.03	1.05	1.01	1.00	1.01	1.02
244.7	0.97	1.03	1.02	1.01	1.00	1.00

considered to be an ideal Compton scatterer, for most of the cases of momentum transfers (> 0.6). First, the carbon scattering count-rate (c.p.m) was analysed and corrected for target self-absorption, change in efficiency due to the degradation in energy of the Compton scattered photons, and for the decay of the source strength. The ratios of corrected experimental data and calculated Compton scattering differential cross-sections were computed for every angle of measurement. For momentum transfers x less than 0.6, theoretical Rayleigh and incoherent scattering cross-sections [Hu' 75] were computed and added to obtain the cross-sections comparable to observable ones. The ratios obtained were averaged for each energy and this average value represents the relative source photon strength for that photon incident energy. In fact this value relates the experimental data to differential scattering cross-sections. Using these deduced strength factors, all the experimental data were converted into scattering cross-sections, for comparison with theory and previous experiments. The ratios of count-rates to Compton cross-sections and the source photon strength factors are given in Table 4.3.

TABLE 4.3

Source photon strength factors

E_γ (keV)	2.4°	3.5°	5.1°	6.0°	8.0°	10.0°	K	K^{-1}
1408.0	46.0	44.3	45.5	46.7	47.2	47.7	46.3±2.6%	0.0216
1274.2	13.8	15.6	13.5	13.1	15.6	13.9	14.2±7%	0.0704
1112.0	35.9	35.8	34.3	36.0	35.6	37.7	35.9±3.2%	0.0278
1085.8	33.4	30.4	33.1	32.0	31.0	31.2	32.3±3.5%	0.0310
964.0	42.1	42.1	44.7	41.6	42.9	43.4	42.8±3.2%	0.0234
778.9		44.8	48.1	45.2	47.4	45.7	46.3±3%	0.0216
443.9		22.0	21.5	20.8	21.4	21.2	21.1±2.4%	0.0474
344.3		179	179	175	186	176	179 ±2.4%	0.00559
244.7		66.6	70.8	62.2	69.5	69.4	67.7±5%	0.0148

Table : Ratio of corrected experimental count-rates (cpm) to Compton scattering cross-sections ($b/_{Sr}$) for carbon.

Legend : K denotes the source photon strength factor
Data statistical errors $\leq$ 3%

9. Efficiency correction for Compton scattered photons

The energy of a photon, after being scattered by "free" electrons, is less than the initial energy. The efficiency of a radiation detector, (a Ge(Li) counter in this case) is energy dependent. The Compton scattered photons are more efficiently absorbed by the detector than the elastically scattered ones. The actual energy lost by the photon depends on the initial energy and scattering angle. A relative efficiency correction was performed to account for the change in efficiency relative to the energy unmodified photons. Energy-shifts are tabulated for each energy and angle (Table 4.4). A weak auxiliary Eu-source was placed at the target position and a source spectrum was collected until the desired statistics ($\sim$ 1%) were achieved. The detector and weak source geometry was maintained the same as for the regular scattering experiment. The peak area for each energy was computed. The ratio of this are to the standard tabulated source-line intensity [Ri 70], BO 74] yields an estimate of the relative efficiencies. The ratios were normalised to the value of 1112-keV line set to unity. A plot of the variation in relative efficiency with energy is presented in Fig. 4.7. These experimental

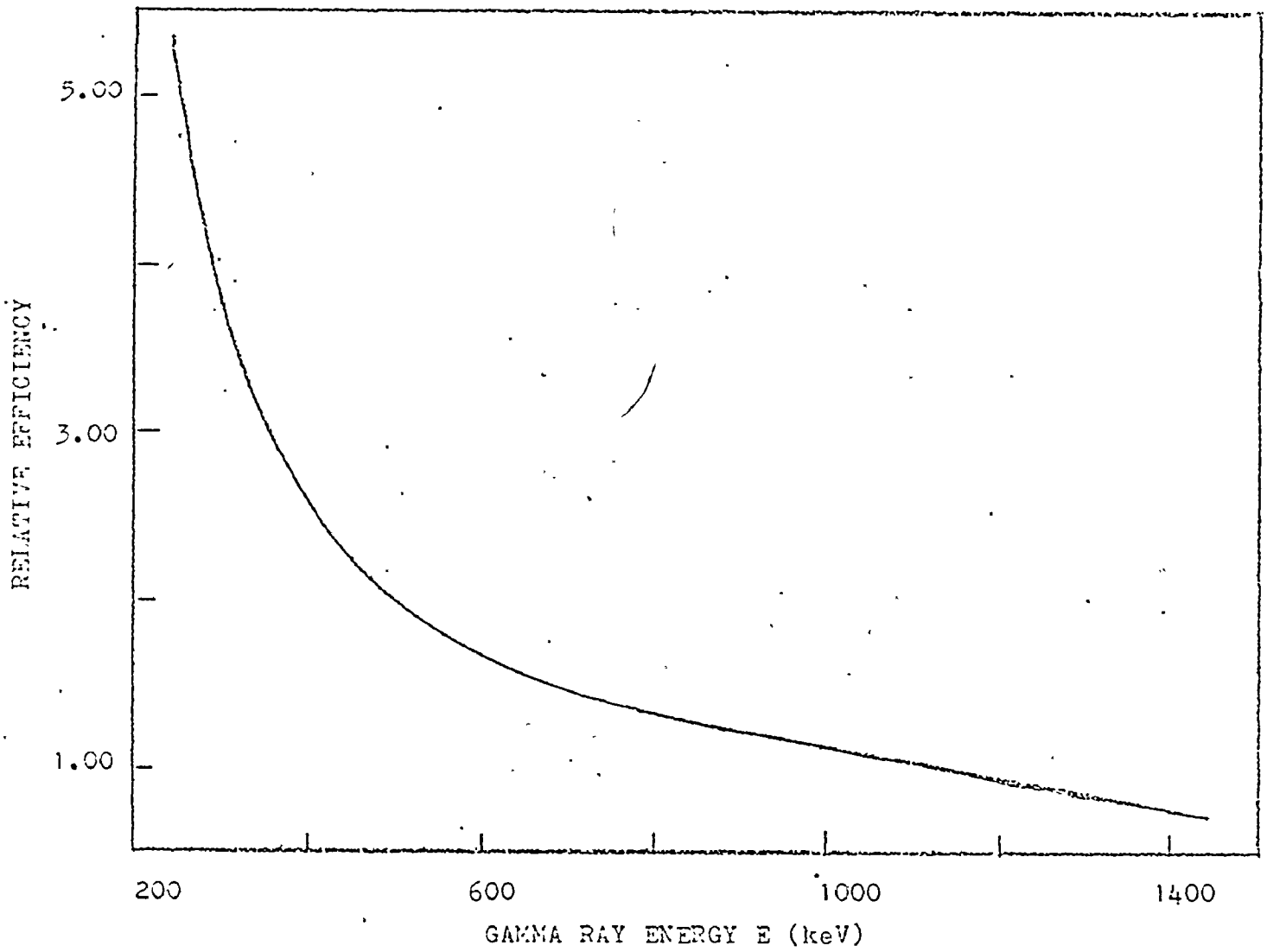

Fig. 4.7 Relative efficiency of the Ge(Li) detector used

TABLE 4.4

Scattering angle	2.4°	3.5°	5.1°	6.0°	8.0°	10.0°
$E_{incident}$ (keV)						
1408.0	3.4	7.3	15.3	21.1	37.1	57.1
1274.2	3.0	6.2	12.8	17.5	30.7	47.2
1112.0	2.1	4.5	9.6	13.2	23.3	35.9
1085.8	1.8	4.1	9.0	12.4	22.0	34.1
964.0	1.6	3.4	7.2	10.0	17.6	27.1
778.9	1.1	2.2	4.7	6.5	11.5	17.8
443.9	0.3	0.7	1.5	2.1	3.8	5.8
344.3	0.2	0.4	0.9	1.3	2.3	3.5
244.7	0.1	0.2	0.5	0.6	1.1	1.8

Energy shifts for Compton scattered gamma rays in keV

TABLE 4.5

Relative efficiencies of the detector used for Compton Scattered photons

Photon incident energy (keV)	Mean scattering angles					
	2.4^{o}	3.5^{o}	5.1^{o}	6.0^{o}	8.0^{o}	10.0^{o}
140.80	1.00	1.01	1.02	1.02	1.04	1.06
1274.2	1.00	1.01	1.01	1.02	1.03	1.04
1112.0	1.00	1.00	1.01	1.01	1.02	1.03
1085.8	1.00	1.00	1.01	1.01	1.02	1.03
964.0	1.00	1.00	1.01	1.01	1.02	1.02
778.9	1.00	1.00	1.01	1.01	1.01	1.02
443.9	1.00	1.00	1.00	1.00	1.01	1.02
344.3	1.00	1.00	1.00	1.00	1.01	1.01
244.7	1.00	1.00	1.00	1.00	1.01	1.01

values were fitted by a least-squares procedure to an inverse polynomial function. Using the fitted coefficients, relative efficiencies were calculated for energy-modified gamma rays for every angle. Only the Compton peak energies were used for computation. Even though the Compton peaks were considerably wider (unlike elastic peaks), the use of peak energies was justified by the fact that the peaks could be considered to be symmetric and any increase in efficiency for the low-energy part of the peak would compensate for a decrease for the high-energy side. Thus this correction is sufficient for the total Compton peak area. It is to be noted (Table 4.5) that this correction is very small except for higher energies and larger angles.

10. Tabulation of experimental data

Experimental differential scattering cross-sections, using the carbon data for normalisation are presented in Tables 4.6 and 4.7. If the relative error in experimental count-rate is σ_e (in percent) and photon strength factor for the particular energy has a relative error σ_{cn} then the total relative error is given by $\sigma_{exp} = \sqrt{\sigma_e^2 + \sigma_{cn}^2}$.

TABLE 4.6

Experimental Differential Elastic Scattering Cross-sections in Barns/Steradian

1. LEAD

Photon energy (keV)	2.4°	3.5°	5.1°	6.0°	8.0°	10.0°
1408.0	11.0± .4	3.76± .19	1.33± .05	0.95± .08	0.55± .03	0.22± .02
1274.2	13.3±1.0	5.7 ±0.4	1.77± .16	1.26± .15	0.58± .09	
1112.0	17.3± .8	7.8 ± .3	2.83± .11	1.59± .17	0.87± .06	0.60± .06
1085.8	17.2± .7	8.3 ± .6	2.75± .12	1.94± .13		
964.0	23.6± .9	10.6 ± .5	4.3 ± .2	2.48± .26	1.35± .08	0.96± .08
778.9	32.0±3.	14.6 ± .9	8.5 ± .3		2.02± .10	1.11± .10
443.9	100 ± 3	46.4 ±1.4	21.0 ± .8	16.1 ±1.2	9.3 ±0.5	6.94± .35
344.3	165 ± 6	86 ± 3	43.6 ±1.4	32.3 ±1.4	17.2 ±1.0	13.3 ±1.1
244.7	245 ± 16	140 ± 10	83 ± 6	67 ± 5	35.6 ±2.5	26.6 ±1.9

2. TANTALUM

Photon energy (keV)	2.4°	3.5°	5.1°	6.0°	8.0°	10.0°
1408.0	8.3±0.5	2.52± .15	1.13± .05	0.74± .04	0.38± .03	0.15± .02
1274.2	10.6±0.9	3.89± .31	1.63± .16	1.16± .14	0.53± .08	
1112.0	14.3±0.7	5.69± .22	2.06±0.10	1.22± .09	0.69± .06	0.43± .05
1085.8	14.0±0.7	5.8 ± .6	1.86± .11	1.22± .15		
964.0	19.5±1.0	8.6 ± .3	2.91± .12	2.09± .11	1.01± .06	0.62± .07
778.9	27.5±1.4	12.8 ± .5	6.2 ± .2	3.37± .29	1.50± .09	1.09± .11
443.9	84.3± .27	32.2 ±1.2	17.4 ± .6	13.5 ± .6	7.60± .35	4.60± .3
344.3	123 ± 7	66 ± 2	30 ± 1	22.3 ±1.3	14.9 ± .5	9.0 ± .5
244.7	230 ± 16	128 ± 9	59 ± 7	38 ± 4	30 ± 3	19 ± 2

TABLE 4.6
(cont'd)

3. CADMIUM

Photon energy (keV)	2.4°	3.5°	5.1°	6.0°	8.0°	10.0°
1408.2	2.03± .12	0.93± .07	0.26± .01	0.14± .01	0.076± .007	0.049± .007
1274.2	2.63± .21	1.11± .12	0.48± .05	0.25± .04		0.10 ± .02
1112.0	4.27± .16	1.57± .09	0.72± .04	0.35± .04	0.11 ± .02	0.068± .014
1085.8	4.04± .35	1.38± .17	0.71± .04	0.46± .07		
964.0	5.78± .19	2.07± .21	1.18± .05	0.65± .04	0.25 ± .02	0.097± .017
778.9	11.4 ± .5	3.6 ± .2	1.69± .10	1.11± .07	0.47 ± .03	0.24 ± .02
443.9	24.5 ±1.0	12.9 ±1.0	4.8 ± .2	3.6 ± .4	1.69 ± .07	1.29 ± .06
344.3	37.9 ±2.4	22.3 ±1.3	11.0 ±0.6	7.4 ± .4	3.38 ± .20	2.34 ± .14
244.7	62 ± 5	35.7 ±2.5	20.5 ±1.4	18.7 ±1.3	7.80 ± .6	5.7 ± .4

4. COPPER

Photon energy (keV)	2.4°	3.5°	5.1°	6.0°	8.0°	10.0°
1408.0	0.75± .03	0.17± .01	0.087± .005	0.055± .006	0.027± .004	.012± .002
1274.2	1.01± .08	0.28± .03	0.12 ± .02	0.10 ± .02		±
1112.0	1.54± .11	0.37± .03	0.11 ± .01	0.08 ± .01	0.058± .013	
1085.8	1.48± .16	0.49± .03	0.120± .013			
964.0	2.16± .23	0.54± .06	0.16 ± .01	0.14 ± .02	0.058± .013	0.062±.009
778.9	2.57± .20	1.10± .07	0.43 ± .02	0.27 ± .02	0.121± .015	0.071±.009
443.9	5.94± .19	2.73± .11	1.73 ± .07	1.25 ± .07	0.45 ± .02	0.184±.008
344.3	12.1 ± .5	4.6 ± .2	2.3 ± .1	1.95 ± .07	1.34 ± .08	0.88 ±.05
244.7	25.8 ±1.4	12.7 ±1.0	4.2 ± .3	3.0 ± .2	2.50 ± .18	2.03 ±.14

TABLE 4.7

Incoherent scattering cross-sections in barns/Steradian

1. LEAD

Photon Energy (keV)	2.4°	3.5°	5.1°	6.0°	8.0°	10.0°
1408.0	4.36± .25	4.45± .18	4.88± .15	4.83± .43	4.90± .15	4.70± .14
1274.2	4.23± .68	4.43± .35	3.95± .32	3.77± .60	4.21± .38	3.27± .29
1112.0	4.10± .49	3.95± .20	4.07± .16	3.67± .18	4.25± .17	3.98± .16
1085.8	3.10± .32	3.27± .41	4.09± .20	3.96± .24	4.39± .16	4.36± .17
964.0	3.11± .50	3.80± .23	3.98± .16	3.81± .23	4.25± .17	4.02± .16
778.9	4.47± .89	2.44± .29	3.91± .16	3.51± .32	3.70± .19	3.83± .15

2. TANTALUM

Photon Energy (keV)	2.4°	3.5°	5.1°	6.0°	8.0°	10.0°
1408.0	4.22± .34	4.54± .23	4.67± .16	4.56± .36	4.76± .16	4.32± .26
1274.2	4.96± .45	4.42± .40	3.84± .35	3.09± .53	3.65± .33	3.74± .34
1112.0		4.29± .17	3.94± .16	3.48± .35	3.70± .15	4.21± .17
1085.8		3.75± .47	3.85± .19	3.56± .53	4.03± .20	4.04± .20
964.0		3.97± .20	4.03± .16	4.26± .64	4.15± .17	3.87± .16
778.9		3.37± .34	4.04± .16	4.00± .34	4.13± .19	4.30± .17

TABLE 4.7
(cont'd)

3. CADMIUM

Photon Energy (keV)	2.4°	3.5°	5.1°	6.0°	8.0°	10.0°
1408.0	2.42± .15	2.36± .7	2.87± .09	2.78± .17	2.87± .09	2.76± .16
1274.2	2.69± .46	2.59± .31	2.79± .22	2.40± .29	2.78± .22	2.28± .21
1112.0		2.38± .14	2.60± .10	2.81± .17	2.95± .21	2.85± .17
1085.8		1.93± .29	2.67± .11	2.73± .16	2.75± .19	2.82± .17
964.0		2.26± .23	2.94± .12	2.99± .18	3.00± .18	2.69± .16
778.9		1.80± .22	2.55± .09	2.70± .16	2.81± .17	2.86± .17

4. COPPER

Photon Energy (keV)	2.4°	3.5°	5.1°	6.0°	8.0°	10.0°
1408.0	1.61± .07	1.86± .07	1.93± .06	1.92± .06	1.87± .06	1.90± .06
1274.2	1.63± .11	1.84± .15	1.93± .14	1.81± .15	1.69± .14	1.50± .12
1112.0		1.85± .07	1.80± .07	1.75± .07	1.80± .07	1.84± .06
1085.8		1.58± .08	1.77± .07	1.68± .07	1.83± .07	1.80± .07
964.0		1.74± .07	1.93± .07	1.97± .08	2.02± .08	1.89± .06
778.9		1.70± .09	1.76± .06	1.92± .07	1.89± .07	1.87± .06

TABLE 4.7
(cont'd)

5. ALUMINUM

Photon Energy (keV)	2.4°	3.5°	5.1°	6.0°	8.0°	10.0°
1408.0	.98±.06	.96±.06	.93±.05	.89±.05	.98±.06	.88±.05
1274.2	.99±.09	.84±.08	.89±.08	.87±.08	.94±.08	.79±.07
1112.0	.99±.06	1.00±.06	1.01±.06	.96±.06	.99±.06	1.12±.07
1085.8	.93±.06	.95±.06	.98±.06	.96±.06	1.04±.06	1.06±.06
964.0	1.06±.06	.92±.06	.99±.06	.96±.06	.99±.06	.96±.06
778.9	1.16±.07	1.01±.06	.90±.06	.85±.06	.98±.06	.96±.06
*443.9	2.12±.13	1.12±.07	1.09±.06	1.09±.06	1.12±.07	1.14±.07
*344.3	2.61±.10	1.48±.09	1.10±.07	1.07±.06	1.06±.06	
*244.7	4.13±.25	2.35±.16	1.39±.09	1.31±.09	1.37±.09	1.26±.09

* Incoherent + coherent cross-sections

σ_{exp} is given in per cent. σ_e includes the uncertainties in counting statistics, attenuation correction, thickness measurement and background evaluation. Coherent and incoherent data are tabulated separately in units of barns per steradian with errors. A few remarks concerning the resolution of the elastic and Compton components are necessary at this point. The energy shift of Compton scattered gamma rays (cf. Table 4.4) determines the peak-position and the width of the Compton peak primarily depends on the effective angular spread of the photon-beam. Empirically, this width was found to be consistent with a FWHM of 1.5° of a triangular distribution. On the basis of the Compton peak-widths, it was found, for an energy shift of more than 9 keV, both elastic and Compton peaks were well-resolved. For shifts between $\sim$ 2 and 9 keV, least-squares fit procedure (cf. Section 6) was used to extract the components. The Compton components obtained by the fitting procedures from unresolved peaks within 3 channels (corresponding to 2 keV) were unreliable, however, the elastic components formed the major part of the scattered photons in these cases.

For low energies (443.9, 344.3 and 244.7 keV) the Compton components at 10°, and 8° were used to estimate

the elastic part for smaller angles. The Compton cross-section was assumed to be constant for all these angles and the uncertainty in the elastic component, introduced due to this procedure, is very small.

11. Verification of the method of normalisation

In the previous section the procedure used to arrive at the experimental scattering cross-sections on the basis of theoretical cross-sections and experimental count-rates for the carbon scatterer was outlined. The soundness of the procedure can be checked by (i) comparing the experimental scattering cross-sections for aluminum with the theoretical values in the range of x where agreement can be expected and (ii) computing the absolute scattering cross-sections from the experimental parameters for carbon. Because of the low electron binding energies for aluminum (e.g. K-electron binding energy = 1.5 keV) one would expect it to behave as a pure Compton scatterer, for $x \gtrsim 0.4$. Convincingly enough, it was found that the weighted mean ratio of experimental to theoretical cross-sections [HU 75] is 1.00 ± .01.

The absolute scattering cross-sections were obtained

from an experiment to scan the photon beam-profile (cf. Chapter 3.3 and also Figures 3.4a and 3.4b) and a measurement of relative efficiency using an auxiliary weak europium source.

Absolute scattering cross-sections can be computed as follows. For a scatterer with no absorption, the count-rate of scattered photons observed may be written as (cf. eq. 4.3)

$$I = I_o \, \Delta\Omega_t [N_t . t . \frac{d\sigma(\theta)}{d\Omega}] \cdot \Delta\Omega_D \cdot \varepsilon_R \qquad (4.25)$$

where

I_o is the rate of number of photons emerging from the source per unit solid angle, as observed by the same detector

$\Delta\Omega_t$ the target-to-source solid angle

$\Delta\Omega_D$ the detector-to-target solid angle

t the thickness of scatterer of N_t atoms/cc. and

ε' the relative efficiency of the detector to the scattered photons or the ratio of efficiency for scattered photons to that of the incident photons.

In this expression, all other factors are known except I_o and $\frac{d\sigma}{d\Omega}$. By experimentally measuring I_o the absolute value of $\frac{d\sigma(\theta)}{d\Omega}$ can be deduced. It is difficult to measure I_o directly since the rate would be too high for the detection system. The photon beam was scanned using a 0.25" aperture in front of the detector, which was shielded otherwise. The photon-source was moved through different positions (or angles) on either side of the zero position and in each position the source spectrum was recorded. Thus the detector was allowed to look at only a part of the photon beam. It may be noted that only a portion of the detector faced the photon-beam. An auxiliary weak europium source was placed in target position and spectra were recorded with and without this special aperture in front. The ratio of these two count rates for each photon-energy gives the relative efficiency of the full detector to the detector with only a 0.25" aperture. Then we have,

$$I_o = (\Delta\Omega'_D)^{-1} \varepsilon[\Delta r \Sigma p(r).r] \times 2\pi \qquad (4.26)$$

where $\Delta\Omega'_D$ is the detector-source solid angle

$p(r)$ is the photon countrate for a particular energy when the source was positioned at a distance r from the zero-position

Δr the distance interval between positions

and ε the ratio of countrates without and with 0.25" aperture in front of the detector in the auxiliary source experiment.

The value of ε was found to lie between 39.0 and 41.3 for the range of energies above 778.9 keV. Typical source countrate distribution is presented in Fig. 4.8. For carbon, the cross-sections obtained using source-photon strength factors and those based on the source-scan measurements agreed well within 5% for energies between 1408- and 778.9-keV [Table 4.8]. Incoherent scattering cross-sections for carbon have almost a constant value in this range of energies and angles and so the correction due to the finite angular interval and distribution of angles in this interval is not expected to be important.

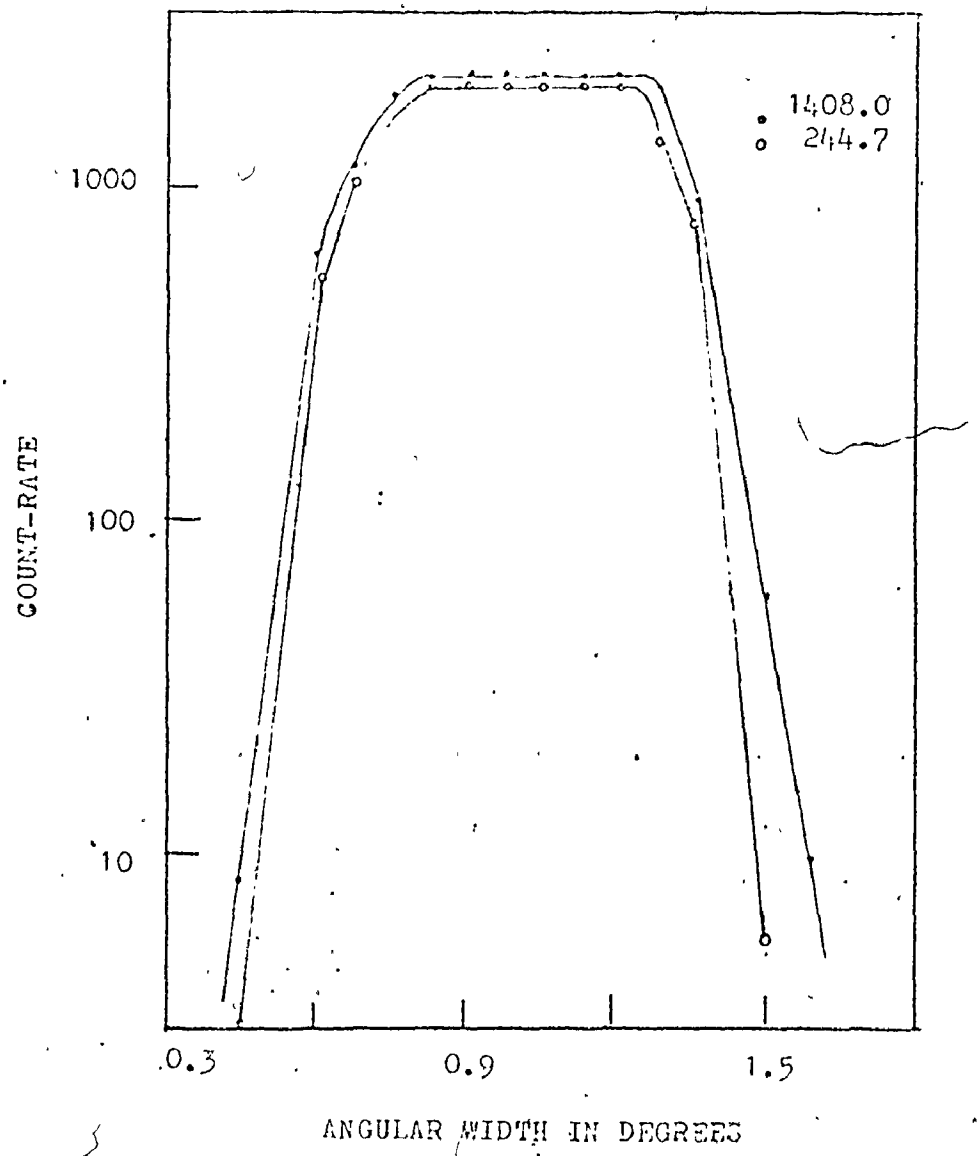

Fig. 4.8 Experimental source photon beam angular profile

TABLE 4.8

Carbon differential scattering (incoherent) cross-sections

E_r	Method	2.4°	3.5°	5.1°	6.0°	8.0°	10.0°
1408	1	0.465	0.445	0.450	0.455	0.447	0.433
	2	0.469	0.450	0.454	0.459	0.451	0.438
1274	1	0.476	0.533	0.454	0.437	0.505	0.437
	2	0.464	0.519	0.441	0.426	0.490	0.423
1112	1	0.491	0.486	0.459	0.477	0.459	0.470
	2	0.473	0.468	0.444	0.459	0.444	0.454
1086	1	0.516	0.511	0.460	0.496	0.468	0.440
	2	0.489	0.485	0.438	0.470	0.440	0.418
964	1	0.493	0.490	0.515	0.474	0.478	0.468
	2	0.468	0.463	0.486	0.448	0.453	0.444
779	1	0.581	0.517	0.549	0.511	0.526	0.494
	2	0.561	0.460	0.489	0.455	0.468	0.440

Method 1 : Absolute cross-sections based on experimental source beam scan measurements

Method 2 : Cross-sections computed using source-photon strength factors

CHAPTER 5

RESULTS AND DISCUSSION

1. Rayleigh scattering

(a) Some details of previous investigations

There have been a number of measurements of differential elastic scattering cross-sections in recent years [DI 68, SC 69, HA 71, SC 73a, SC 73b] employing high resolution Ge(Li) detection systems. All these measurements were performed for large momentum transfers ($x>10$) and involved large scattering angles. Considerable experimental work on small angle scattering had been done since 1950 and in all these measurements low resoltuion detection systems were used.

Storruste measured scattering cross-sections for lead, copper and aluminum using 410-keV gamma rays and the NaI detection system for many scattering angles between 3° and 40° [ST 50]. Around 40°, the Compton scattering was expected to be the dominant component of the scattered radiation. Using the measured absolute scattering cross-section for angles in this range the Compton cross-sections for smaller angles were obtained by extrapolation. Then the Rayleigh scattering cross-sections were deduced from

the observed cross-sections by subtracting the extrapolated Compton component. Mann conducted an investigation using 411-, 662-, and 1330- keV gamma rays in the range of scattering angles between 15^{o} and 90^{o} [MA 56]. It was found for 411- and 662- keV lines that the experimental cross-sections disagreed with the theoretical values based on the form-factor approximation using Dirac wave-functions with the inclusion of only K- and L- shell electrons. In an interesting experiment using Co^{60} gamma rays (average energy 1250-keV) Rayleigh scattering cross-sections were measured [BE 60] for small angles in the intervals 15' to 1^{o} and 15' to $2^{o}30'$. The experimental cross-sections were found to follow a Z^{2}- dependence and the values were higher than the theoretical predictions for high Z- scatterers. The theory compared was based on a form-factor approximation given by Debye and Franz [DF 30, FR 35]. Moreover, the measurements on tantalum yielded anomalously high coherent scattering cross-sections and for nickel (Z = 28) the experimental values were markedly lower than those for copper (Z = 29).

A valuable set of absolute coherent scattering cross-section measurements was carried out by Nath and Ghose

[NA 64] for small scattering angles (1^{o} - 12^{o}) on lead, tin and copper using 279-, 662-, 1170-, and 1330-keV gamma rays. The incoherent component of scattering was taken into account by application of the theoretical values of incoherent scattering function [BE 31]. Their results for the 279-keV gamma rays in lead were in very good agreement with the theoretical coherent scattering cross-sections of Nelms and Oppenheim [NE 55] based on Hartree model wavefunctions and the form-factor approximation. For 662-keV photons scattered by lead their cross-sections were in fair agreement with theory up to 6^{o} and beyond that the experimental values were higher. For Co^{60} gamma rays the data werein good agreement with theory for scattering angles larger than 3^{o} and for smaller angles the theoretical values were found to be higher. For copper the measured coherent scattering cross-sections were considerably lower than the theoretical ones.

An experimental method employing a coincidence technique and a source of annihilation radiation (511-keV) was used by Hauser and Mussgnug [HA 66]. They attempted to measure elastic scattering cross-sections for elements with the atomic numbers (Z) in the range of 72 to 92.

Their arrangement permitted a very small angular resolution $\sim 0.04^{0}$ and scattering angles $\sim 0.5^{0}$. For $x>2.0$ in lead, their measurements agreed with that of Nath and Ghose but for $x<2.0$ their values were tending towards a constant thereby differing from the form-factor approximation. It is difficult to make a quantitative comparison with all these measurements for two reasons. First these articles did not list the deduced cross-sections numerically and secondly a quantitative evaluation of the agreement or disagreement with the theory was not presented.

(b) Procedure followed for comparison with the theory.

In the earlier experiments [NA 64, KA 61] the small angle coherent scattering cross-sections were considered as a simple function of Z and E. On the assumption that, the differential elastic scattering cross-section be given by

$$\frac{d\sigma(\theta)}{d\Omega} = \frac{Z^{n}}{E^{m}} \; g(\theta)$$

the exponents n and m were extracted from the experimental data. It was found that n varied from 2 to 3 as the momentum transfer increased and that m increased with θ. Since both n and m vary with x it is worthwhile to plot

$\frac{d\sigma}{d\Omega}$ vs. x in a logarithmic scale. Before drawing these graphs the polarisation factor $[(1+\cos^2\theta)/2]$ may be removed and the graphs are presented for $\frac{d\sigma'}{d\Omega}$ (x) vs. x such that (cf. ch. 2.)

$$\frac{d\sigma'(x)}{d\Omega}_{coh.} = r_o^2 |F(x)|^2$$

From figures 5.1, 5.5, 5.9, and 5.13, it is observed that the exponent of x decreases as x decreases thus conforming to the features of the form-factor approximation. For the range of energies between 244.7 and 1408.0-keV tne coherent cross-section momentum transfer plots seem to be rather smooth curves. The theoretical curves of cross-sections were obtained from the form-factor tables of Hubbel et al. [HU 75]. From the tabulated values the form-factor for a particular experimental x was obtained by linear interpolation. These theoretical form-factors supersede the previous calculations of Nelms and Oppenheim [NE 55]. Of course both these computations used Hartree model non-relativistic wave-functions. Nelms and Oppenheim plotted form-factor curves for a few elements and presented the Z-dependence separately.

But the tables of Hubbel et al. are more elaborate and present F(x) vs. x for all the atomic numbers. For this reason the form-factors of Hubbel et al. were compared with the present data in detail. To provide a closer comparison between theory and experimental data a weighted mean ratio $\bar{R}$ was calculated using the formula

$$\bar{R} = \sum_{i=1}^{N} \frac{R_i W_i}{\sum_{i=1}^{N} W_i}$$

where R_i is the ratio of experimental to the theoretical differential scattering cross-section for the i^{th} datum and N is the number of data points. The weight factor for the i^{th} point is given by

$$W_i = \frac{1}{e_i^2}$$

the value e_i^2 being the variance in the experimental datum.

The uncertainty in $\bar{R}$, $e_{\bar{R}}$ can be also obtained from

$$e_{\bar{R}}^2 = \frac{\sum_{i=1}^{N} (R_i - \bar{R})^2 W_i}{(N-1) \sum_{i=1}^{N} W_i} .$$

TABLE 5.1a

Weighted mean ratios of experimental coherent cross-sections to form-factor based theoretical values

Photon energy (keV)	$\bar{R}$ Lead	Tantalum	Cadmium	Copper
1408.0	0.82 ± .02	0.84 ± .02	0.74 ± .02	0.97 ± .05
1274.2	0.82 ± .02	0.89 ± .03	0.83 ± .04	1.02 ± .05
1112.0	0.82 ± .02	0.85 ± .03	0.85 ± .05	0.86 ± .08
1085.8	0.79 ± .03	0.78 ± .04	0.79 ± .03	0.91 ± .09
964.0	0.89 ± .03	0.91 ± .02	0.89 ± .03	0.85 ± .07
778.9	0.83 ± .05	0.89 ± .03	0.88 ± .04	0.95 ± .03
443.9	0.83 ± .03	0.89 ± .04	0.78 ± .03	0.78 ± .05
344.3	0.98 ± .02	0.99 ± .01	0.90 ± .02	0.90 ± .07
244.7	1.01 ± .03	1.08 ± .07	0.93 ± .04	0.99 ± .09
$\bar{R}$ For all points	0.86 ± .01	0.90 ± .01	0.84 ± .01	0.87 ± .02

TABLE 5.1b

Weighted mean ratio $\bar{R}$ for different x-regions

x in $\mathring{A}^{-1}$	$\bar{R}$ Lead
0.41 - 1.1	0.90 ± .04
1.2 - 3.5	0.88 ± .02
3.6 - 6.3	0.78 ± .01
6.4 - 10.0	0.94 ± .04
x in $\mathring{A}^{-1}$	$\bar{R}$ Tantalum
0.41 - 0.6	1.11 ± .07
0.75 - 1.1	0.91 ± .06
1.2 - 4.7	0.89 ± .02
4.8 - 10.0	0.88 ± .02
x in $\mathring{A}^{-1}$	$\bar{R}$ Cadmium
0.41 - 1.25	0.89 ± .02
1.3 - 5.5	0.84 ± .02
5.6 - 10.0	0.68 ± .03
x in $\mathring{A}^{-1}$	$\bar{R}$ Copper
0.4 - 0.6	1.15 ± .06
0.7 - 1.25	0.82 ± .02
1.3 - 10.0	0.88 ± .03

The weighted mean ratios were calculated for all the data points for each element. Similar ratios were also obtained for all angles per energy and for different regions of momentum transfer. Thus a quantitative evaluation of dependence on x and E of $\bar{R}$ was deduced. The empirical power law relationships for E and Z were not attempted since the form-factor calculations are more accurate and readily available. Just direct comparisons with this theory itself were felt to be interesting.

(c) Comparison with the theories and experiments for lead

A comparison of the current set of data of coherent scattering cross-sections with an appropriate set of previous measurements are presented through Tables 5.2 - 5.5. All the other experimenters used different photon energies and hence the momentum transfer $x(=\sin(\theta/2) \cdot \lambda^{-1})$ is used as a basis for comparison. Small angle scattering data are more appropriate in this context since the photon energies involved would be in the same range and a better agreement can be expected. In the case of low energies ($\lesssim$ 100 keV) and large angles, in spite of the same momentum transfer a considerably large absorptive part (related to the photoelectric effect) in the scattering amplitude could have a significant

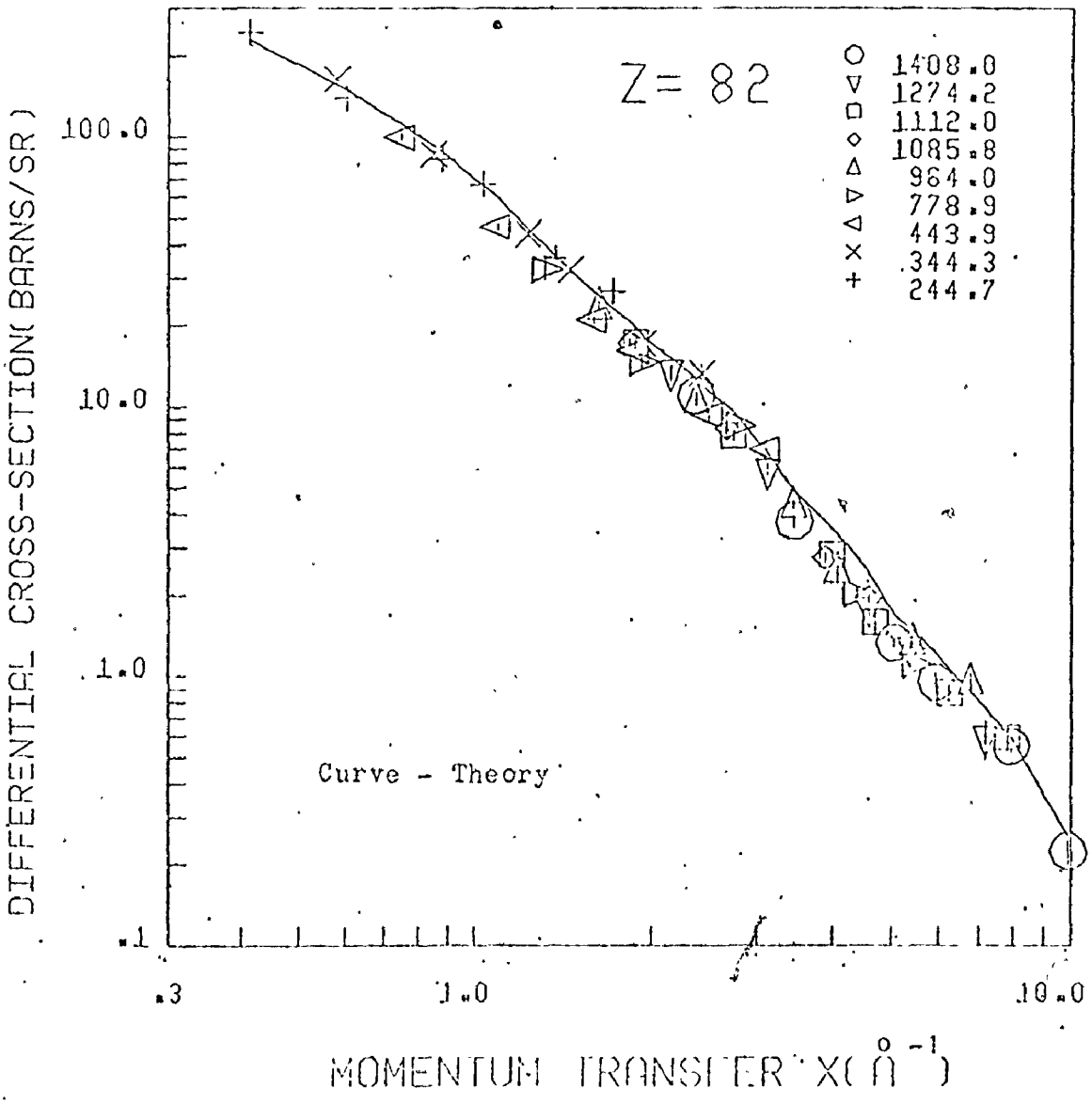

Fig. 5.1 Dependence of coherent differential scattering cross-section on momentum transfer x in lead

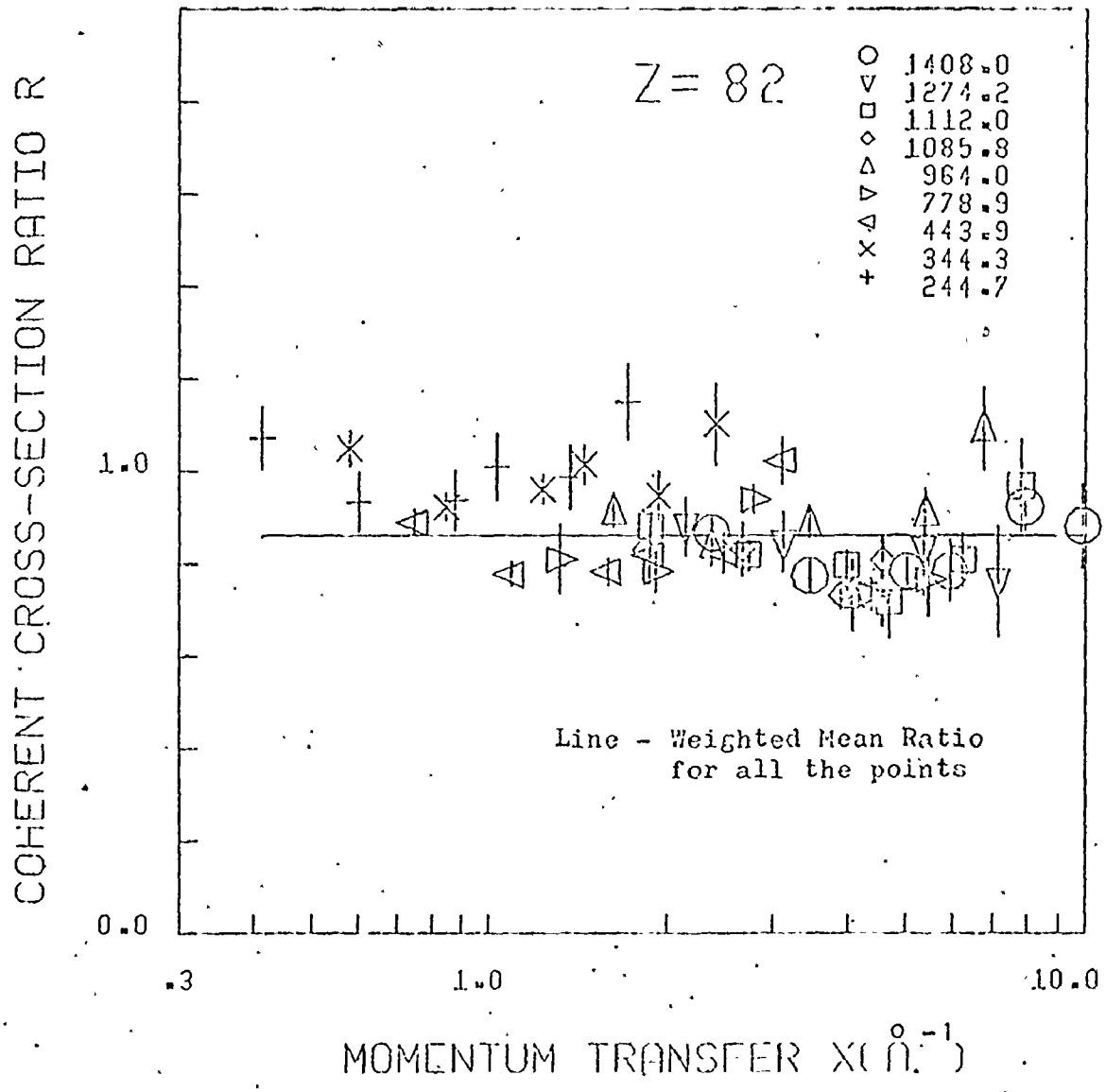

Fig. 5.2 Variation of coherent cross-section ratio with x in lead

TABLE 5.2

Comparison of the experimental coherent scattering cross-section for lead

Momentum transfer	$\frac{d\sigma}{d\Omega}$ in b/Sr	$\frac{d\sigma}{d\Omega}$ in b/Sr present values for closest x
0.41	210 ± 10	244 ± 15
0.75	120 ± 5	100 ± 3
1.25	46 ± 3	4.37 ± 1.4
1.36	36 ± 2.5	35.6 ± 2.5
1.45	27.5 ± .5	32.3 ± 1.4
1.72	28 ± 3	26.6 ± 1.9
1.81	18 ± 2	17.2 ± .7
1.87	19 ± 1	16.1 ± 1.2
2.71	9 ± .8	7.79 ± .34
3.06	6.6 ± .4	6.94 ± .35
3.21	4.68± .2	5.7 ± .4
3.79	3.1 ± .2	2.75 ± .12
4.44	2.2 ± .1	2.02 ± .1
5.43	1.38± .08	1.35 ± .08
6.23	0.98± .15	0.87 ± .06
7.28	0.52± .15	0.58 ± .09
10.0	0.16± .05	0.22 ± .02

TABLE 5.3

Comparison of the experimental total (coherent + incoherent) scattering cross-sections for lead

Momentum transfer x in A^{o-1}	$\frac{d\sigma}{d\Omega}$ (Total) from Storruste and Tjom [ST 58]	$\frac{d\sigma}{d\Omega}$ (Total) Present values for closest x
0.82	100 ± 13	90.3 ± 3
1.08	65.5 ± .9	50.5 ± 1.7
1.47	30.5 ± .4	36.4 ± 1.5
2.36	16.0 ± .2	14.4 ± 0.6
3.13	10.5 ± .14	11.03± .5
3.95	8.05± .1	6.9 ± 0.4
4.73	7.10± .09	5.68± .4

contribution. The present experimental cross-sections agree reasonably well with that of Nath and Ghose [NA 64] while the agreement is not as good with those of Storruste and Tjøm [ST 58]. In the latter case the cross-sections were not corrected for finite angular spread [NA 64]. This correction might be of the order of 10% reducing their values. Then the agreement tends to improve. The experimental scattering cross-sections of Kane et al. [KA 61] including both the coherent and incoherent components are apparently higher than the current values by about 10%. They normalised their values on the basis of the cross-sections of Storruste and Tjøm. If the same renormalisation required for the data of Storruste and Tjøm is applied to the values of Kane et al., the discrepancies are reduced. It may be mentioned that the errors quoted in Tables 5.2 and 5.4 for the data of Nath et al. and Kane et al. might be higher than their true values since those were read off the figures in their papers [NA 64, KA 61]. The plots of Nath and Ghose were magnified by a factor of 2.5 to allow convenient readout. The measured coherent scattering cross-sections for 145-keV at large scattering angles [SC 69] presented in Table 5.5 has progressively higher values

TABLE 5.4

Comparison of the experiment total (coherent + incoherent) scattering cross-sections for lead

Momentum transfer x in A^{0-1}	$\frac{d\sigma}{d\Omega}$ (Total) in $b/_{Sr}$ from Kane et al. [KA 61]	$\frac{d\sigma}{d\Omega}$ (Total) in $b/_{Sr}$ Present values for closest x
2.0	19 ± .2	17.4 ± 1.0
2.94	13 ± .13	11.0 ± .5
3.84	8.3 ± .8	6.8 ± .4
4.38	7.0 ± .7	6.1 ± .4
5.42	5.8 ± .6	5.4 ± .4

TABLE 5.5

Comparison of the experiment coherent scattering cross-sections for lead

Schumacher's data [SC 69]				
Photon energy (keV)	θ^{o}	x in A^{o-1}	$\frac{d\sigma'}{d\Omega}$ in $b/_{Sr}$	$\frac{d\sigma}{d\Omega}$ in $b/_{Sr}$ present values for closest x
145	32	3.22	6.86±.58	6.94±.35
	45	4.47	2.76±.19	2.02±.1
	60	5.85	1.54±.1	0.95±.08
	75^{o}	7.12	1.05±.06	0.58±.09

differing by as much as 80%. The observed cross-sections were multiplied by $2(1+\cos^2\theta)^{-1}$. In fact these values are considerably higher than form-factor based values too. Thus the present set of measurements agree well with the other small angle data comparing on the basis of x.

In the range of x between 0.4 and 10.0 $\mathring{A}^{-1}$ the scattering amplitudes f_N, f_M, f_L and k_K due to N, M, L and K - shell electrons are the important components of the total amplitude F. To estimate which of these is a major contributor to F(x), the f-ratios i.e., the values of $|\frac{f_N(x)}{F(x)}|$, $|\frac{f_M}{F}|$, $|\frac{f_L}{F}|$ and $|\frac{f_K(x)}{F(x)}|$ are computed on the basis of a simple model due to Pauling and Sherman [PA 32]. These estimates plotted in Figures 5.3, 5.7, 5.11 and 5.15 are just meant to give a simple picture of the components and are not as accurate as the more realistic computations of Cromer et al. [CR 68]. On the basis of these estimates it is noted that the L-shell electrons contribute the major part of the amplitude in the region $2.5 < x < 6.0\ \mathring{A}^{-1}$ and that the K-shell electrons are important for $x > 7.0\ \mathring{A}^{-1}$. Larger momentum transfers involve K-electrons primarily. The form-factor approximation implies that the scattering amplitude depends mainly on x

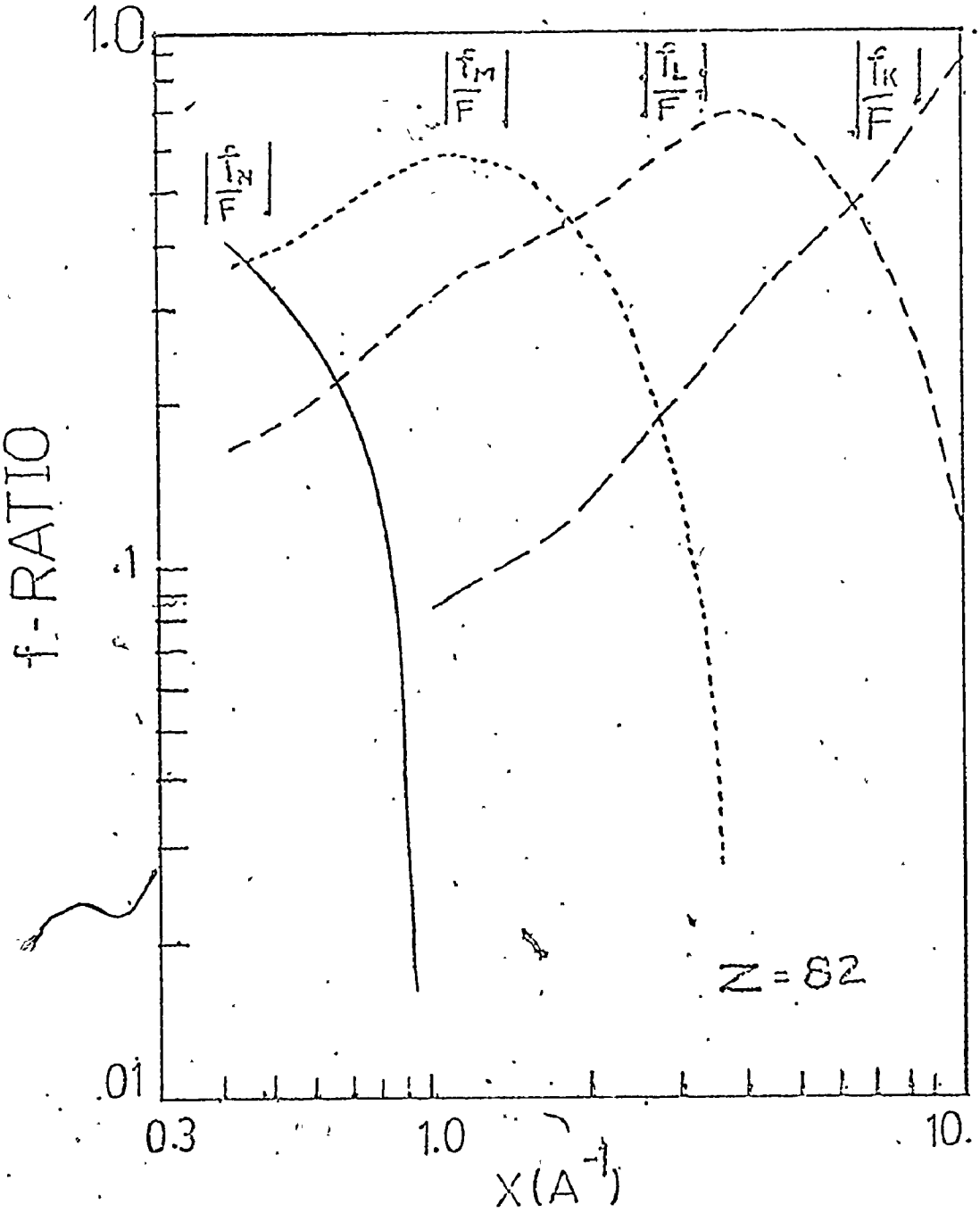

Fig. 5.3 The f-ratio curves for lead

and not directly on E. This is true to a great extent as exhibited by the plot of coherent scattering cross-sections against the momentum transfer x. To closely examine this point, the weighted mean ratio $\bar{R}_E$ for all the data points per energy was computed and drawn in Figure 5.4. It is observed (cf. Table 5.1a) that for the 244.7 and 344.3-keV lines the form-factor theory agrees with the experiment very well and for higher energies the experimental values are lower by about 15%. The approximate correction to the form-factor approximation suggested by Brown et al. [BR 57] is energy-dependent. This correction takes into account the electron-binding in the intermediate states of the atomic system. These two low energy lines (244.7 and 344.3-keV) span a region of x between 0.4 and 2.4 Å^{-1}. In this region there are data points due to higher energies and one may consider the weighted mean ratio for this region of x. It is noted that the weighted mean ratios for 244.7 and 344.3-keV lines are considerably higher than a similar ratio for x ranging from 0.4 to 2.4 Å^{-1}. This difference indicates that for the same range of x, the form-factor approximation describes the scattering due to low energy gamma rays more accurately

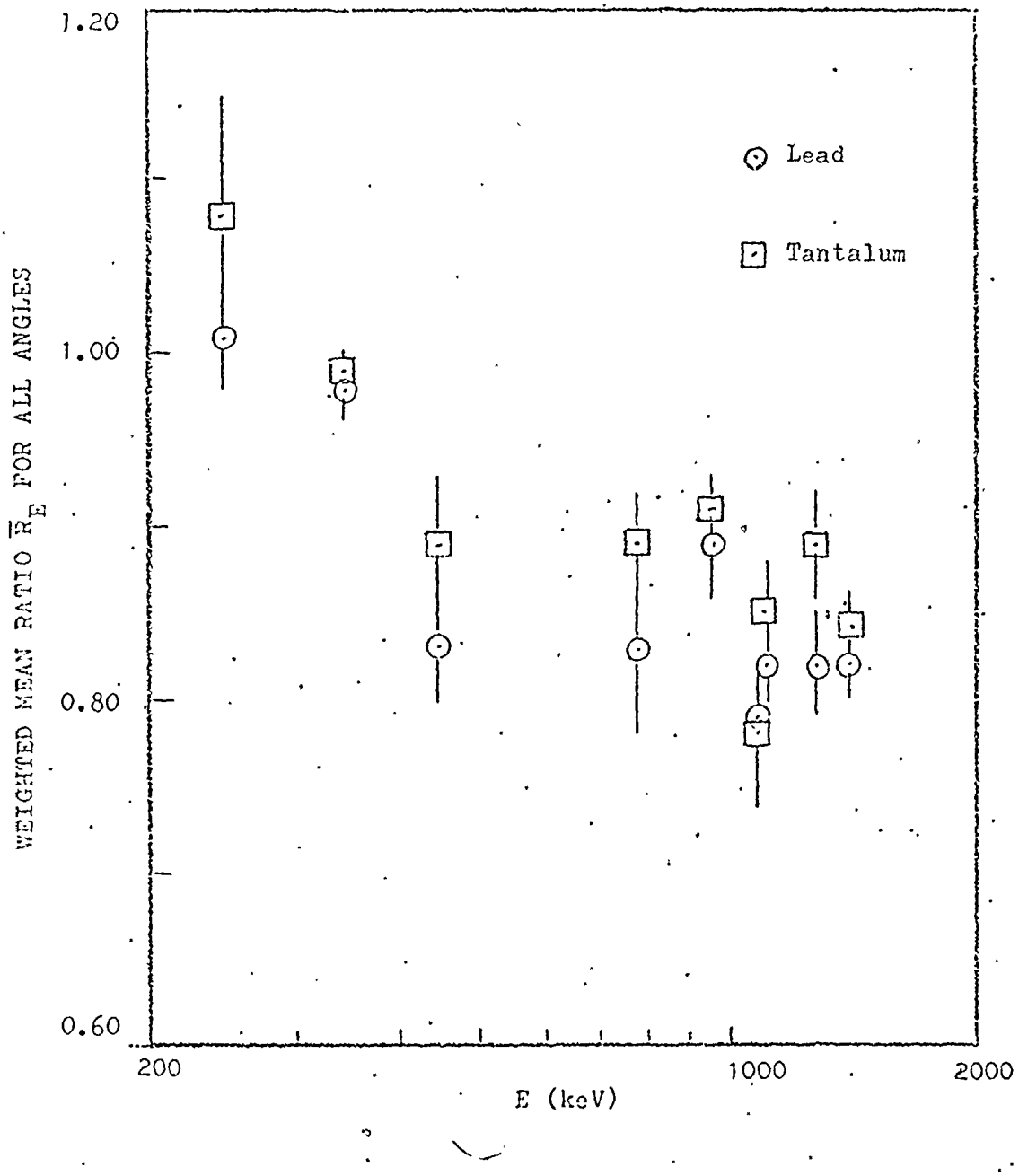

Fig. 5.4 Variation of the Weighted Mean Ratio $\bar{R}_E$ for the angular distribution with energy E in lead and tantalum

than the cases involving high incident energies. For $x > 2.5$ $\mathring{A}^{-1}$ or for incident energies 443.9 keV and above, the electron binding in the intermediate states could be a source of discrepancy. The form-factor in this region involves L and K-shell electron contributions for the most part. The correction to the L-shell form-factor could be $\sim -8\%$ (reading off Figure 4, reference Sc 73) and for the K-electron form-factor it could be as high as -30%. In the region of x above 7.0 $\mathring{A}^{-1}$ the K-electron contribution dominates the form-factor amplitude and in this region the weighted mean ratio is 0.94 ± 0.04. This value leads to the inference that the correction required to the K-shell form-factor is far less than the prediction. In fact in this region the experimental values are not far from the theory as the weighted mean ratio indicates. But in the region $3.5 < x < 6.3$, the weighted mean ratio is 0.78 ± 0.1 indicating an overall discrepancy of 22% in the cross-section. This may point to a correction of -11% to the form-factor which is not inconsistent with the estimate for L-shell contribution [SC 73]. The low values of the ratio R_i of experimental to the form-factor-based cross-sections [HU 75] in this region x may be noted from

the plot of R vs. x in Figure 5.2. It is to be mentioned that the coherent components in this region were, in almost all cases, well resolved from the incoherent peaks and so the possibility of the introduction of any uncertainty due to a lack of proper stripping of the incoherent component is negligible.

(d) Comparison with the theories and experiments for tantalum.

Both lead and tantalum are high Z materials with tightly bound K- and L- shell electrons. For example, the K- electron binding energy in lead is 88-keV and for tantalum it is 67.4-keV (cf. Table 5.7). So one may expect the shape of the f-ratio and form-factor curves for lead and tantalum to be similar in the momentum transfer range of $0.4 < x < 10.0$. In fact this pattern is exhibited by the f-ratio vs. x plots for tantalum (cf. Fig. 5.7) and the weighted mean ratios $\bar{R}_E$ for different energies in tantalum. As in the case of lead, the scattering of the 244.7 and 344.4-keV gamma rays in tantalum yields cross-sections as predicted by the form-factor calculations [HU 75]. For higher incident energies the experimental coherent scattering cross-sections are lower than the predictions, (Table 5.1a).

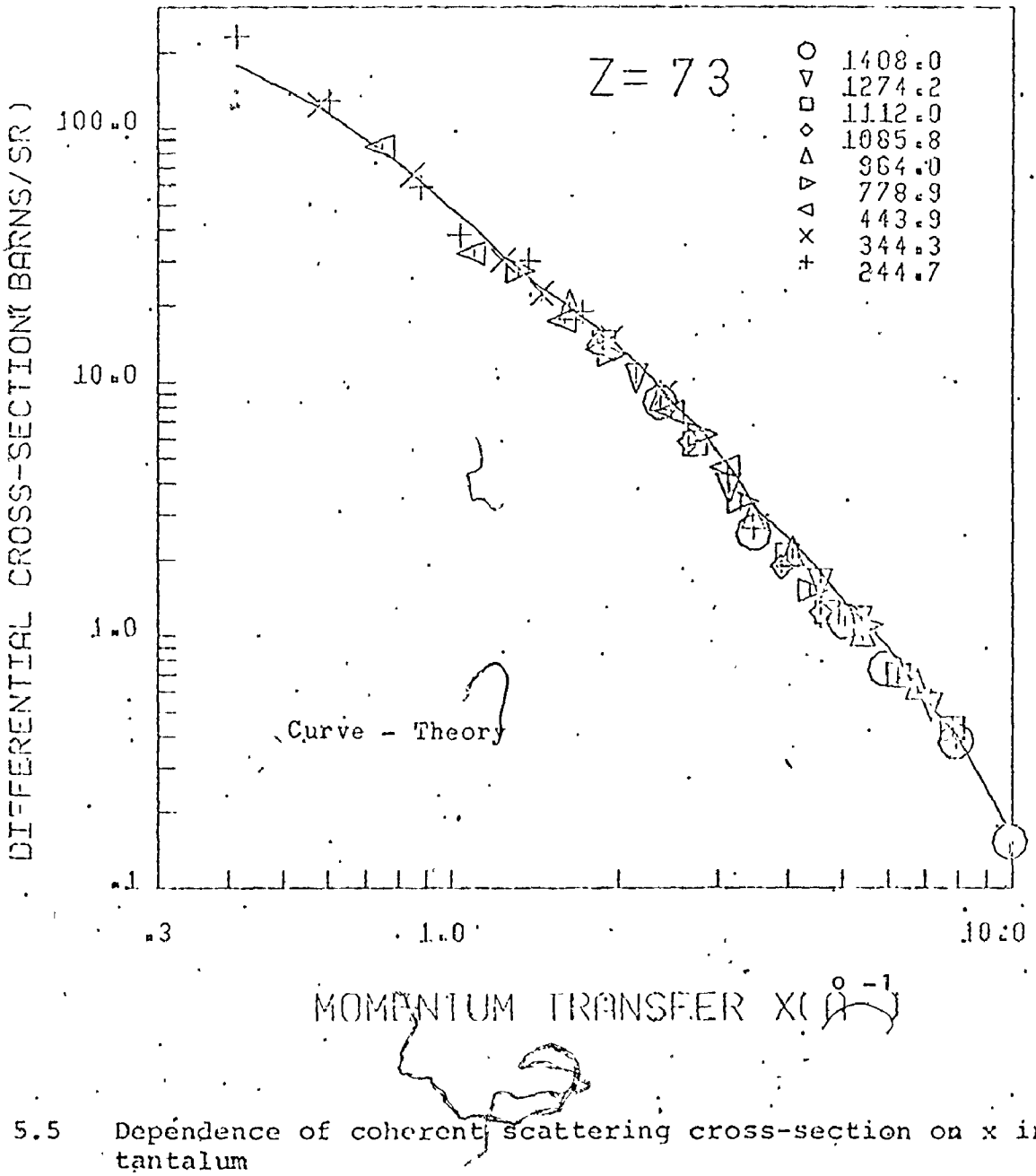

Fig. 5.5 Dependence of coherent scattering cross-section on x in tantalum

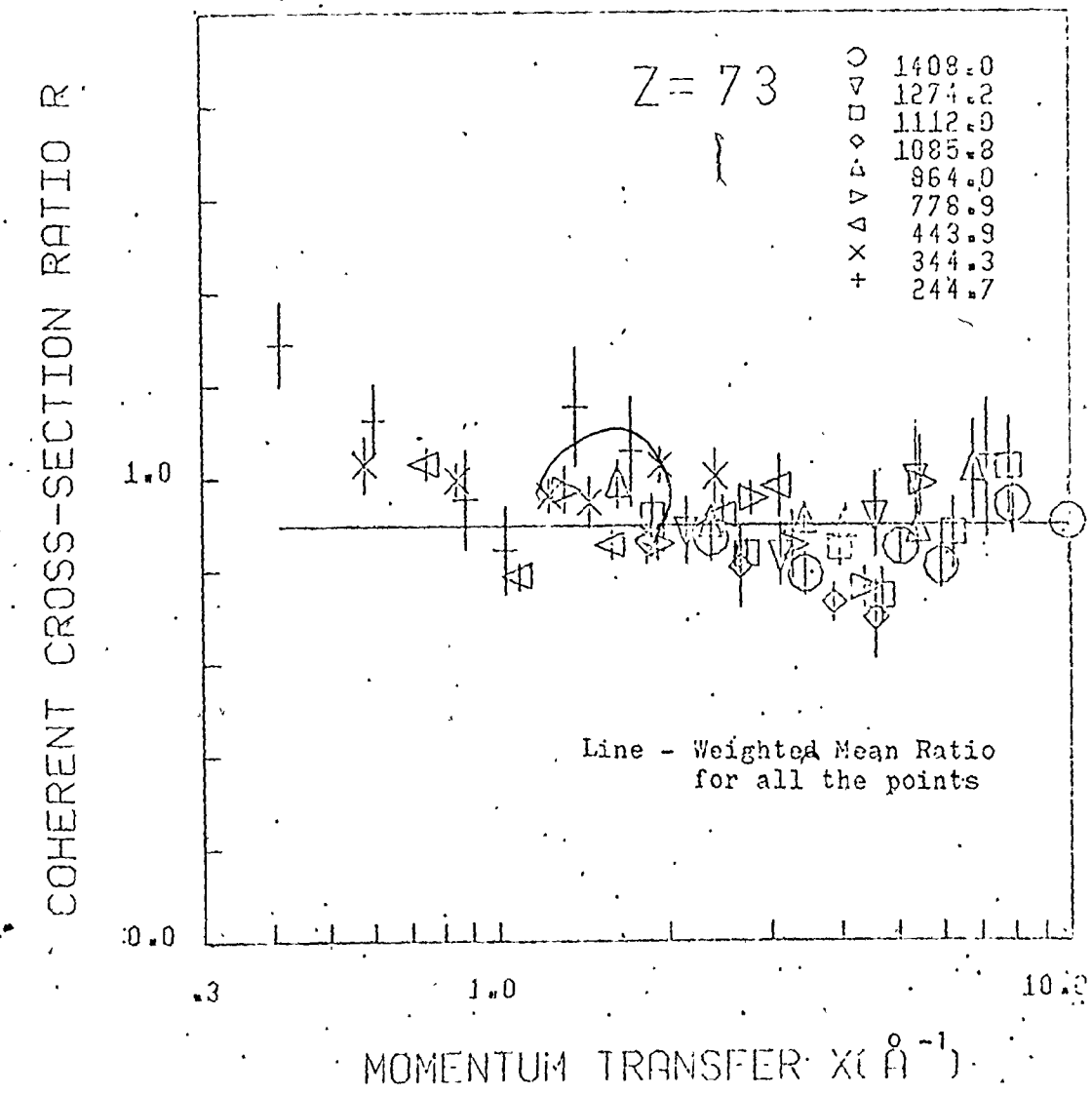

Fig. 5.6 Variation of coherent scattering cross-section ratio with x in tantalum

Bel'skii and Starodubtsev [BE 60] observed an anomalously high scattering cross-section for Co^{60} gamma rays in tantalum and suggested the possibility of Bragg diffraction. Except for the 244.7-keV line at 2.4^{o} there seems to be no such effect in the present data. From the crystal diffraction data [PDF 74] the possible strong diffraction lines and angles for this case were deduced and presented in Figure 5.8. With a d-spacing value of 0.8835Å^{-1} for a [321] reflection the scattering angle would be 2.15^{o}. With a relatively large angular resolution $\sim 1.5^{o}$, it is possible that there is some contribution for this datum. Since it is not possible to evaluate a reasonably accurate weighting of this infinitesimal angular interval this datum, i.e. the cross-section at 2.4^{o} for 244.7-keV is not useful. The weighted mean ratio of all the data for the 244.7-keV line is 1.08 ± .07 and for the 344.3-keV line, the corresponding value is 0.99 ± .01. For all the higher energies the agreement with the theory is poorer, yielding an over-all weighted mean ratio for all data equal to 0.90 ± .01. It is interesting to note from Table 5.1a and Figure 5.4 that the weighted mean ratio for all data for each incident energy in tantalum $\bar{R}_{E,Ta}$ is

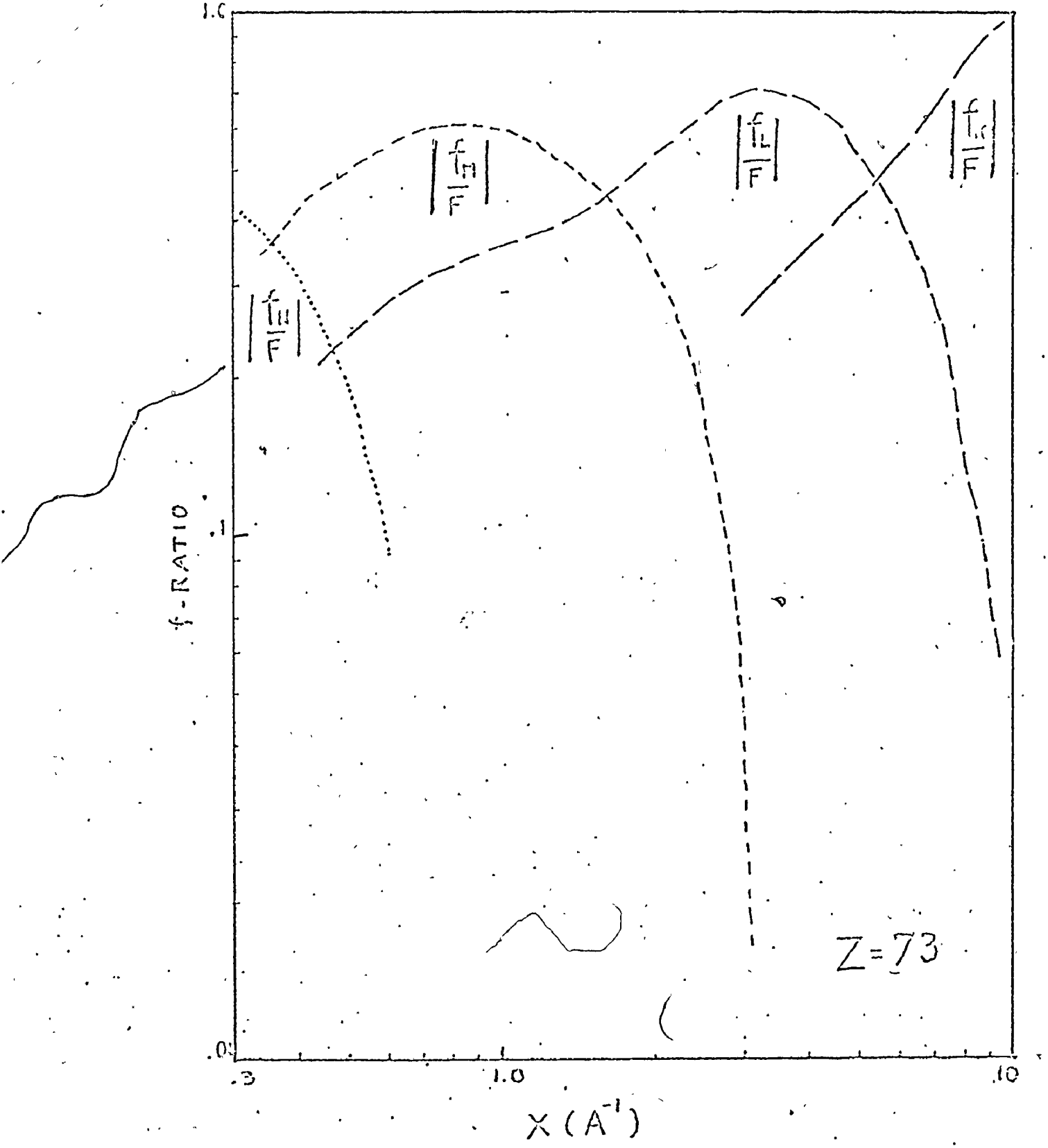

Fig. 5.7 The f-ratio curves for tantalum

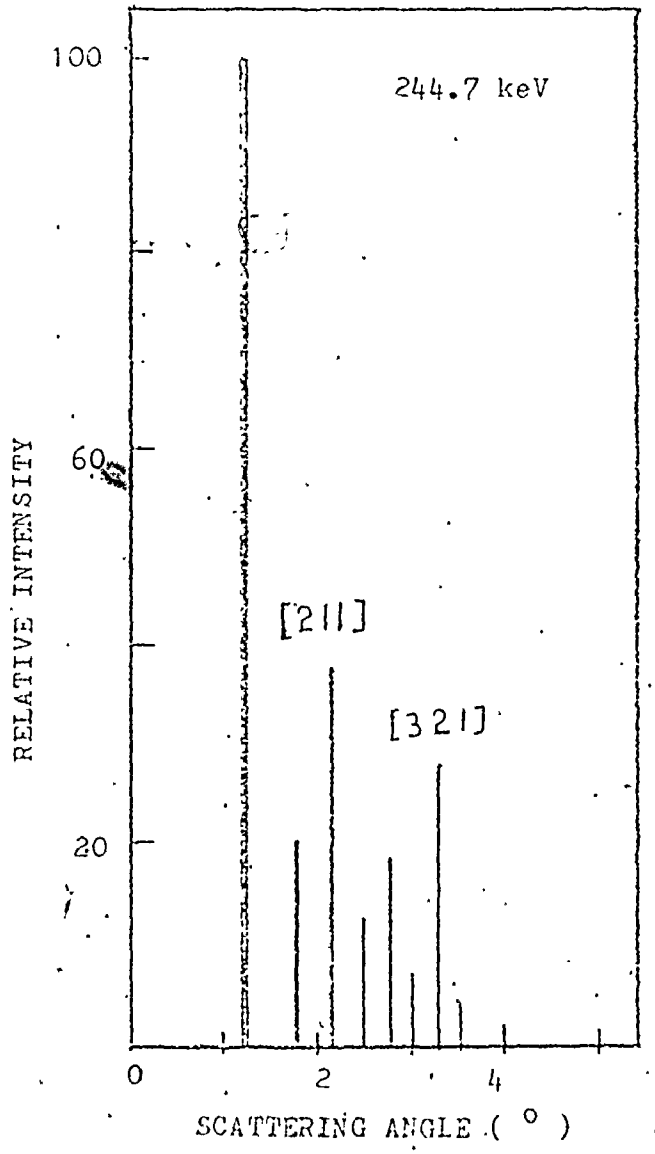

Fig. 5.8 Bragg diffraction intensities for scattering of 244.7-keV gamma rays by tantalum

relatively higher than $\bar{R}_{E,Pb}$. Thus, in general, if any correction to the (L-shell) form-factor amplitude is to be applied, the required magnitude will be less for tantalum than for lead.

When the measurements of Hauser et al. [HA 66] is considered for comparison in the range of x between 0.2 and 2.0 $\mathring{A}^{-1}$, the relatively large uncertainties do not allow their data to decide between the present values or the theory.

(e) Comparison with the theories and experiments for cadmium.

An inspection of the f-ratio and the differential cross-section curves in Figures 5.9 and 5.11, indicate that the features for cadmium are quite different from those of lead or tantalum. The important contributions to the form-factor scattering amplitude for cadmium arise from the K-, L- and M-shell electrons in the momentum transfer range of interest. The regions of their major contribution are wide and the cross-sections curve exhibits broad bumps. The experimental curve for cross-sections seems to follow the predicted shape for x up to 5.5. For x > 5.5 the experimental cross-sections have large deviations from the theory, the weighted mean ratio for all data in this

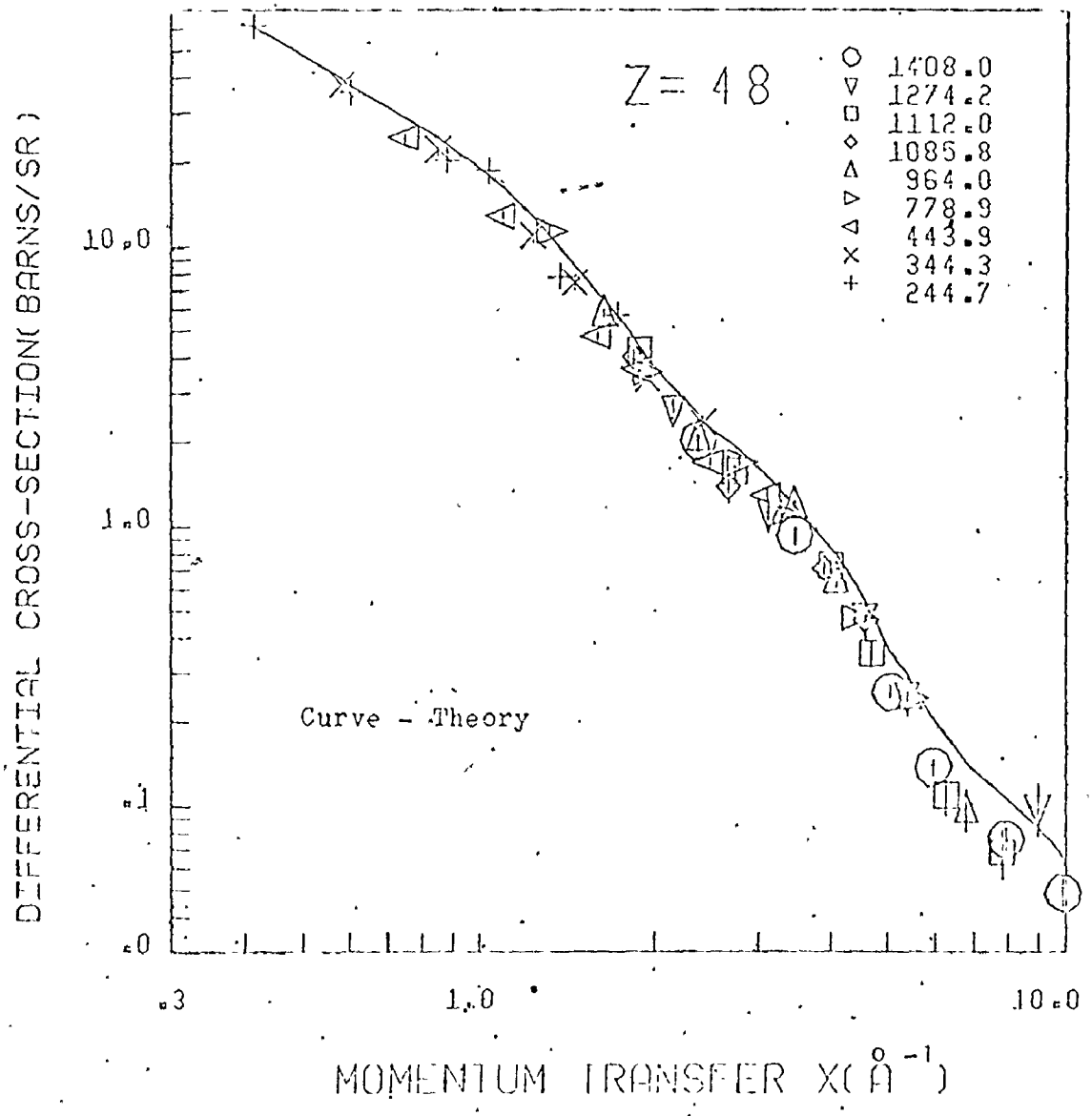

Fig. 5.9 Dependence of coherent scattering cross-section on x in cadmium

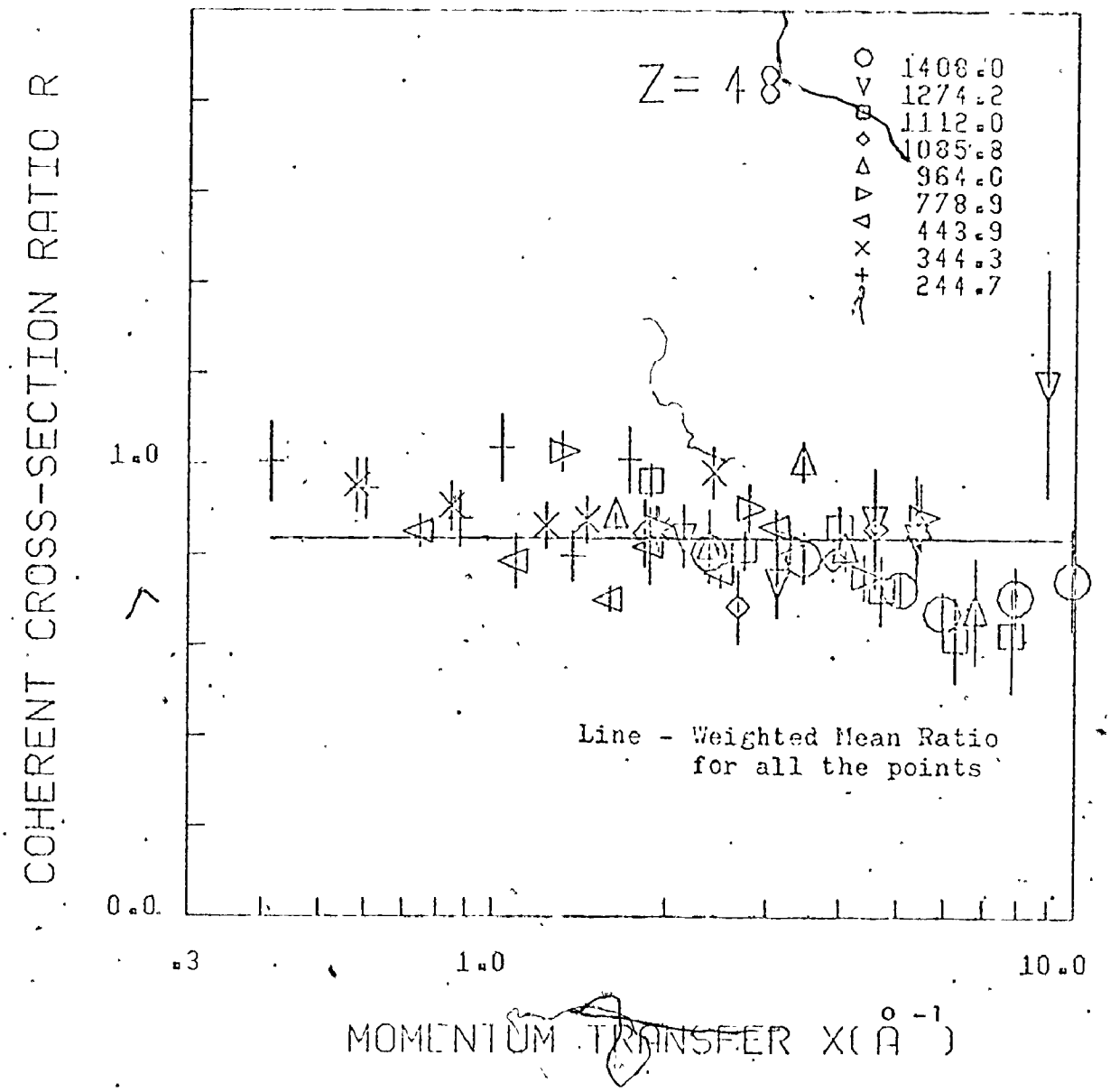

Fig. 5.10 Variation of coherent scattering cross-section ratio with x in cadmium

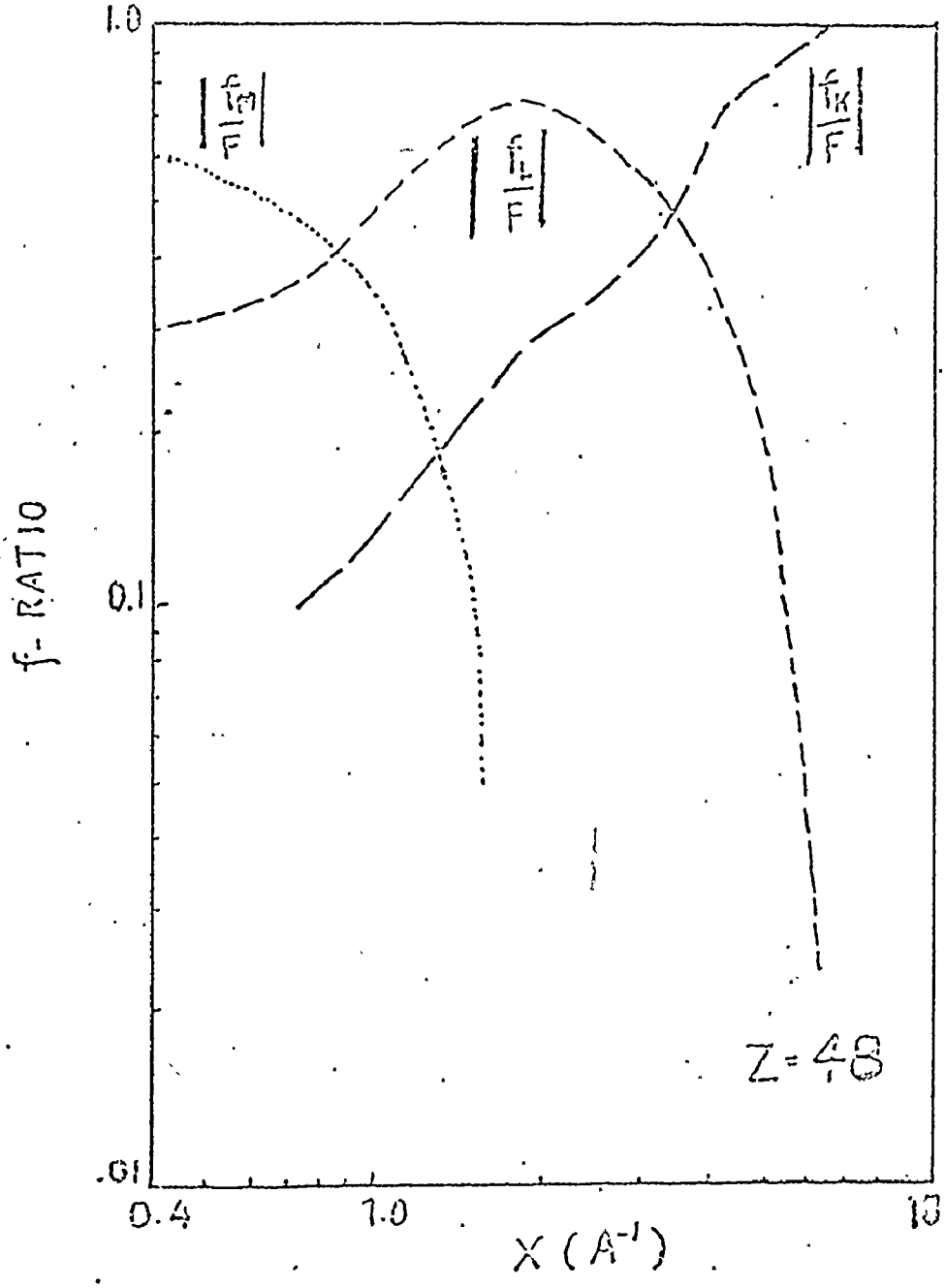

Fig. 5.11 The f-ratio curves for cadmium

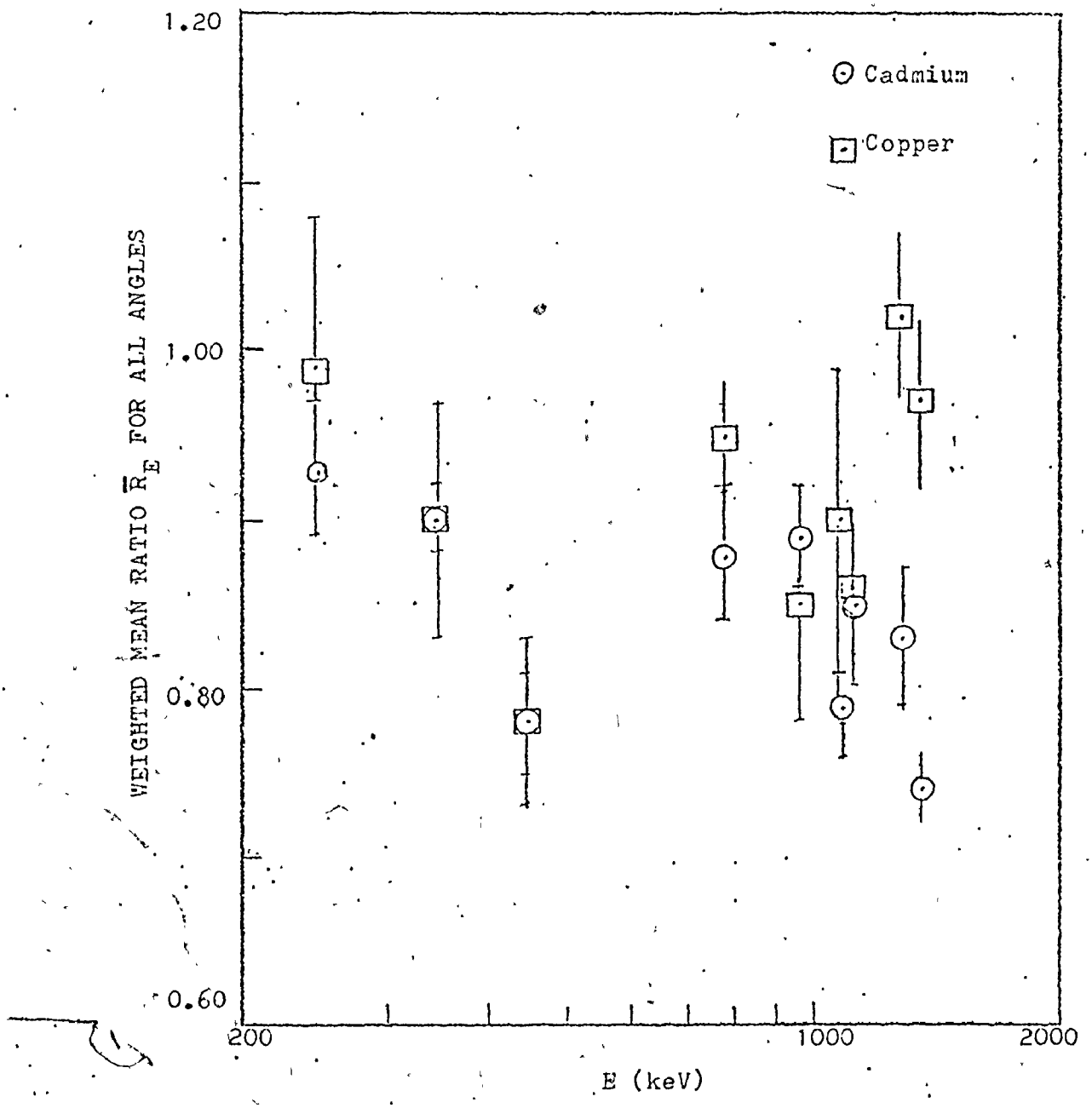

Fig. 5.12 Variation of $\bar{R}_E$ with E in cadmium and copper

region being 0.68 ± .03. This suggests that the K-shell form-factor requires a correction ∿ 16%. The agreement with the theory is better for x < 1.25 with the weighted mean ratio equal to 0.89 ± .02 while in the intermediate region of x, the mean ratio drops to 0.84 ± 0.02. Thus the general feature is that the deviation from the theory increases with the momentum transfer (also cf. Fig. 5.10). Very few previous measurements are available in the literature for comparison in this case.

(f) Comparison with the theories and experiments for copper.

Copper and cadmium bear considerable similarities in the f-ratio and cross-section curves (cf. Figures 5.15 and 5.13) but the experimental cross-sections for copper provide some interesting features. For momentum transfers greater than 1.2 $\mathring{A}^{-1}$, the data-points tend to follow the theoretical shape very well though the weighted mean ratio in this region is only 0.88 ± .03. But for x between 0.7 and 1.2 $\mathring{A}^{-1}$ the experimental cross-sections show a marked deviation. In this region of x, the L-shell scattering amplitudeis the prominent component while K- and M-shell contributions are important in the given order as shown in Figure 5.15. Then it is possible that the scattering

TABLE 5.6

Comparison of the experimental coherent scattering cross-sections for copper

Momentum transfer x in $\AA^{-1}$	$\frac{d\sigma}{d\Omega}$ in b/Sr from Nath and Ghose [NA 64]	$\frac{d\sigma}{d\Omega}$ in b/Sr present values for closest x
0.74	6.8 ± .8	5.9 ± .2
1.55	1.25 ± .3	1.73 ± .07
1.87	0.85 ± .15	1.39 ± .08
2.1	0.6 ± .15	1.01 ± .08
2.49	0.3 ±0.1	0.45 ± .02

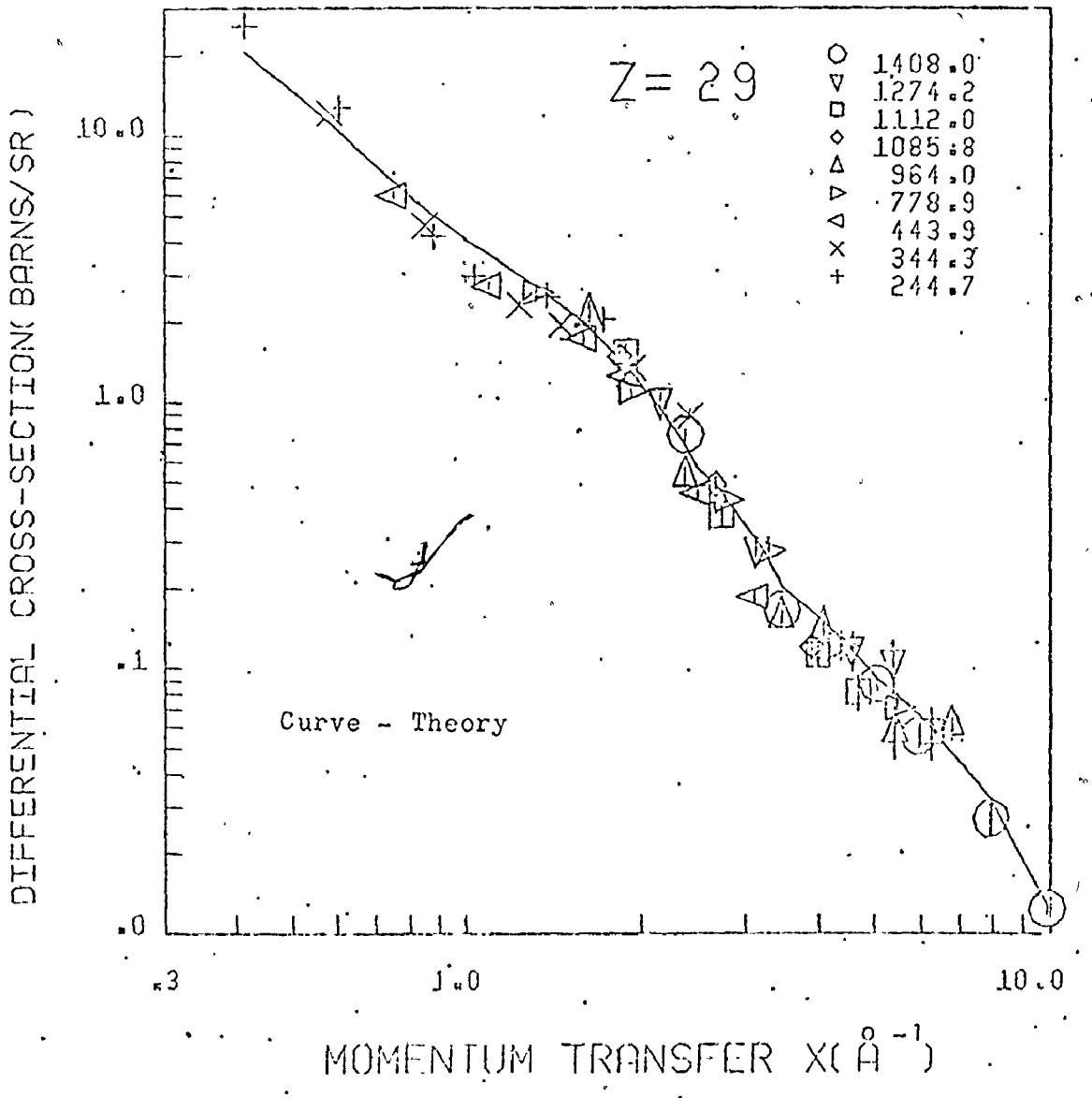

Fig. 5.13 Dependence of coherent scattering cross-section on x in copper

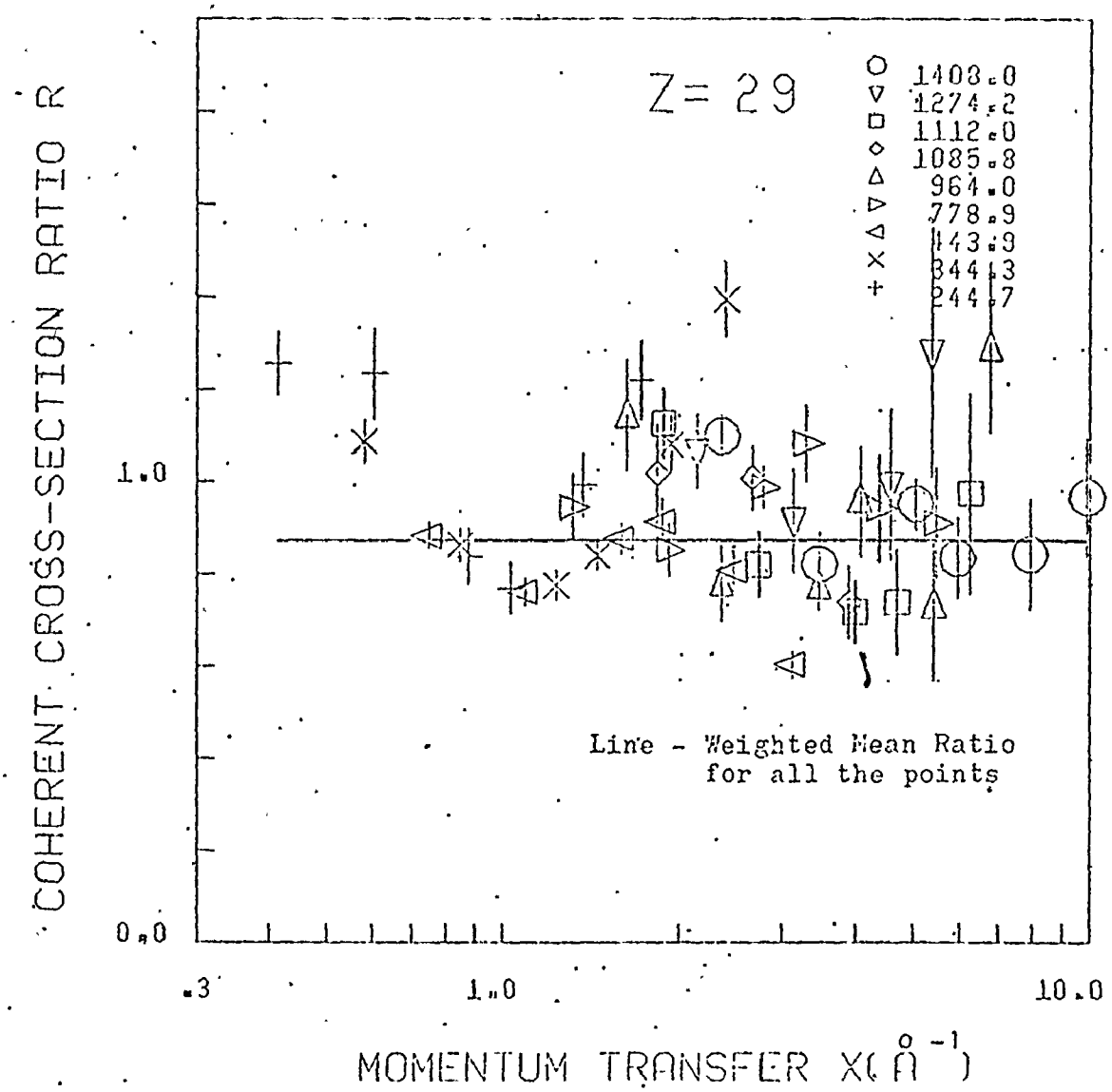

Fig. 5.14 Variation of coherent cross-section ratio with x in copper

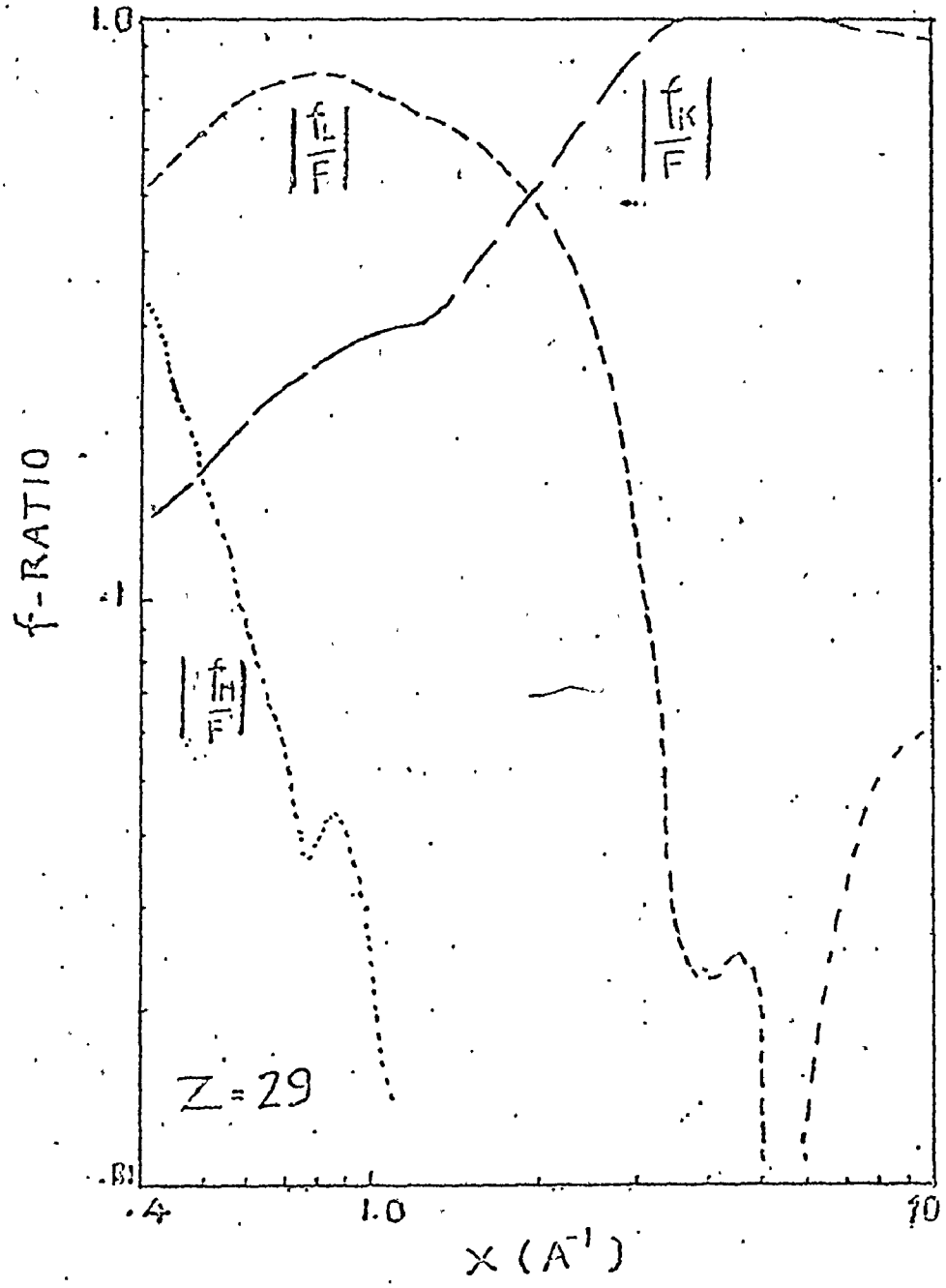

Fig. 5.15 The f-ratio curves for copper

amplitude in this case is quite sensitive to the M-shell contribution also. For the incident energies between 443.9- and 1112.0-keV the weighted mean ratios are about the same for cadmium and copper as in Figure 5.12 and Table 5.1a. But the weighted mean ratios for 1274.2- and 1408.0-keV lines are close to 1.00 for copper while for cadmium the data for these two incident energies yield considerably low weighted mean ratios. Thus copper and cadmium differ substantially as far as the data for these two lines are concerned.

Experimental coherent scattering cross-sections of Nath and Ghose are presented against the present values for copper in Table 5.6. For the coherent component the experimental count-rates for the copper scatterer were low and hence in general, the uncertainties would be relatively large. They observed that their values were lower than the form-factor based cross-sections. Their measurement agrees with the present value for $x \simeq 0.74$ and for higher x their cross-sections are significantly lower. It is, however, to be remembered that they measured the scattering cross-sections with unresolved incoherent components and deduced the coherent part. In this range of x, the incoherent scattering cross-sections are $\sim$ 2 barns and hence they had to extract a small component. This could be a possible cause for their low values and large uncertainties.

It may be recalled that the theoretical values used above for comparison with the experiment are based on non-relativistic wave-functions. The relativistic correction to the form-factor amplitudes becomes important for momentum transfers in the range of $(Z\alpha)^{-1}$ in (mc) units. This corresponds to a value of $x = 34.4\text{Å}^{-1}$ in lead and $x = 97.3\text{Å}^{-1}$ for copper. Levinger [LE 52] showed that for the scattering of gamma rays by K-electrons in tin the relativistic effect increases the form-factor amplitude by about 25% for a momentum transfer of 61.8Å^{-1}. Also the computations of Cromer-Waber [Table 7, HU 75] suggest an increase to the form-factor by about 4.7% for $x = 2.0\text{Å}^{-1}$ in lead. So any inclusion of the relativistic correction to the form-factor would increase the deviation from the experiment and any future computation will have to accommodate this effect too.

2. Incoherent scattering cross-sections - comparison with the theory and experiments and discussion

Recalling from chapter 2, the incoherent scattering function S(x,Z) modifies the pure Compton scattering cross-sections to take into account the effect of the binding energies of the atomic electrons where the energy transferred by the gamma ray is of the order of the binding energies. The incoherent scattering function is a function of momentum transfer x and the momentum transfers involved in this investigation fall in the range where the incoherent scattering function varies from 0.0 to 1.0 depending upon x and the atomic number Z of the scatterer. In the region of interest the previous experimental values have large uncertainties and provide a need for further measurements for any decisive comparison [HU 75, page 490]. Of particular interest in this context are the measurements of incoherent scattering, cross-sections by Anand et al. [AN 64] and Quivy [QU 66]. The measured incoherent scattering functions for lead [AN 64] were about 20% less than the theoretical values [CR 69, HU 75] for x between 5.0 and 8.0 Å^{-1}. Quivy's measurement showed that the experimental incoherent scattering functions were lower than (~10%) the predicted

values for $x \gtrsim 10.0$ $\mathring{A}^{-1}$. These investigations involved 280-keV [AN 64] and 662-keV [QU 66] gamma rays and large scattering angles. In the region of x of our interest these measurements present only a few data-points.

From the experimental incoherent scattering differential cross-sections the number of equivalent "free" electrons n_f were calculated using the relationship given by

$$n_f = \frac{\left(\frac{d\sigma}{d\Omega}(\theta)\right)_{EXPT}}{\left(\frac{d\sigma}{d\Omega}(\theta)\right)_{KLEIN\text{-}NISHINA}}$$

where the denominator is the differential cross-section per electron calculated on the basis of the Klein-Nishina formula.

The weighted mean values of n_f for different momentum regions were computed and presented in Table 5.8 for all the elements of interest. If the scattering were to follow the Klein-Nishina free electron scattering cross-sections the number of electrons would be equal to the atomic number Z of the atom. From Table 5.8, it is to be

TABLE 5.7

Atomic electron binding energies

X-ray levels	Spectroscopic notation for electrons	Number of electrons	Binding energies in keV					
			Lead	Tantalum	Cadmium	Copper	Aluminum	Carbon
K	1S1/2	2	88.0	67.4	26.7	8.98	1.56 }	0.284
LI	2S1/2	2	15.86	11.68	4.02	1.096	0.118}	
LII	2S1/2	2	15.20	11.14	3.727	0.951	0.073}	
LIII	2P3/2	4	13.04	9.88	3.538	0.931		
MI	3S1/2	2	3.851	2.708	0.770	0.120		
MII	3P1/2	2	3.554	2.469	0.65;			
MIII	3P3/2	4	3.066	2.194	0.617			
MIV	3D3/2	4	2.586	1.793	0.411			
MV	3D5/2	6	2.484	1.735	0.404			
NI	4S1/2	2	0.894	0.566				
NII	4P1/2	2	0.764	0.465				
NIII	4P3/2	4	0.645	0.405				
NIV	4D3/2	4	0.435	0.241				
No. of electrons up to the marked shells			54	55	38	27	13	
Experimental n_f for $6.0<x<10.0$			58.5 ±1.4	56.4 ±1.3	37.8 ±0.5	25 ±0.4	12.8 ±0.2	

TABLE 5.8

Average number of equivalent free electrons $\bar{n}_f$ from experiment

Momentum transfer region in Å^{-1}	$\bar{n}_f$ lead	tantalum	cadmium	copper
1.3 - 2.4	45.1±3.7	49.2±4.6	26.6±1.4	20.5±0.7
2.6 - 4.7	51.0±0.8	52.3±0.8	34.3±0.8	24.0±0.4
5.0 - 9.9	58.5±1.4	56.4±1.3	37.8±0.5	25.0±0.4
Average for all regions	54.1±1.2	53.9±1.0	34.4±0.8	23.8±0.3

noted that lead, tantalum, cadmium and copper have the number of weighted mean free-electrons $\bar{n}_f$ less than their atomic numbers, conforming to the general expectation. Aluminum follows the pure Compton scattering process in this region. Also one may note a gradual increase in $\bar{n}_f$ with x for copper, cadmium, tantalum and lead. Comparing the electron binding energies (cf. Table 5.7) and the deduced n_f for maximum x in this work, it appears as though the electrons with binding energies less than about 2.0 keV participate fully in the incoherent scattering. In this region the energy transferred by the gamma ray is of the order of 60 keV. This observation is consistent with the data for all these elements. Perhaps, in a simple sense, this situation may be answering the question of how free are the electrons for a given energy transfer. Actual computation of the incoherent scattering cross-sections are more complicated and the comparison of the experimental data will be made with the calculations of Cromer [CR 69] tabulated by Hubbel et al. [HU 75].

The experimental scattering function is obtained by dividing experimental free electrons n_f by the atomic number of the scatterer. When the scattering is a pure

Compton process the incoherent scattering function is equal to unity. For the elements under study the experimental incoherent scattering functions are plotted against the momentum transfer x in Figures 5.16 - 5.19. The theoretical values are drawn as continuous curves. The incident energies are indicated by different symbols and the uncertainties by the vertical bars. For quantitative comparisons with the theory, the ratio of the experimental to theoretical incoherent scattering functions were computed. The weighted means of such ratios were obtained for the angular distribution of each gamma ray with energy from 1408.0 - to 778.9-keV. Similar weighted means of the ratios were taken for different momentum transfer regions also. The results are presented in Table 5.9. For lead and tantalum the weighted mean ratios for different momentum transfer regions are about the same within their uncertainties while it was noted that the mean free electrons were increasing with x. This indicates that on the average the trend for the variation of incoherent scattering function is similar between the theory and experiment, (cf. Figures 5.16, 5.17, 5.20 and 5.21). But, for cadmium and copper the mean ratios for x below 2.4 are less than those for larger

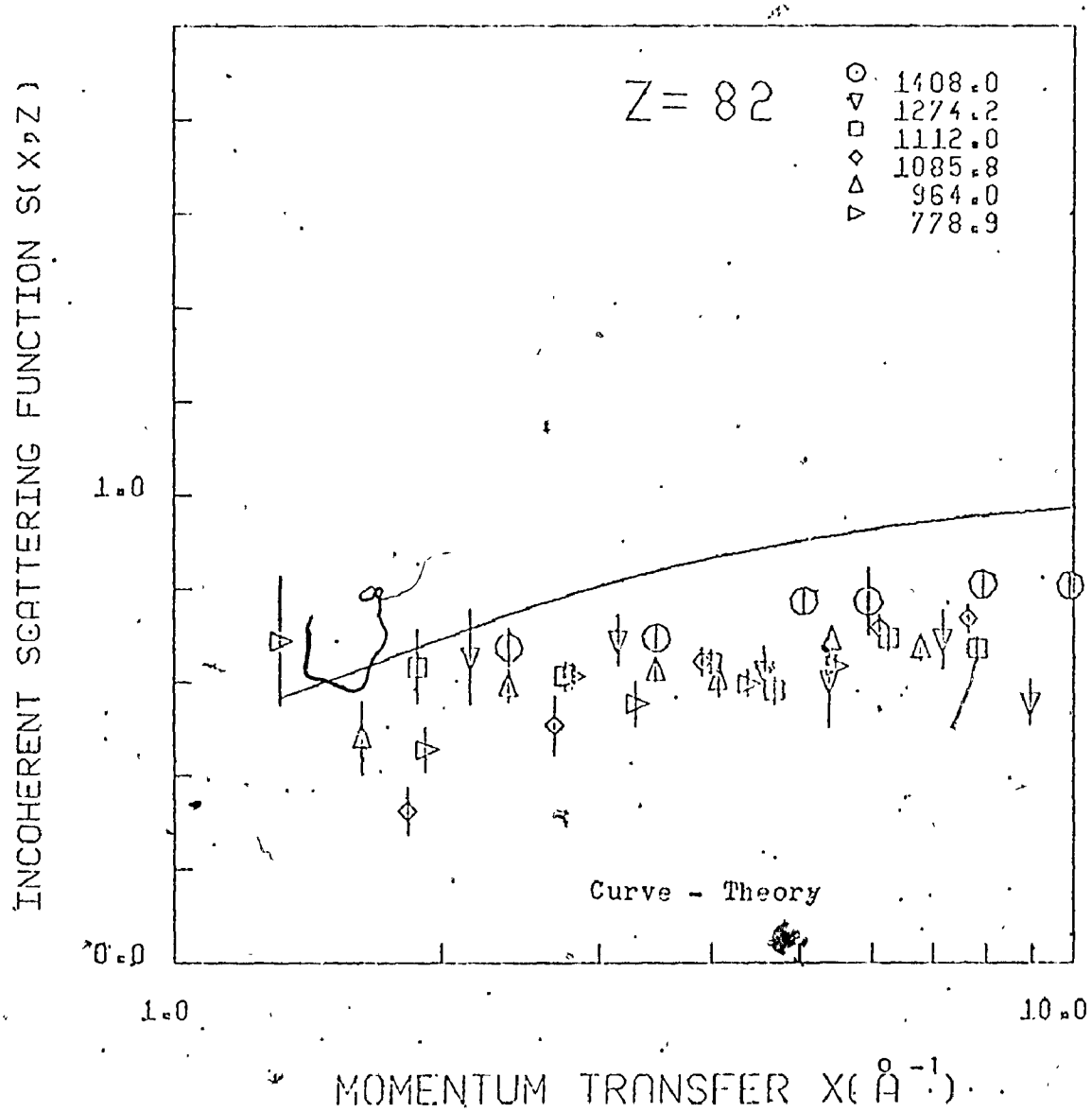

Fig. 5.16 Variation of incoherent scattering function S with x in lead

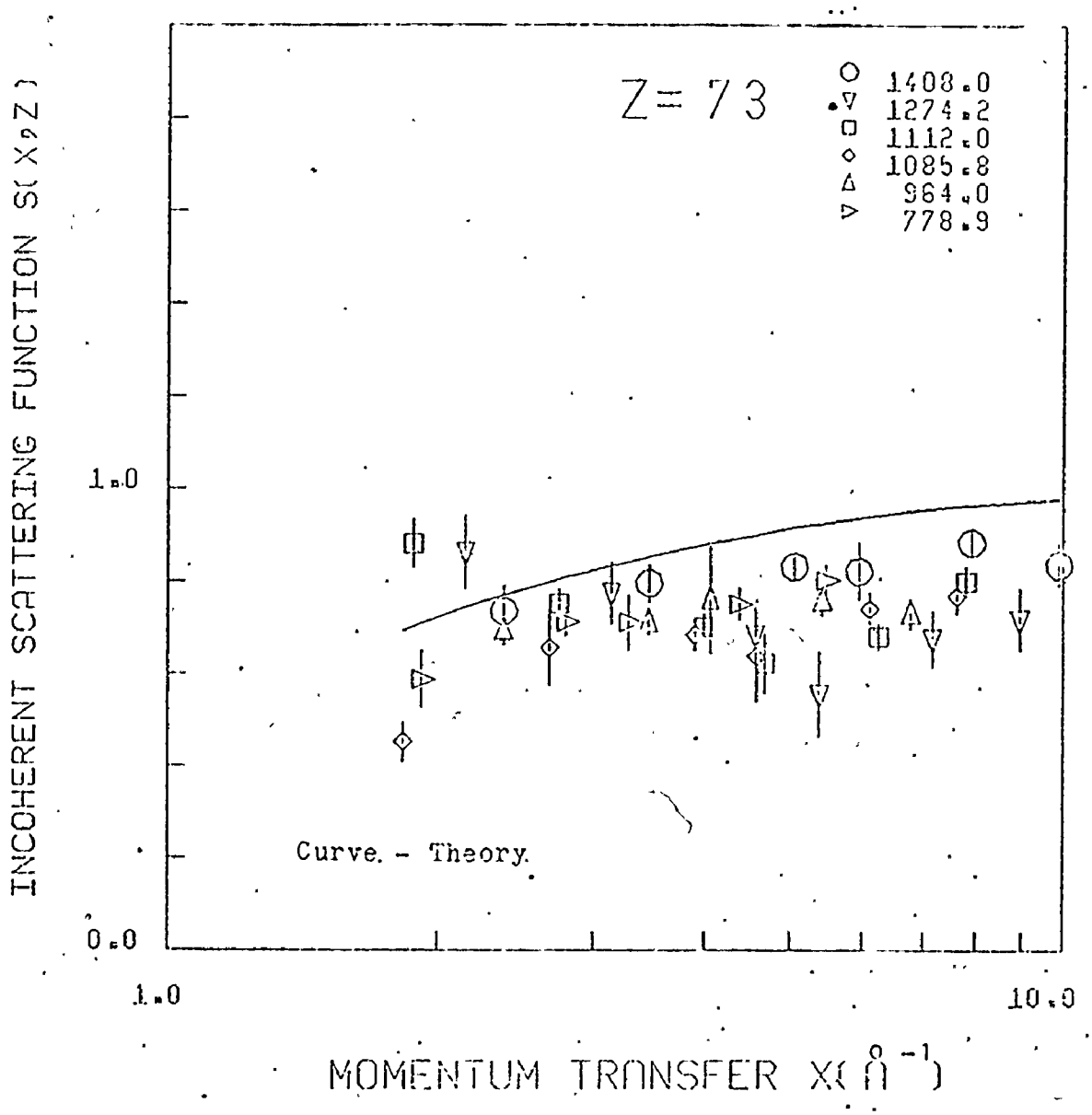

Fig. 5.17 Variation of S with x in tantalum

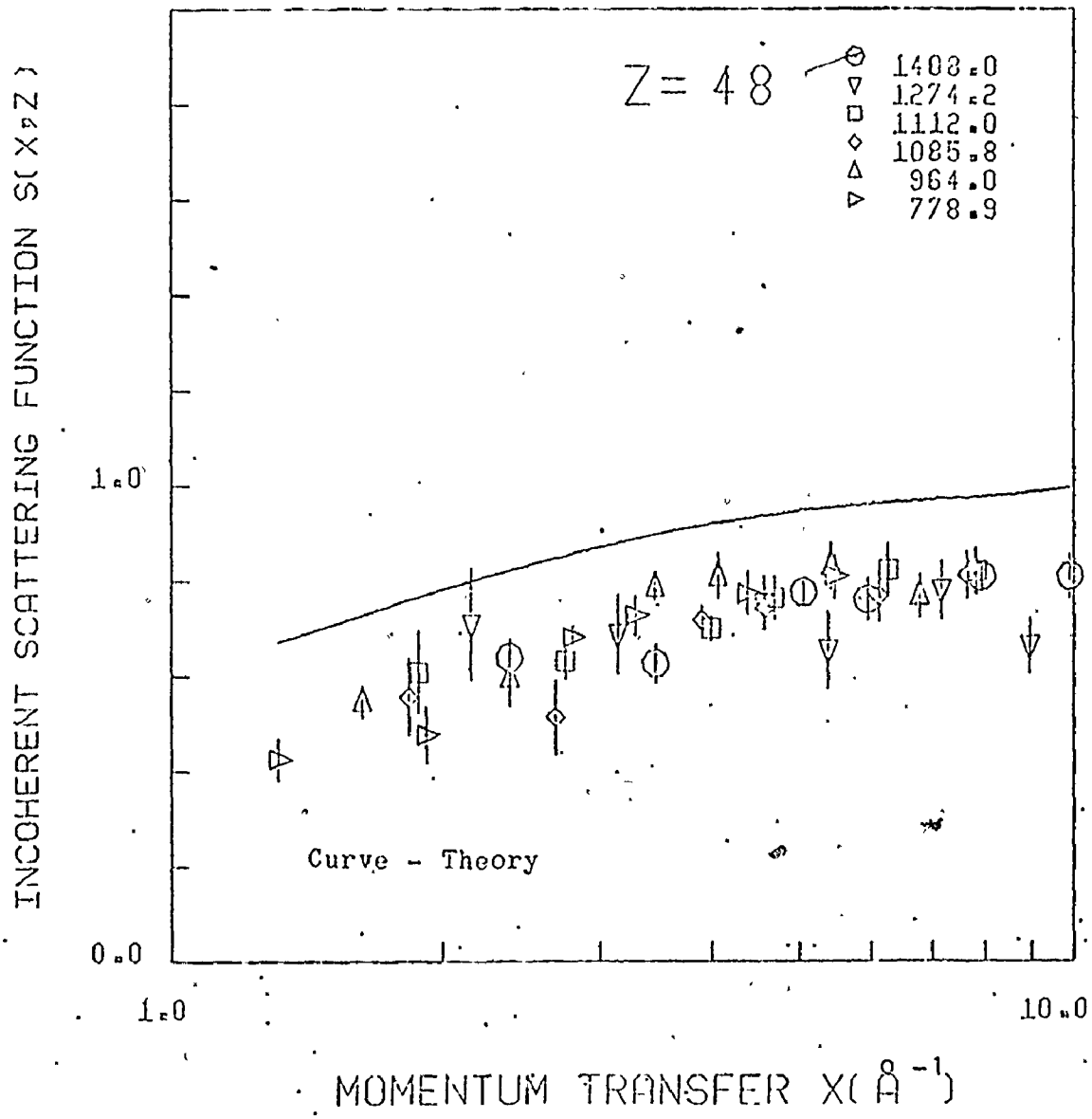

Fig. 5.18 Variation of S with x in cadmium

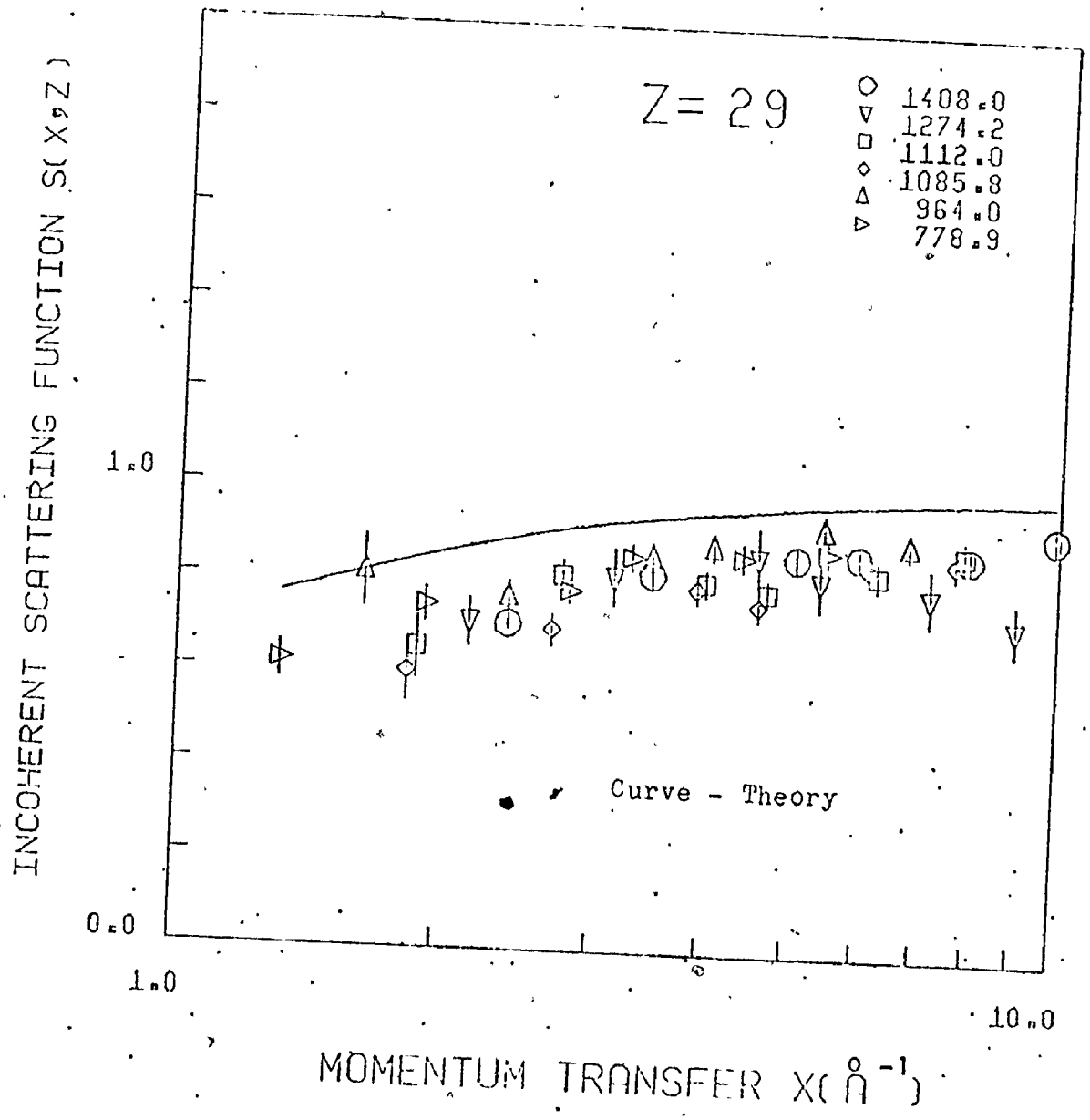

Fig. 5.19 Variation of S with x in copper

TABLE 5.9

Weighted Mean Ratios of Experiment to Theory-Incoherent Scattering

E.	$\bar{R}_{Pb}$	$\bar{R}_{Ta}$	$\bar{R}_{Cd}$	$\bar{R}_{Cu}$	$\bar{R}_{Al}$
1408.0	0.85±.01	0.91±.01	0.80±.02	0.88±.02	0.96±.02
1274.2	0.70±.05	0.79±.07	0.76±.03	0.82±.03	0.90±.03
1112.0	0.73±.02	0.82±.06	0.79±.02	0.85±.01	1.03±.03
1085.8	0.74±.03	0.77±.02	0.79±.02	0.82±.02	1.01±.03
964.0	0.74±.01	0.83±.02	0.83±.03	0.92±.01	1.01±.03
778.9	0.71±.02	0.86±.01	0.79±.03	0.88±.01	0.99±.05
					1.06±.04)
					1.00±.01) Total
					1.06±.05)
Average $\bar{R}$ for all points	0.75±.01	0.84±.02	0.80±.01	0.87±.01	1.00±.01

Average Ratio for different x-regions

x	$\bar{R}_{Pb}$	x	$\bar{R}_{Ta}$	x	$\bar{R}_{Cd}$
1.32-2.38	0.78±.05	1.83-2.38	0.92±.08	1.32-2.38	0.73±.02
2.67-4.69	0.74±.01	2.67-4.69	0.84±.02	2.67-4.69	0.80±.01
5.05-9.90	0.76±.02	5.05-9.9	0.82±.02	5.05-9.90	0.82±.01

x	$\bar{R}_{Cu}$	x	$\bar{R}$
1.32-2.38	0.83±.02	0.41-2.50	1.04±.02
2.67-5.94	0.87±.01	2.67-3.99	0.97±.03
6.11-9.9	0.87±.02	4.07-9.90	0.99±.02

momentum transfer regions, leading to the observation that the average shapes of the theorectical and experimental values differ considerably in this region, as depicted by the plots for the ratio of experimental to theoretical incoherent scattering functions against the momentum transfer through Figures 5.22 and 5.23.

Another interesting feature of the deviation between the theory and experiment is the atomic number dependence. The weighted mean ratios of the angular distribution for each gamma ray energy were plotted against the atomic number of the scatterer in Figures 5.26 - 5.28. From these graphs one may observe that the deviation increases with the atomic number and for all the energies the pattern of deviation appears to be very similar. So any factor explaining the discrepancy may have a strong Z-dependence.

Now the possible causes of the deviations between the theory and experiment may be considered. Recently there has been a series of publications on the effects of multiple scattering [TA 76]. The scattered photon, after one Compton scattering may undergo another Rayleigh or Compton scattering. If the second scattering were to add to the intensity

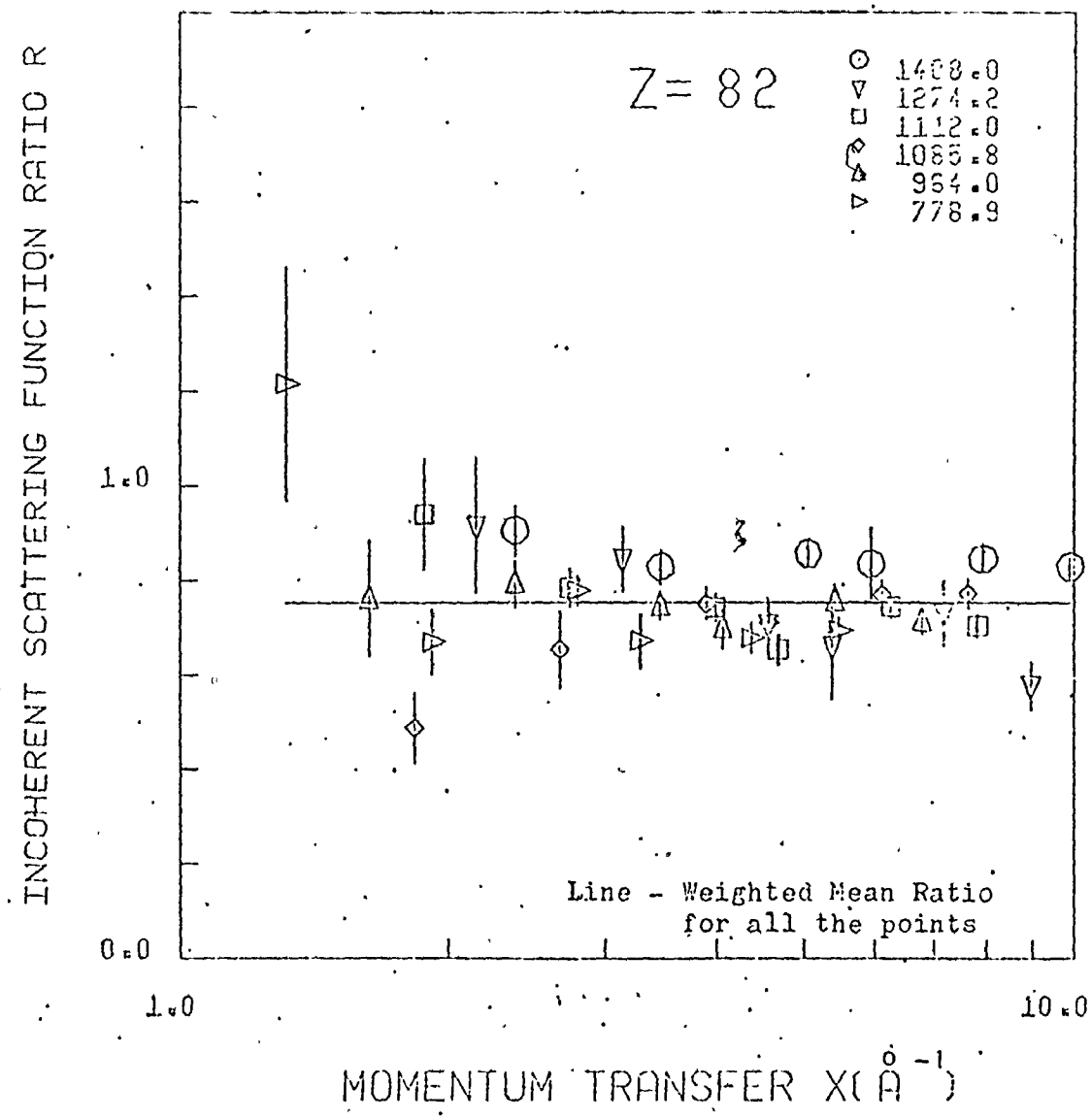

Fig. 5.20 Dependence of incoherent scattering cross-section ratio on x in lead

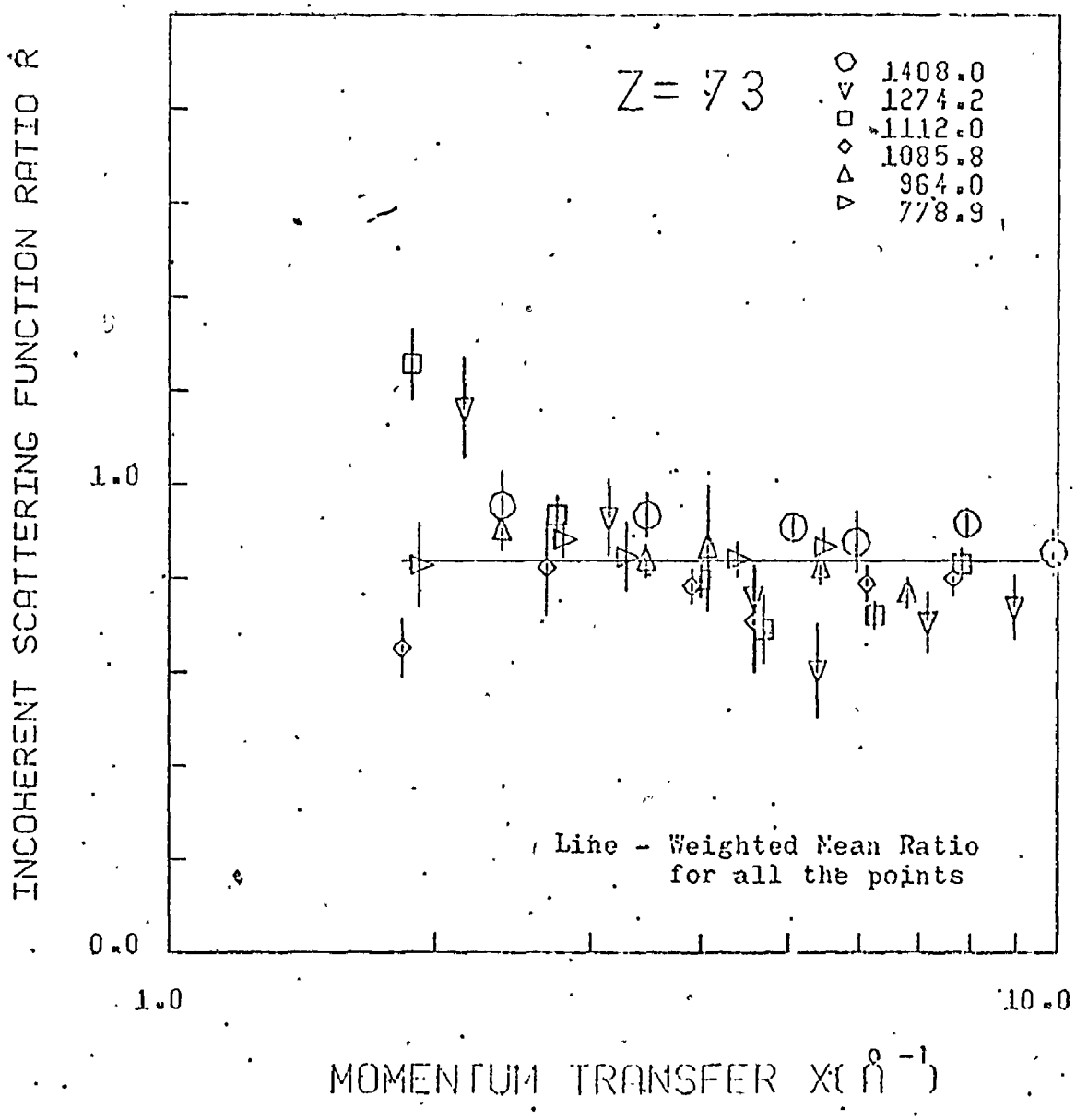

Fig. 5.21 Dependence of incoherent scattering cross-section ratio on x in tantalum

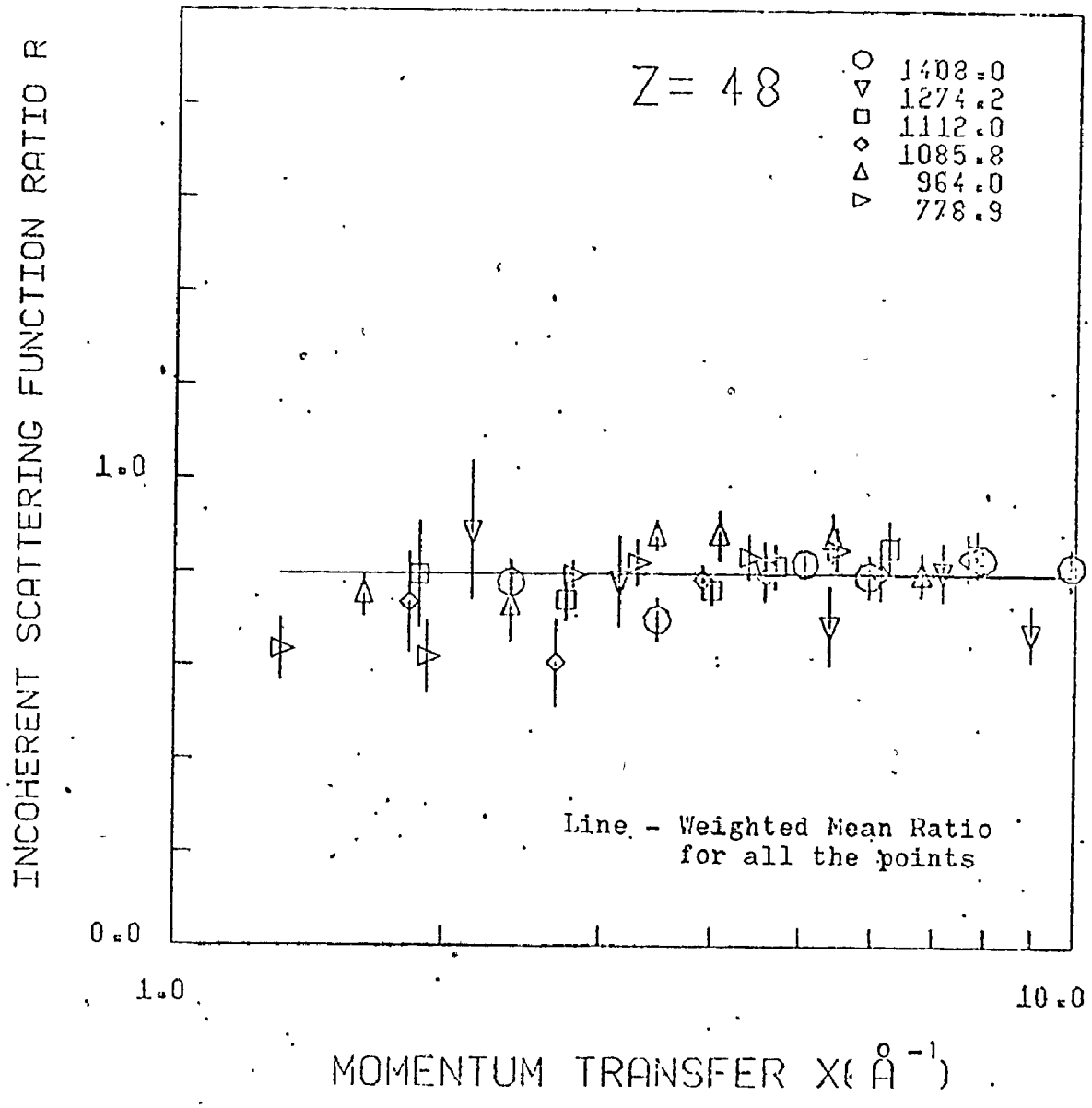

Fig. 5.22 Dependence of incoherent scattering cross-section ratio on x in cadmium

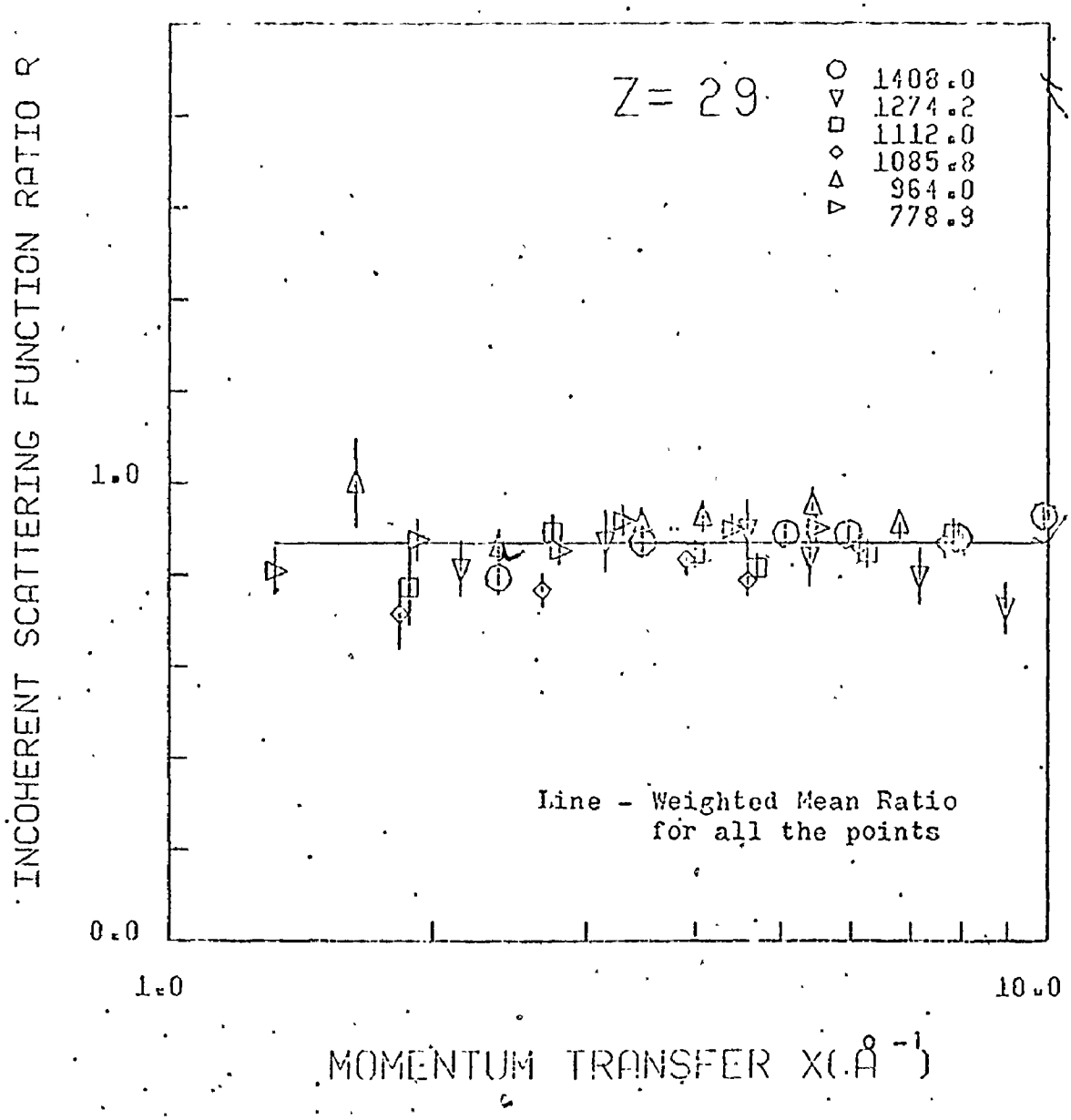

Fig. 5.23 Dependence of incoherent scattering cross-section ratio on x in copper

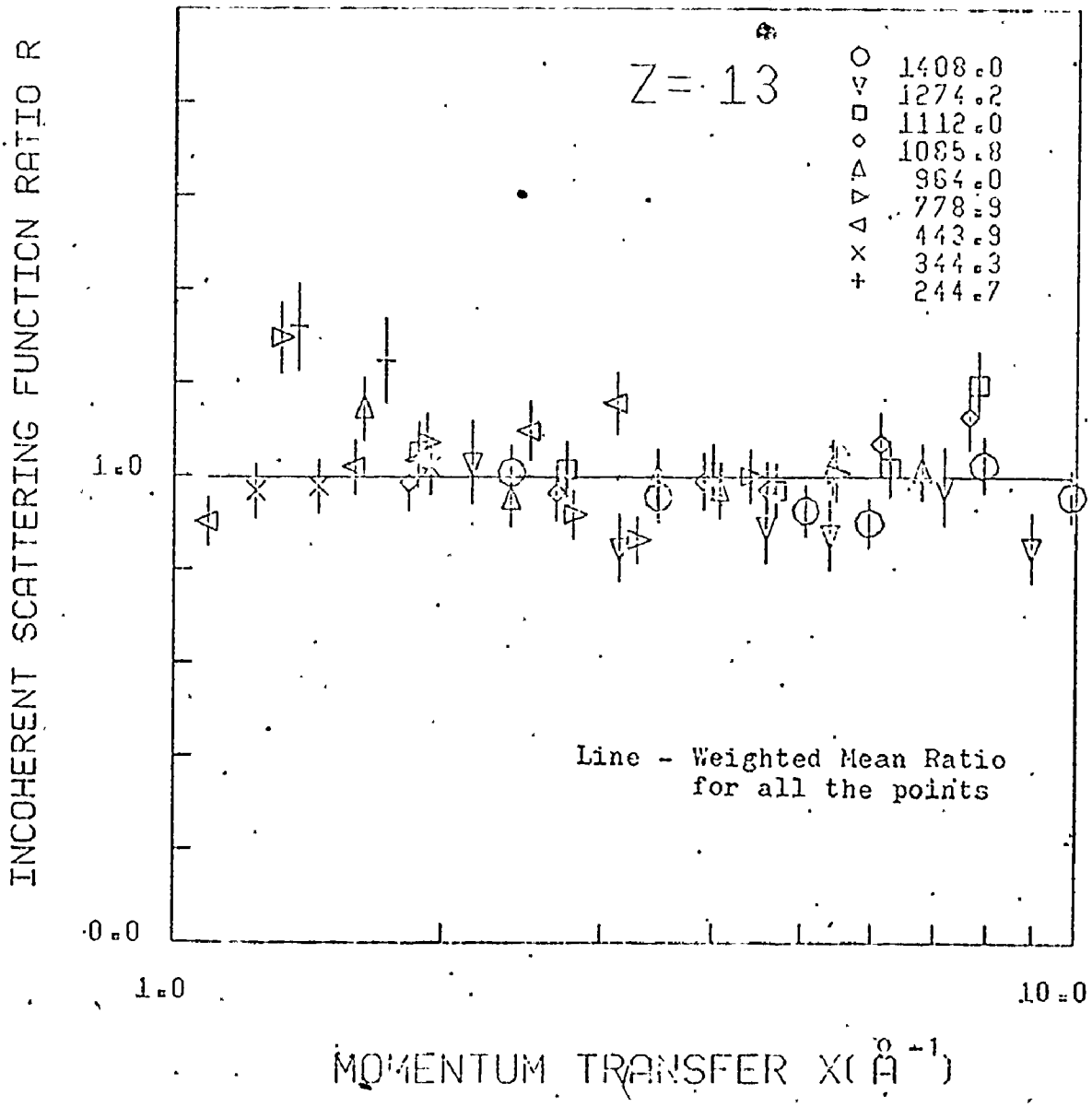

Fig. 5.24 Dependence of incoherent scattering cross-section ratio on x in aluminum

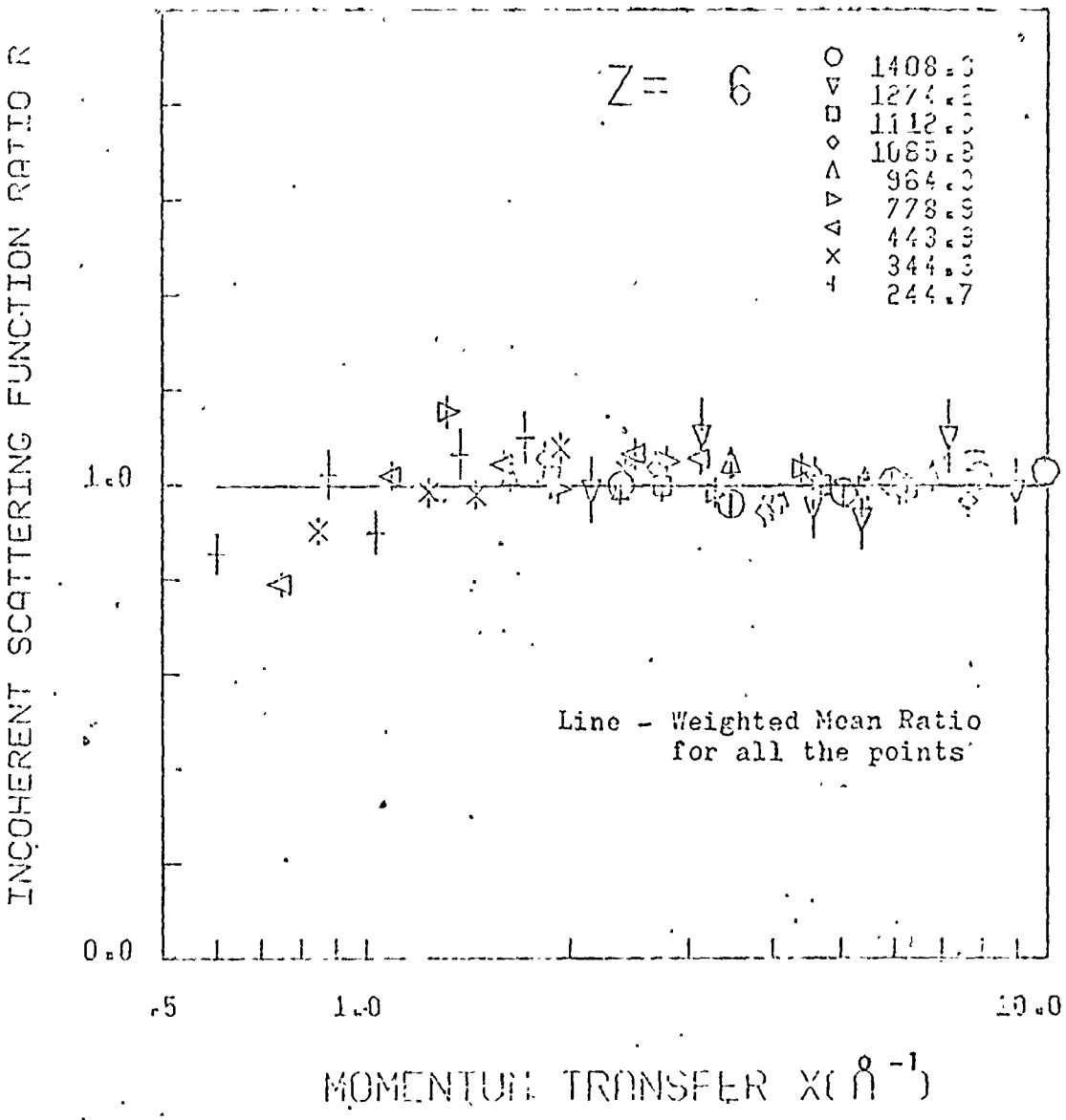

Fig. 5.25 Dependence of incoherent scattering cross-section ratio on x in copper

(scattering-in) then the condition that the sum of the partial scattering angles in both the scatterings must be equal to the mean scattering angle for the pure single scattering event. The extra-energy-spreads will then be observable too. If the second one is to scatter out of the observation solid angle the observed intensity will reduce. These intensity variations are a function of the thickness of the scatterer and the realistic estimates are difficult to compute for practical cases. This could be experimentally checked by varying the thicknesses of the scatterer. Such checks were made to ensure the linearity of the intensity after the correction for attenuation in the scatterer (cf. Fig. 3.5). There was no evidence for the thicknesses used in this experiment that the multiple scattering could be a factor.

The atomic electrons, bound to the nucleus as they are, have a distribution of momenta [DU 33, C071] and the initial momentum of the electron introduces a spread into the shape of the Compton scattered photon energy spectrum. This effect will be more important for higher atomic numbers than low Z-elements. From the latest momentum distribution tables [BI 75] it was found that the loss of intensity

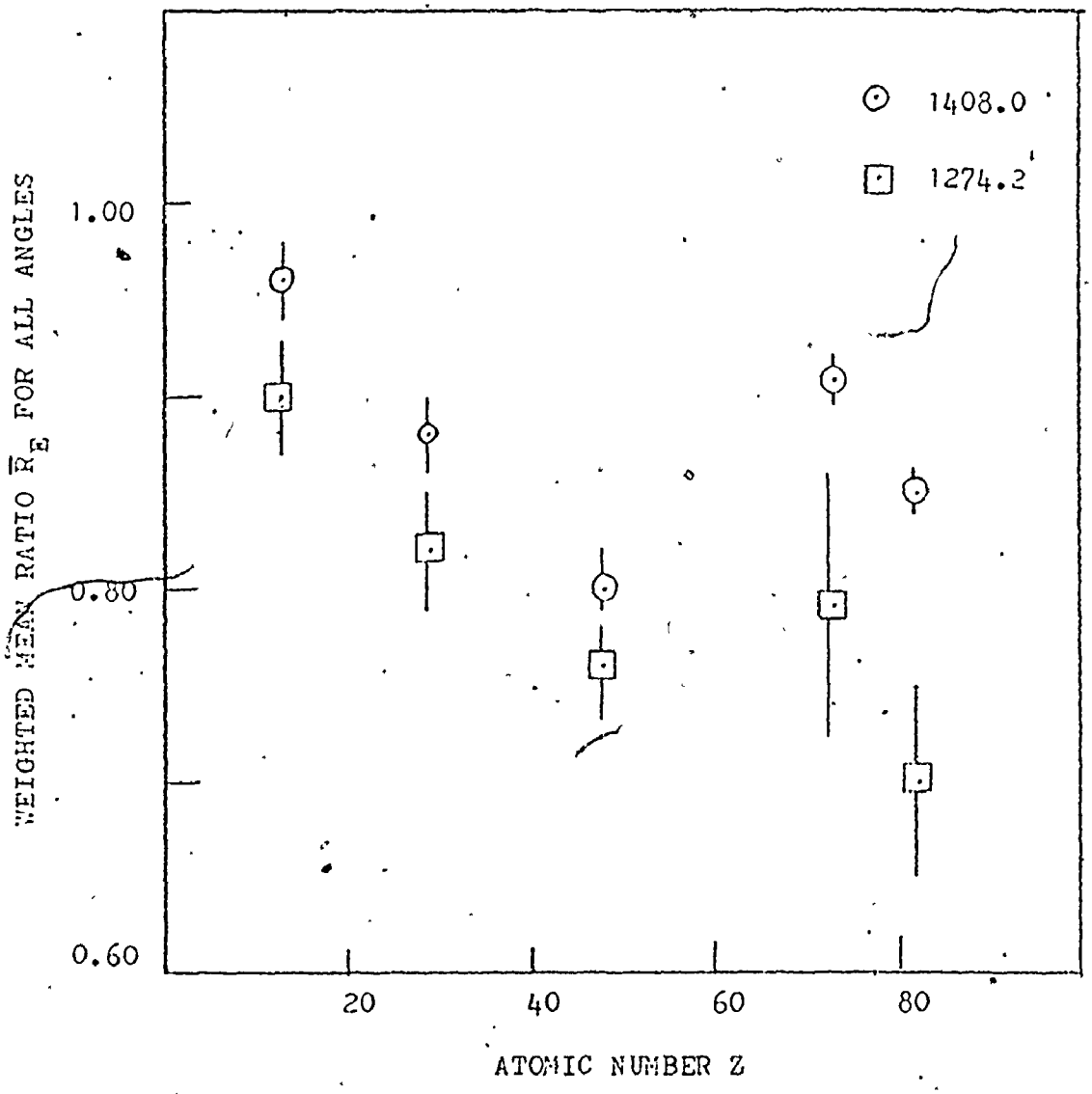

Fig. 5.26 Variation of $\bar{R}_E$ with atomic number Z for the incoherent scattering of 1408.0 and 1274.2 keV gamma rays

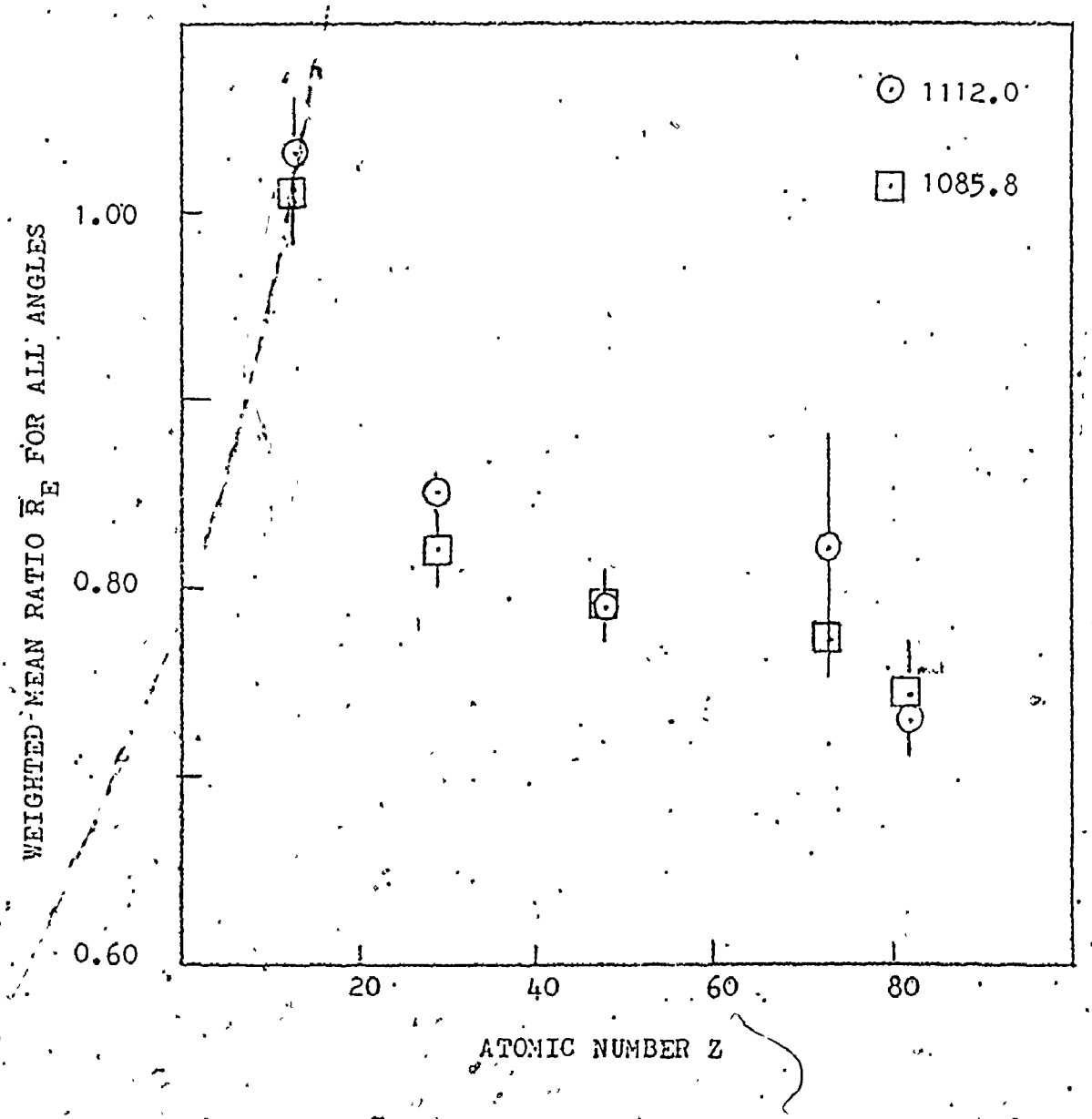

Fig. 5.27 Variation of $\bar{R}_E$ with Z for the incoherent scattering of 1112.0 and 1085.8 keV gamma rays

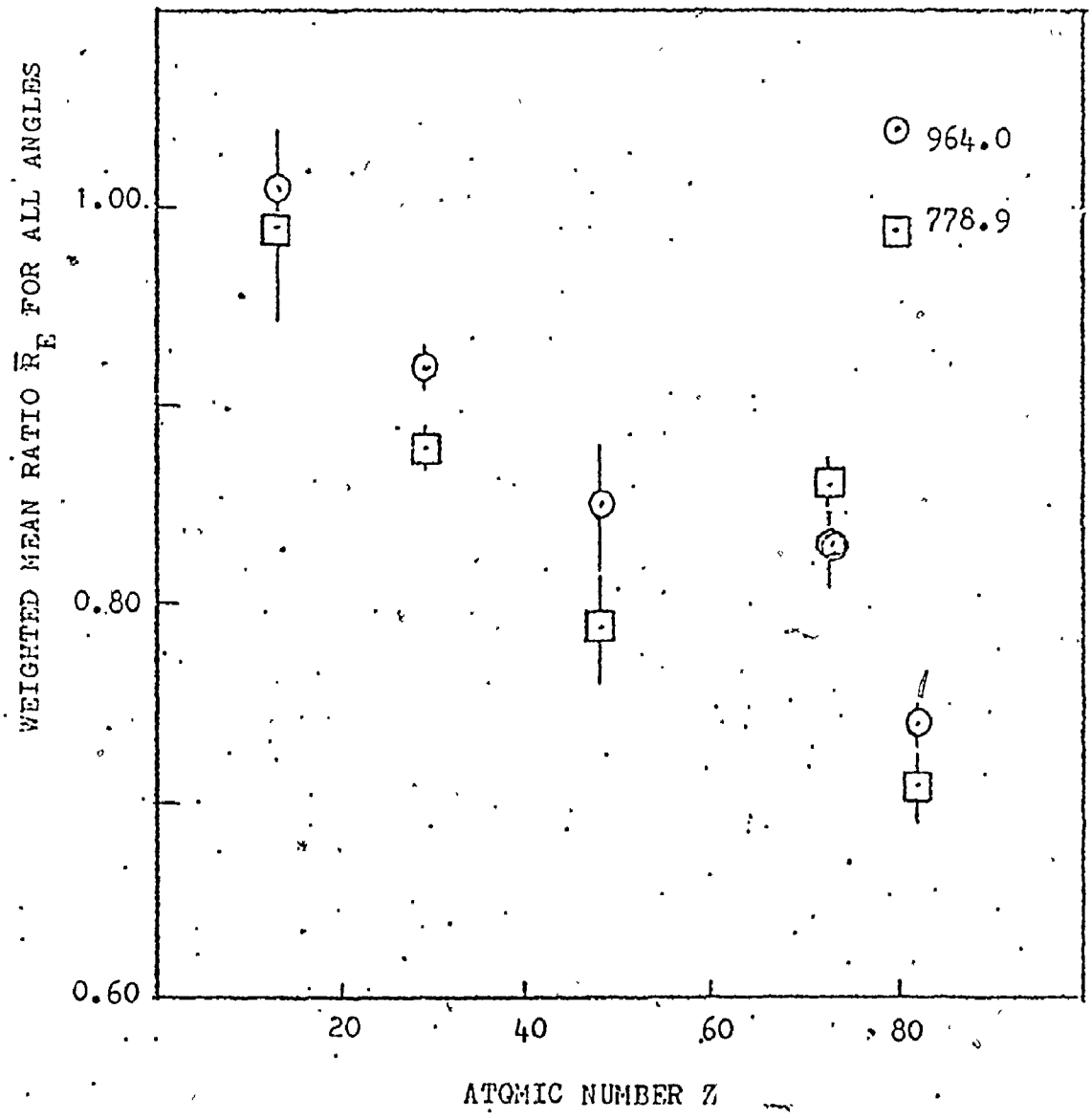

Fig. 5.28 Variation of $\bar{R}_E$ with Z for the incoherent scattering of 964.0 and 778.9 keV photons

in the background due to this effect would be less than 4% and this effect would not explain the discrepancy. The statistics in this experiment was not good enough to extract very small shape-effects due to the momentum distribution of the bound electrons.

From the theoretical section on incoherent scattering, it may be recalled that the formula for the incoherent scattering function involved the form-factor approximation. An analysis of the coherent scattering showed that for these energies between 778.9 and 1408.0 keV, the correction advocated by Brown et al. [BR 57] for binding of the electrons in the intermediate states would sufficiently reduce the form-factor scattering amplitude. A similar correction applied to the incoherent scattering function might lead to an experimentally agreeable result. Perhaps, this effect might explain the atomic number dependence of the deviation too since this correction involves the Coulomb potential for the atomic electron.

CHAPTER 6

Summary

1. Coherent scattering

The experimental coherent scattering differential cross-sections were compared with form-factor based calculations for lead, tantalum, cadmium and copper. In general it was found that these theoretical values are higher than the measured cross-sections by about 14%. There seems to be an explicit dependence of cross-sections on the photon energy and thus suggests a need for a correction to include this effect. The data for lead and tantalum have marked deviations from the theory in the region of x where L-shell amplitudes are expected to be prominent. While cadmium has a low cross-section in the region of K-shell dominance, copper data display disagreement in a region of x where L- , K- and M-shell scattering amplitudes are important. Theoretical calculations of scattering amplitudes with the inclusion of electron binding effects in the intermediate states might offer a part of the explanation. From the copper data one is lead to conclude that even M-shell amplitude computations can be very important besides K- and L- amplitudes for $x \geq 1.0$ Å^{-1}.

2. Incoherent scattering

The quantitative deviations between theoretical and experimental incoherent scattering functions are substantial for high-Z elements. The discrepancies are ~ 25% and this fact is strengthened by a large number of data points. Any systematic errors of that proportion if existent are not conceivable. The present investigation, being perhaps the first systematic measurement of incoherent scattering functions for small momentum transfers with a high resolution spectrometer system, will have to be checked by independent measurements to definitely establish the behaviour of the incoherent scattering process.

BIBLIOGRAPHY

AN 64 Anand, S., Singh, M. and Sood, B.S., Curr. Sci. 33, 139 (1964).

BA 30 Baker, E.B., Phys. Rev. 36, 630 (1930).

BA 69 "Lectures on Quantum Mechanics", Baym, G. W.A. Benjamin, Inc., New York (1969).

BE 31 Bewilogua, L., Z. Physik 19, 740 (1931).

BE 60 Bel'skii, S.A. and Starodubtsev, S.V., Sov. Phys. JETP 37 (10), 4, 700 (1960).

BI 75 Biggs, F., Mendelsohn, L.B. and Maun, J.B., Atomic Data and Nuclear Data Tables, 16, No. 3 (1975).

BO 74 Bowman, W.W. and MacMurdo, K.W., Atomic Data and Nuclear Data Tables, 13, 251 (1974).

BR 54 Brown, G.E., Peierls, R.E. and Woodward, J.B., Proc. Roy. Soc. A, 227, 51 (Part I)
Brenner, S., Brown, G.E. and Woodward, J.B., Proc. Roy. Soc. A, 227, 59 (Part II).

BR 55 Brown, G.E. and Mayers, D.F., Proc. Roy. Soc. A, 234, 387 (Part III).

BR 57 Brown, G.E. and Mayers, D.F., Proc. Roy. Soc. A, 242, 89 (1957).

CO 23 Compton, A.H., Phys. Rev., 21, 207A, 483 (1923).

CO 22 Compton A.H., Bull. Nat. Res. Council, No. 20, 19 (1922).

CO 23 Compton, A.H., Phys. Rev., 21, 207 and 483 (1923).

CO 35 Compton, A.H. and Allison, S.K., "X-Rays in Theory and Experiment", Van Nostrand, New Jersey (1935).

CO 71 Cooper, M., Adv. Phys., 20, 453 (1971).

CR 68 Cromer, D.T. and Mann, J.B., Acta Crys., A24, Part 2, 321 (1968).

CR 69 Cromer, D.T., J. Chem. Phys., 50, 4857 (1969).

DA 52 Davisson, C.M. and Evans, R.D., Rev. Mod. Phys., 24, 79 (1952).

DA 65 Davisson, C.M., "Alpha-Beta-Gamma-ray Spectroscopy", Ed. Siegbahn, K., ch. 2, 1, 37.

DE 23 Debye, P., Phys. Zeits, 24, 161 (1923).

DE 30 Debye, P. and Harm, F., Physik. Zeits., 31, 420 (1930).

DE 33 Delbrück, M., Z. Physik, 84, 144 (1933).

DI 68 Dixon, W.R. and Storey, R.S., Can. J. Phys., 46, 1153 (1968).

DU 33 DuMond, J.W.M., Rev. Mod. Phys., 5. 1 (1933).

DY 73 Dyson, N.A., "X-Rays in Atomic and Nuclear Physics", Longman Group Ltd., London (1973).

EI 05 Einstein, A., Ann. Physik, 17, 132 (1905).

EV 55 Evans, R.D., "The Atomic Nucleus", McGraw Hill, New York (1955).

FA 53 Fano, U., Nucleonics, 11, 8, p8 (1953).

FE 28 Fermi, E., Z. Physik, 48, 73 (1928).

FR 35 Franz, W., Z. Physik, 95, 652 (1935).

FR 36 Franz, W., Z. Physik, 98, 314 (1936).

GR 57 Grodstein, G.W., Nat. Bur. Standards Cir. 583 (1957).

HA 28 Hartree, D.R., Proc. Cambridge Phil. Soc., 24, 89, 111 (1928).

HA 51 Halpern, O. and Hall, H., Phys. Rev., 84, 5, p. 997 (1951).

HA 66 Hauser, U. and Mussgnug, B., Zeits. Physik, 195, 252 (1966).

HA 71 Hardie, G., De Vries, J.S. and Chiang, C.K., Phys. Rev. C. 3, 1287 (1971).

HE 31 Heisenberg, W., Z. Physik, 19, 737 (1931).

HE 54 Heitler, W., "The Quantum Theory of Radiation", 3 ed. Oxford Univ. Press (1954).

HU 75 Hubbell, J.H., Veigele, Wm. J., Briggs, E.A., Brown, R.T., Cromer, D.T., Howerton, R.J., J. Phys. Chem. Ref. Data 4, 3, p.471 (1975).

JO 68 Johnson, W.R. and Feiock, F.D., Phys. Rev., 168, 22 (1968).

KA 61 Kane, P.P. and Holzwarth, G.M., Phys. Rev., 122, 5, p.1579 (1961).

KA 67 Kane, P.P. and Basavaraju, G., Rev. Mod. Phys., 39, 52 (1967).

KL 29 Klein, O. and Nishina, Y., Z. Physik, 52, 853 (1929).

LE 52 Levinger, J.S., Phys. Rev., 87, 4, p.656 (1952).

MA 56 Mann, A.K., Phys. Rev., 101, 1, p.4 (1956).

ME 66 Messiah, A., "Quantum Mechanics", II, John Wiley & Sons (1966).

MO 50 Moon, P.B., Proc. Phys. Soc. (London), A63, 1189 (1950).

MO 58 Mössbauer, R.L., Zeits. Physik, 151, 124 (1958).

NA 64 Nath, A. and Ghose, A.M., Nucl. Phys, 57, 547 (1964).

NE 53 Nelms, A.T., Natl. Bur. Std. (U.S.) cir. #542 (1953).

NE 55 Nelms, A.T. and Oppenheim, J., J. Res. Natl. Bur. Std. (U.S.), 55, 53 (1955).

PA 27 Pauling, L., Proc. Roy. Soc. London, A114, 181 (1927).

PA 32 Pauling, L. and Sherman, J., Zeits. f. Krist, 81, 1 (1932).

PA 75 Papatzacos, P. and Mark, K., Physics Reports, 21, 81 (1975).

PDF74 Berry, L.G. (Ed.) "Powder Diffraction File", Pub. Joint Committee on Powder Diffraction Standards, U.S.A., SMH-24 (1974).

PI 46 Pirenne, M.H., "The Diffraction of X-rays and Electrons by Free Molecules", Cambridge Univ. Press, London (1946).

QU 66 Quivy, R., Nucl. Phys. 76, 362 (1966).

RO 52 Rohrlich, F. and Gluckstern, R.L., Phys. Rev., 86, 1, p.1 (1952).

RO 68 Roy, R. and Reed, R.D., "Interactions of Photons and Leptons with matter", Academic Press (1968).

SC 55 Schiff, L.I., "Quantum Mechanics", McGraw-Hill Company (1955).

SC 69 Schumacher, M., Phys. Rev., 182, 1, p.7 (1969).

SC 73a Smend, F., Schumacher, M. and Borchert, I., Nucl. Phys., A213, 309 (1973).

SC 73b Schumacher, M., Smend, F. and Borchert, I., Nucl. Phys., A206, 531 (1973).

SH 54 Brenner, S., Brown, G.E. and Woodward, J.B., Proc. Roy. Soc. A, 227, 59 (Part II).

SI 65 Singh, M. and Sood, B.S., Nucl. Phys., 64, 502 (1965).

ST 58 Storruste, A. and Tjøm, P.O., Nucl. Phys., 6, 151 (1958).

ST 70 Storm, E. and Israel, H.I., Nuclear Data Tables A7, 565 (1970).

TA 76 Tanner, A.C. and Epstein, I.R., Phys. Rev., A13, 335 (1976),
Phys. Rev., A14, 313 (1976),
Phys. Rev., A14, 328 (1976).

TH 26 Thomas, L.H., Proc. Camb. Phil. Soc., 23, 542 (1926).

VE 66 Veigele, Wm. J., Tracy, P.T. and Henry, E.M., Am. J. Phys., 34, 1116 (1966).

WE 27 Wentzel, G., Zeits. für Physik, 43, 481 (1927).

WA 29 Waller, I. and Hartree, D.R., Proc. Roy. Soc. London, A124, 119 (1929).